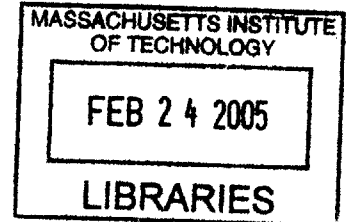


The Areal Reduction Factor (ARF) a Multifractal Analysis

by

Andreas Langousis

Diploma of Civil and Environmental Engineering (2003)
National Technical University of Athens.



BARKER

Submitted to the Department of Civil and Environmental Engineering
in partial fulfillment of the requirements
for the degree of

MASTER OF SCIENCE IN CIVIL AND ENVIRONMENTAL ENGINEERING

at the

MASSACHUSETTS INSTITUTE OF TECHNOLOGY


February 2005

© 2005 Massachusetts Institute of Technology. All rights reserved

Signature of Author.....

Department of Civil and Environmental Engineering

October 6, 2004

Certified by.....

Daniele Veneziano

Professor of Civil and Environmental Engineering

Thesis Supervisor

Accepted by.....

Andrew Whittle

Chairman, Departmental Committee on Graduate Students

The Areal Reduction Factor (ARF) a Multifractal Analysis

by

Andreas Langousis

Submitted to the Department of Civil and Environmental Engineering
on October 6, 2004 in partial fulfillment of the requirements
for the Degree of Master of Science in Civil and Environmental Engineering.

Abstract

The Areal Reduction Factor (ARF) η is a key parameter in the design for hydrologic extremes. For a basin of area A , $\eta(A, D, T)$ is the ratio between the area-average rainfall intensity over a duration D with return period T and the point rainfall intensity for the same D and T . Besides depending on A , D and possibly T , the ARF is affected by the shape of the basin and by a number of seasonal, climatic and topographic characteristics. Another factor on which ARF depends is the advection velocity, v_{ad} , of the rainfall features. Commonly used formulas and charts for the ARF have been derived by smoothing or curve-fitting empirical ARFs extracted from raingauge network records.

Here we derive some properties of the ARF under the assumption that space-time rainfall is exactly or approximately multifractal. We do so for various shapes of the rainfall collecting region and for $v_{ad} = 0$ and $v_{ad} \neq 0$.

When $v_{ad} = 0$, a key parameter in the analysis is the ratio $u_{res} = v_{res}/v_e$ between the “response velocity” $v_{res} = L/D$, where L is the maximum linear dimension of the region, and the “evolution velocity” $v_e = L_e/D_e$, where L_e and D_e are the characteristic linear dimension and characteristic duration of organized rainfall features.

The effect of $v_{ad} \neq 0$ depends on the shape of the region. For highly elongated basins, both the direction and magnitude of advection are influential, whereas for regular shaped regions only the magnitude v_{ad} matters.

We review ways in which rainfall has been observed to deviate from exact multifractality and models that capture such deviations. We show how the ARF behaves when rainfall is a bounded cascade in space and time. We also investigate the effect of estimating areal rainfall from raingauge network measurements. We find that bounded-cascade deviations from multifractality and sparse spatial sampling distort in similar ways the scaling properties of the ARF.

Finally we show how one can reproduce various features of empirical ARF charts by using multifractal and bounded cascade models and considering the effects of sparse spatial sampling.

Thesis Supervisor: Daniele Veneziano

Title: Professor of Civil and Environmental Engineering

*Dedicated to
my father,
my mother, and
my brother.*

Acknowledgments

Reaching the end effort, I would like to acknowledge all those who contributed and provided the basis for this work.

First of all I would like to thank my professor and friend Daniele Veneziano for his contributions to my thesis, and the time he spent working with me providing continuous support during this academic year. Daniele Veneziano is not only an outstanding professor and researcher; he is also a most understanding and helpful person. If it wasn't for him, I doubt this thesis would have been finished.

By no means can I forget my former research supervisor, professor and best friend Demetris Koutsoyiannis, who introduced me to the magic world of stochastic processes. I entered this field by taking his course "*Stochastic Hydrology*" at the National Technical University of Athens. By the end of the course I was addicted to stochastic processes and started working with him on stochastic modeling.

Of course, I cannot omit to acknowledge some persons that truly marked my life by providing me the basis in mathematics and engineering. My high-school teachers Stavros Drosakis and Demetris Nasiopoulos taught me that mathematics is not only an interesting game but also an attractive way of thinking.

Nikolaos Ioakimidis, Professor of Applied Mathematics at the Polytechnic School of University of Patras, is the person that academically fended for me most during my first year of graduate studies in the University of Patras. I still remember his words: "*Studying is good only if you know when to stop*", which I never followed.

George Christodoulou, Professor of Applied Hydraulics at the National Technical University of Athens, Andreas Andreadakis, Director of the Sanitary Engineering Laboratory at the National Technical University of Athens, and the Hydraulic Engineers Jack Gabrielidis and Tilemahos Papatthasiadis are the persons that I have to thanks most for becoming a Hydraulic Engineer.

Finally I owe a great thanks to my father, my mother and my brother who always supported me and never stopped believing in me.

Special Acknowledgments: This work was supported in part by the Department of Civil and Environmental Engineering of Massachusetts Institute of Technology under *Schoettler Fellowship*, in part by the National Science Foundation under Grant No. EAR-0228835, and in part by "*Alexander S. Onassis*" Public Benefit Foundation under Scholarship No. F-ZA 054/2004-2005.

Cambridge, October 2004

Andreas Langousis

Table of contents

Abstract.....	2
Acknowledgments.....	4
Introduction.....	6
1 Literature review.....	9
1.1 The Areal Reduction Factor (ARF).....	9
1.2 Empirical methodologies for estimating ARFs.....	10
1.3 Semi-theoretical methodologies for estimating ARFs.....	14
2 Extremes of multifractal rainfall in time.....	21
2.1 Cramer’s Theorem for sums of independent random variables.....	21
2.2 Extremes of bare and dressed multifractal cascades.....	23
2.3 Scaling properties of the intensity duration frequency curves.....	26
2.4 Conclusions and comments.....	31
3 Extremes of multifractal rainfall in time and space.....	32
3.1 Extremes of Multifractal Space-Time Rainfall for $v_{ad} = 0$	33
3.2 The Effect of Advection.....	47
3.3 Numerical validation.....	55
3.4 Velocity parameters.....	62
3.5 Comments.....	67
4. Imperfect scaling of rainfall, sparse sampling and their effects on the ARF.....	68
4.1 Observed deviations of rainfall from multifractality.....	70
4.2 Raingauge network density and deviations from multifractality.....	83
4.3 Effect of bounded cascade modeling and sparse sampling on the ARF.....	84
5. Application to the N.E.R.C. curves.....	91
5.1 N.E.R.C.’s ARF curves.....	91
5.2 Behavior of the ARF in Figure 5.2.....	95
5.3 Numerical reproduction of the N.E.R.C. ARF results.....	97
5.4 Conclusions and comments.....	102
6. Conclusions.....	104
References.....	110
Appendix A.....	116
Linkage between Haar wavelets and micro-canonical cascades.....	116

Introduction

In hydrological risk analysis and design, knowledge of the probability of rainfall extremes is essential. For example, in reservoir design and flood estimation one is interested in rainfall intensities averaged over an area A and a duration D , with a given return period T . These intensities are provided by the so-called Intensity Duration Area Frequency (IDAF) curves.

Direct estimation of the IDAF curves from rainfall records is a difficult task, because it is rare to have extensive records from spatially dense pluviometric networks or radar. For $A = 0$ (precipitation at a point), the IDAF curves reduce to the familiar Intensity Duration Frequency (IDF) curves.

Since it is relatively easy to estimate the IDF curves using long rainfall records from single pluviometric stations, a convenient and commonly used way of estimating the IDAF curves is to multiply the IDF values by an Areal Reduction Factor (ARF). This factor is defined as the ratio of the rainfall intensity averaged over area A and duration D with return period T , and the rainfall intensity at a point for the same D and T .

The ARF increases with decreasing area A , approaching unity as A tends to zero. Also, the ARF increases as duration D increases. The effect of the return period T on the ARF is not clear. N.E.R.C. (1975) finds a weak dependence of the ARF on T (ARF slightly increases as T decreases), whereas other researchers (Bell, 1976; Asquith *et al.*, 2000; De Michele *et al.*, 2001) find that the ARF is largely influenced by T . Specifically, they find that the ARF decreases with increasing T , and that its dependence (see above) on A and D becomes more pronounced for larger values of T .

A number of empirical formulas have been proposed for the estimation of the ARF from rainfall records. Most of them consider the ARF to be independent of the return period T . ARF curves for general use have also been proposed. These curves give the ARF as a function of only A and D , and therefore assume negligible dependence on the return period T , geometry of the basin, and climatic conditions.

Several studies have tried to derive the ARF, IDF or IDAF curves using semi-theoretical probabilistic models of rainfall (Roche, 1966; Rodriguez-Iturbe and Mejia, 1974; Bacchi and Ranzi, 1996; Sivapalan and Blöschl, 1998; Asquith and Famiglietti, 2000). Most of them incorporate the spatial correlation structure of rainfall, as well as semi-theoretical functions and

constants that have to be inferred from data. In practice, estimation of those quantities is often inaccurate.

Since rainfall data rarely allow direct estimation of rainfall intensities over the range of areas, durations and return periods of practical interest, one way to make the inference of rainfall extremes more robust is to use theoretical model-based results. Multifractal models provide a good representation of space-time rainfall fields (Lovejoy and Schertzer, 1995; Gupta and Waymire, 1993; Deidda, 2000) and possess scale-invariance properties that may be at the root of certain power-law behaviors observed in empirical ARF curves. Therefore, it is attractive to use the theory of multifractality to explain the behaviour of rainfall extremes and extend the empirical ARFs beyond the range of A , D and T covered by the data. For example, Bendjoudi *et al.* (1999) and Veneziano and Furcolo (2002a) used multifractal rainfall models to determine the scaling properties of the IDF curves.

In the simple case of perfect isotropic multifractality, rainfall intensity is the product of independent and identically distributed (id) random fluctuations. For rainfall, a multiplicative scheme is generally supported by data (Veneziano *et al.*, 1996; Carsteanu and Fofoula-Georgiou, 1996; Menabde *et al.*, 1997), whereas deviations from the id property have been found, typically in the form of dependences of the amplitude of the multiplicative fluctuations on scale (Perica and Fofoula-Georgiou, 1996b; Veneziano *et al.*, 1996; Menabde *et al.*, 1997; Menabde and Sivapalan, 2000; Veneziano *et al.*, 2003).

This thesis studies the behavior of Areal Reduction Factors (ARFs) under multifractality, the effects of deviations from exact multifractality, and the bias from the estimation of ARF from sparse spatial data. The latter is an important problem because ARF estimation is typically based on rainfall records from raingauge networks with finite density.

The thesis is organized as follows. Chapter 1 reviews the bibliography on IDF and IDAF curves, and on ARFs. Specifically, the definition of the ARF is given, and its relationship with the IDF and IDAF curves is discussed. Empirical and semi-theoretical methodologies for ARF estimation are analyzed, and empirical ARF curves proposed for general use are presented.

Chapter 2 reviews properties of multifractal processes and their implications on the IDF curves. We start by reviewing a result in large deviation theory known as Cramer's Theorem. Next we consider properties of extremes of multifractal cascades through linkage to Cramer's Theorem, and show how these properties are linked to the scaling of the IDF curves. In doing

so, we review and compare the approaches to IDF scaling of Bendjoudi *et al.* (1999) and Veneziano and Furcolo (2002a).

Chapter 3 extends the analysis from rainfall at a point to average rainfall intensity inside regions of various shapes. Specifically, we consider regular (square or circular) regions and highly elongated regions. The rainfall field is assumed to be multifractal and to advect with constant velocity $\mathbf{v}_{ad} = [v_{ad,x}, v_{ad,y}]$. First we study the case when $\mathbf{v}_{ad} = \mathbf{0}$. A key parameter in this case is the ratio $u_{res} = v_{res}/v_e$ between the “response velocity” $v_{res} = L/D$, where L is the maximum linear dimension of the region, and the “evolution velocity” $v_e = L_e/D_e$, where L_e and D_e are the characteristic linear dimension and characteristic duration of organized rainfall features. Then we examine the case when $\mathbf{v}_{ad} \neq \mathbf{0}$. An important parameter for advection is the ratio $u_{ad} = v_{ad}/v_e$ between the magnitudes of the advection velocity and the evolution velocity. For each case we study the scaling properties of the Intensity Duration Area Frequency (IDAF) curves and the Areal Reduction Factor (ARF). The results obtained are validated through simulation using multifractal cascade models. Finally we discuss the range of velocities v_{res} , v_e and v_{ad} in typical hydrologic applications.

In Chapter 4 we review observed deviations of rainfall from multifractality, in the form of dependences of the amplitude of the multiplicative fluctuations on scale. Proposed models that capture such deviations are discussed and the effects on the ARFs are studied through numerical simulation. We also study the effect of sparse spatial sampling on the estimated ARFs for different densities of the raingauge network.

Chapter 5 discusses features of the empirical Areal Reduction Factors (ARFs) proposed by the Natural Environmental Research Council (N.E.R.C.) (1975) and shows how these features can be matched by considering bounded cascade models of rainfall and sparse spatial sampling.

Conclusions and possible future research directions are given in Chapter 6.

1 Literature review

1.1 The Areal Reduction Factor (ARF)

The Intensity Duration Frequency (IDF) curves are a commonly used tool in hydrological estimation and design. These curves give the point rainfall intensity $i_{D,T}$ as a function of the averaging duration D and return period T .

At a pluviometric station, $i_{D,T}$ is typically estimated from rainfall data by: (1) sub-dividing the historical rainfall records into intervals of duration D , (2) finding the maximum rainfall intensity averaged over D for each year in the record, and (3) ranking the yearly maxima and finding $i_{D,T}$ such that,

$$P[I \geq i_{D,T}] = \frac{1}{T} \quad (1.1)$$

The empirical results may be smoothed by fitting a parametric distribution to the annual maximum values or by fitting a smooth function $f(D, T)$ to the empirical values of $i_{D,T}$. For example, a commonly used formula is (e.g. Stedinger *et al.*, 1993),

$$i_{D,T} = f(D, T) = \frac{k T^a}{(D + b)^m} \quad (1.2)$$

where k , a , b and m are fitting parameters.

In most hydrological applications (e.g. reservoir design, flood estimation), knowledge of the point rainfall intensity $i_{D,T}$ is not sufficient. Rather, one must estimate the intensity $i_{A,D,T}$ averaged over area A and duration D with return period T . Clearly,

$$\lim_{A \rightarrow 0} (i_{A,D,T}) = i_{D,T} \quad (1.3)$$

Plots of $i_{A,D,T}$ produce so-called Intensity Duration Area Frequency (IDAF) curves. The IDAF curves can be estimated using an approach similar to that used for the IDF curves, with the added complication of estimating areal average intensities from point rainfall data.

In practice, it is rare to have dense networks of pluviometric stations and a more convenient way to estimate the IDAF curves is to multiply the IDF values at a point by an Areal Reduction Factor (ARF). The ARF is defined as,

$$ARF(A, D, T) = \frac{i_{A,D,T}}{i_{D,T}} \quad (1.4)$$

Although not explicitly indicated in equation (1.4), the ARF depends also on climatic conditions, as well as the size and shape of the basin (Omolayo, 1993; Asquith and Famiglietti, 2000).

The ARF increases with decreasing area A , approaching 1 as A tends to zero. Also, the ARF increases with increasing duration D , approaching 1 as D tends to infinity. In Section 3.1, these empirical observations will be proved theoretically for a multifractal rainfall field in two spatial dimensions plus time.

Many studies have considered the effect of the return period T on the ARF with somewhat different conclusions. According to N.E.R.C. (1975), the ARF increases slightly as T decreases. Other studies (e.g. Bell, 1976; Asquith *et al.*, 2000; De Michele *et al.*, 2001) have found that the ARF is significantly influenced by the return period. Specifically, the latter studies find that the ARF decreases with increasing T and that dependence on A and D becomes more pronounced as T increases.

Next we review empirical and semi-theoretical methods to estimate ARFs.

1.2 Empirical methodologies for estimating ARFs

Let i_D^j ($j = 1, \dots, \nu$) denote concurrent average rainfall intensities over D at ν stations inside the region of interest. The mean area rainfall in D , $i_{A,D}$, is typically estimated as a weighted average of these average point intensities,

$$i_{A,D} = \sum_{j=1}^{\nu} w_j i_D^j \quad (1.5)$$

Frequently used weighting schemes are:

$$w_j = \frac{1}{\nu} \text{ (i.e. equal weighting)} \quad (1.6)$$

and

$$w_j = \frac{A_j}{\sum_{j=1}^{\nu} A_j} \quad (1.7)$$

where the A_j are the Thiessen polygon areas associated with the raingauge stations inside A (Thiessen, 1911). In both schemes, the weights w_j add to unity.

A number of empirical methodologies have been proposed to estimate the ARFs from rainfall records. Most of them assume that the ARF is independent of the return period (except for Bell's method, which is described later). Next we review these methodologies, as well as empirically derived ARF formulas.

1.2.1 US Weather Bureau method

After estimating the Thiessen weighting factor w_i for each pluviometric station i in the basin of interest, each year j of the rainfall record is divided into intervals of a given duration D . The areal rainfall for each interval of each year j is calculated and the interval when the areal rainfall is maximum is found. Finally, the ARF (assumed independent of the return period T) for duration D is estimated as

$$ARF_{US} = \nu \sum_{j=1}^n \sum_{i=1}^v w_i \dot{P}_{i,j} / \sum_{j=1}^n \sum_{i=1}^v P_{i,j} \quad (1.8)$$

where $P_{i,j}$ is the annual maximum point rainfall in D at station i in year j , $\dot{P}_{i,j}$ is the point rainfall in D at station i on the day when the annual maximum areal rainfall occurs in year j , ν is the number of stations in the basin and n is the length of the data record in years.

The method uses different weighting schemes: Thiessen weighting for $\dot{P}_{i,j}$ in the numerator and equal weighting for $P_{i,j}$ in the denominator.

Based on the assumptions that the ARFs are independent of the return period T , and on the geometry of the basin, Leclerc and Schaake (1972) used equation (1.8) to derive the following empirical relation for $ARF(A, D)$:

$$ARF(A, D) = 1 - \exp(-1.1 D^{-0.25}) + \exp(-1.1 D^{-0.25} - 2.59 \times 10^{-2} A) \quad (1.9)$$

where A is in [Km^2] and D is in [hours]. Weather Bureau (TP-29) specifies ARF for areas up to 1 100 km^2 and storm durations of 1, 3, 6 and 24 hours; see also Figure 1.1.

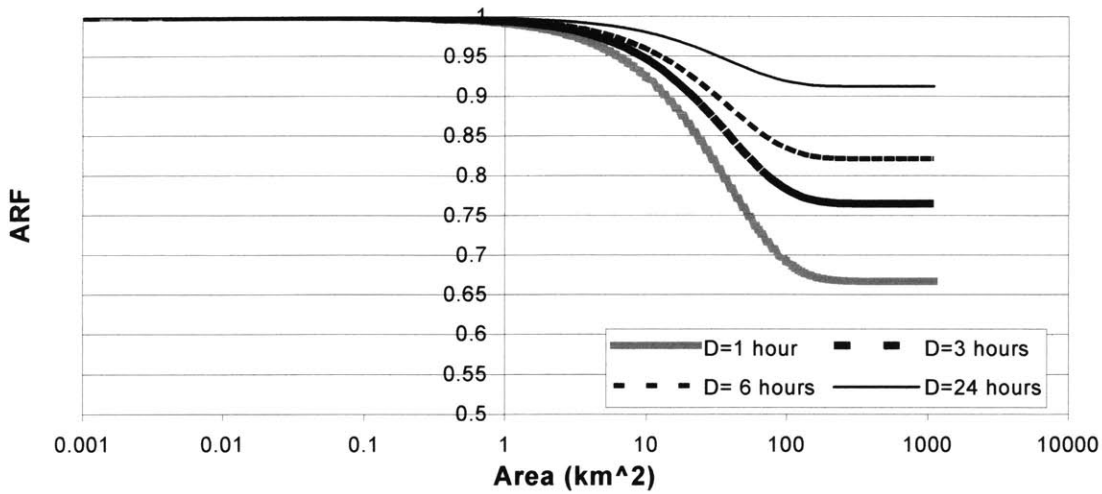


Figure 1.1: Leclerc and Schaake ARF curves for durations of 1, 3, 6, and 24 hours and areas up to 10000 Km².

One can observe In Figure 1.1 that for A small (say $A < 5 \text{ Km}^2$) ARF is nearly constant and equal to 1. This behavior of the ARF is in agreement with the fact that for $A = 0$ the IDAF curves reduce to the IDF curves and thus $\text{ARF} = 1$. For intermediate values of A (say $10 \text{ Km}^2 < A < 100 \text{ Km}^2$) the ARF is approximately a power function of A/D , whereas for A large (say $A > 100 \text{ Km}^2$) the ARF depends only on D . This behavior of the ARF for large A is not supported by other studies (see for example N.E.R.C.'s diagram, Section 1.2.2), and it is probably associated with data limitations for large areas.

1.2.2 N.E.R.C. method

Assuming independence of T and using equal weighting, N.E.R.C. (1975) calculates the ARF as

$$\text{ARF}_{\text{NERC}} = \frac{1}{nv} \sum_{j=1}^n \sum_{i=1}^v (\dot{P}_{i,j} / P_{i,j}) \quad (1.10)$$

N.E.R.C. (1975) used equation (1.10) to estimate the ARFs for thirteen basins in the United Kingdom with areas ranging from 10 to 18000 Km². Averaging durations ranged from 2 minutes to 25 days. N.E.R.C. then smoothed and interpolated the empirical results to obtain the diagram in Figure 1.2 (for a more detailed review of the data and the fitting procedure see Section 5.1).

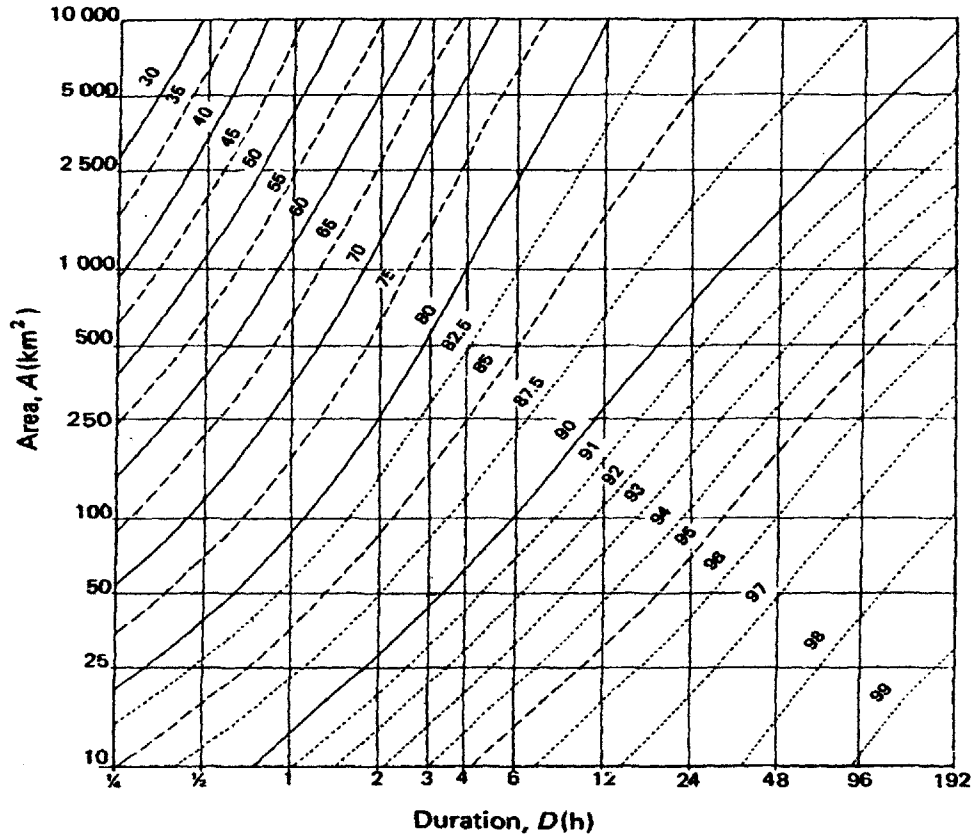


Figure 1.2: ARFs for durations D from 15 minutes to 8 days and areas A from 10 to 10 000 Km^2 . Reproduced from N.E.R.C. (1975) *Flood Studies Report*, Vol. II, p. 40.

According to N.E.R.C. (1975), these ARFs correspond to rainfall events with return period $T = 2\text{-}3$ years.

A general fit to the UK N.E.R.C. (1975) data shows that the ARF is approximately constant for $D \propto A^{0.7}$. However, the N.E.R.C. iso-ARF curves indicate a variable slope, with $D \propto A^{0.5}$ for large A and small D , and larger A exponents for lower areas or larger D (for a more detailed analysis see Section 5.2).

Based on these N.E.R.C. curves, Koutsoyiannis (1997) derived an analytical expression for the ARF,

$$ARF = 1 - \frac{0.048 A^{0.36 - 0.01 \ln(A)}}{D^{0.35}} \geq 0.25 \quad (1.11)$$

where A is in Km^2 and D is in hours. This expression is shown graphically in Figure 1.3.

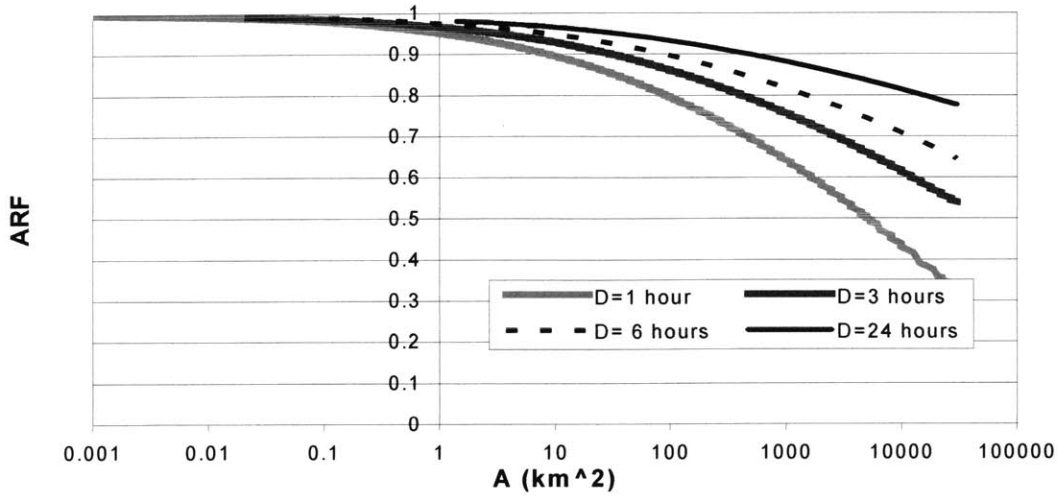


Figure 1.3: Koutsoyiannis ARF curves for durations of 1, 3, 6, and 24 hours and areas up to 30 000 Km².

1.2.3 Bell's method

This method takes into account the variation of the ARF with return period T . Suppose that the rainfall records cover a period of a year. The annual maximum areal and point rainfall series are both ranked in descending order. The ARF with given rank r and thus return period T (e.g. $T = \frac{n-1}{r}$) is estimated as the ratio of the areal rainfall of rank r to the sum of the weighted (e.g. Thiessen weights w_i , $i = 1, 2, \dots, v$) point rainfalls of the same rank,

$$ARF^{T(r)}_{Bell} = \frac{\sum_{i=1}^v w_i P'_{i,r}}{\sum_{i=1}^v w_i P_{i,r}} \quad (1.12)$$

If the ARF is independent of the return period, then

$$ARF_{Bell} = \frac{1}{n} \sum_{r=1}^n ARF^{T(r)}_{Bell} \quad (1.13)$$

If moreover one uses equal weighting (i.e. $w_i = 1/v$), then equation (1.13) reduces to the N.E.R.C. method (equation (1.10)).

1.3 Semi-theoretical methodologies for estimating ARFs

Several studies have tried to derive the ARF (or IDF or IDAF) curves using probabilistic models of space-time rainfall. An early attempt in this direction was made by Roche (1966) who

developed a theoretical approach to point and areal rainfall based on the correlation structure of intense storms.

Rodriguez-Iturbe and Mejia (1974) extended Roche's (1966) approach by assuming that the rainfall field is a zero mean stationary Gaussian process. Averaging over the catchment area A results in a variance reduction factor κ^2 given by

$$\kappa^2 = E[\rho(\|\mathbf{x}_2 - \mathbf{x}_1\|)] \quad (1.14)$$

where $E[\rho]$ is the expected spatial correlation coefficient between two points \mathbf{x}_1 and \mathbf{x}_2 independently and uniformly distributed inside the catchment area, and $\|\mathbf{x}\|$ denotes the length of vector \mathbf{x} . Equation (1.14) can be simplified to,

$$\kappa^2 = \int_0^{\infty} \rho(r) g_R(r) dr \quad (1.15)$$

where R is the random distance between \mathbf{x}_1 and \mathbf{x}_2 , and $g_R(r)$ is the Probability Density Function (PDF) of R . Notice that κ^2 is a function of the spatial correlation structure of rainfall and the size and shape of the catchment. Rodriguez-Iturbe and Mejia (1974) argued that κ , the square root of these variance reduction factor, could be interpreted as the ARF (i.e. $ARF = \kappa$).

In the method of Rodriguez-Iturbe and Mejia (1974), the mean of the averaged rainfall intensity does not change with the catchment area. However, this is a property of the stationary parent process not the extreme value process that is of interest for ARF determination. Therefore, the theoretical validity of the ARFs calculated by this method is limited.

Another important limitation is that, the method does not account for the effect of duration D on the ARFs. It is assumed that this information is included in the spatial autocorrelation function $\rho(r)$. Thus, the effect of the duration D on the ARF is not clear.

A different approach, based on crossing properties of random fields, was proposed by Bacchi and Ranzi (1996). This approach assumes stationarity of the rainfall field and homogeneity of the crossings in space and derives a complicated expression for the ARF that incorporates a large number of fitting parameters that have to be inferred from data.

Bacchi and Ranzi (1996) argue that the ARF increases with decreasing A and increasing D . Furthermore, they find a small decrease of the ARF with increasing T .

Properties of extremes of random functions were used also by Sivapalan and Blöschl (1998). The starting point of their approach is to derive the parent distribution of the catchment average

rainfall intensity from that of point rainfall intensity assuming stationarity of the rainfall field in space and time. Sivapalan and Blöschl (1998) start from the assumption that the parent distribution of the point rainfall intensity i_p is of the *Exponential* type,

$$f(i_p) = \frac{1}{\beta_p} \exp\left(-\frac{i_p}{\beta_p}\right) \quad (1.16)$$

with mean $\mu_p = \beta_p$ and variance $(\sigma_p)^2 = (\beta_p)^2$. They further assume that the spatial autocorrelation function of the rainfall field is isotropic exponential,

$$\rho_p(r) = \exp\left(-\frac{r}{\lambda}\right) \quad (1.17)$$

where r is separating distance and λ is the spatial correlation length, defined as

$$\lambda = \int_0^{\infty} \rho_p(r) dr \quad (1.18)$$

The areal rainfall parent process i_A is assumed in approximation to have a *Gamma* distribution,

$$f(i_A) = \frac{\left(\frac{i_A}{\beta_A}\right)^{k_A} \exp\left(-\frac{i_A}{\beta_A}\right)}{\beta_A \Gamma(k_A)} \quad (1.19)$$

with mean $\mu_A = k_A \beta_A$ and variance $(\sigma_A)^2 = k_A (\beta_A)^2$. The parameters of the distributions in equations (1.16) and (1.18) are related as

$$k_A \beta_A = \beta_p \quad (1.20)$$

$$k_A (\beta_A)^2 = \kappa^2 (\beta_p)^2 \quad (1.21)$$

where κ^2 is a variance reduction factor defined in the same way as in Rodriguez-Iturbe and Mejia (1974); see equation (1.14). The parameters β_p and κ^2 are inferred from data. The areal rainfall extreme value process, which is of the *Gumbel* type, is then semi-analytically derived using two empirical functions f_1 and f_2 . The ARF, which is defined as the ratio between the areal and point rainfall intensities with the same duration and return period, is given by

$$ARF\left(\kappa^2 \frac{A}{\lambda^2}, D, T\right) = \frac{\kappa^2 b(D) c(D) f_2(\kappa^2) - \frac{\kappa^2}{f_1(\kappa^2)} \ln\left\{\ln\left(\frac{T}{T-1}\right)\right\}}{b(D) c(D) - \ln\left\{\ln\left(\frac{T}{T-1}\right)\right\}} \quad (1.22)$$

where $b(D)$ and $c(D)$ are semi-analytical functions. For $T \rightarrow \infty$ equation (1.22) reduces to

$$ARF(\kappa^2 \frac{A}{\lambda^2}) = \frac{\kappa^2}{f_1(\kappa^2)} \quad (1.23)$$

which indicates that the ARF depends solely on the catchment area A and the spatial correlation structure of the rainfall field, which is expressed through κ^2 . The method does not directly account for the duration D of the rainfall event, and it is argued that this piece of information is included in the spatial correlation structure of the field. The calculated ARFs, increase with decreasing A and increasing D , and are highly dependent on both the return period T and the spatial correlation function $\rho_p(r)$ of the point rainfall process.

Also the work of Asquith and Famiglietti (2000) can be considered to belong to this class of stochastic methods. Their methodology is based on two assumptions: (1) the largest potential volume of a storm occurs when the storm is centered over the centroid of the basin, and (2) the cross-correlation of concurrent precipitation at two non-centroid locations is insignificant. Although the former assumption seems plausible, the latter is not. This is so because the spatial correlation structure of rainfall is an important parameter that affects the ARF; see above.

The derivation of the ARF is performed through a function $S_T(r)$ defined as the expected value of the ratio between the rainfall depth at some location a distance r from the centroid of the design storm and the depth of the annual maximum with return period T at the same location. $S_T(r)$ depends on return period T and describes the spatial structure of a storm radiating away from the centroid of the basin.

Asquith and Famiglietti (2000) estimate the ARF as the ratio between the T year rainfall depth over a catchment area A and the point rainfall depth Z_T with return period T at the centroid of the storm, i.e.

$$ARF(A, T) = \frac{1}{Z_T} \frac{\int_A S_T(r) dx dy}{A} = \frac{\int_A S_T(r) dx dy}{A} \quad (1.24)$$

The method does not directly account for the duration D of the rainfall event, and thus the influence of D on the estimated ARFs is not clear. The approach produces ARFs that are significantly influenced by the return period T . Specifically, for longer return periods T the estimated ARFs decay faster with increasing A .

An altogether different approach was followed by Coles and Tawn (1996). These authors observe that stochastic approaches to the ARF are of basically two types: those that emphasize

the spatial dependence of point rainfall without special focus on extremes (the above mentioned approaches are of this type) and those that focus on extremes and pay less attention to spatial dependence. Coles and Tawn (1996) propose a method of the latter type.

A third class of methods exploits the scaling properties of space-time rainfall. Scaling ideas for temporal rainfall have been used by Hubert *et al.* (1993), Benjoudi *et al.* (1999) and Veneziano and Furcolo (2002a) to derive scaling properties of the IDF curves. The latter two approaches will be reviewed in detail in Section 2.3.

Also De Michele *et al.* (2001) pursued a scaling approach to explain the ARF and the IDAF curves. Defining $I(D, A)$ as the maximum annual value of the mean rainfall intensity for duration D and area A , De Michele *et al.* (2001) argue that $I(D, A)$ could have either self similar or multifractal scaling properties with D and A . Then they focus exclusively on the self similar property stating that $I(D, A)$ must have the form,

$$I(D, A-a_0) = D^a g\left(\frac{(A-a_0)^b}{D^c}\right) \quad (1.25)$$

where a_0 is the collection area of a raingauge, g is some random function and a , b and c are scaling exponents. By reasoning on the limiting behavior of $I(D, A)$ as $A \rightarrow 0$ and A or $D \rightarrow \infty$, De Michele *et al.* (2001) conclude that g must have the form,

$$g\left(\frac{(A-a_0)^b}{D^c}\right) = a_1 \left(1 + \omega \frac{(A-a_0)^b}{D^c}\right)^{-\beta} \quad (1.26)$$

where a_1 is the random intensity in a_0 for $T = 1$, and ω and β are constants. The argument by which equation (1.26) is derived is not clear. The constants a , b , c , ω and β are determined from data (relations among these constants allow one to reduce them to 4 independent parameters).

The approach of De Michele *et al.* (2001) makes direct assumptions on the scaling of annual maximum rainfall, without deriving such properties from the scaling of the rainfall field itself. This “*shortcut*” makes it difficult to choose on conceptual grounds between self similarity and multifractality of the annual extremes and also makes it impossible to link the scaling exponents of the ARF and IDAF curves to properties of the rainfall field (e.g. stratiform vs. convective, summer vs. winter precipitation), determine the effect of return period T on the ARF, and characterize the distribution of the random variable a_1 in equation (1.26). All these properties

and parameters have to be inferred from data. Moreover, the way in which the area of the rain gauge collector is treated in equations (1.25) and (1.26) destroys scaling.

From application to a region near Milan (8 years of data, 16 stations covering an area of about 300 km²), De Michele *et al.* find dynamic scaling with D proportional to A , whereas a general fit to the N.E.R.C. (1975) data gives $D \propto A^{0.7}$; see Section 1.2.2.

In a recent study, Castro *et al.* (2004) developed a multifractal approach to explain how the IDAF curves scale with A , D and T . Castro *et al.* (2004) assumed anisotropy of rainfall in space and time with D proportional to $A^{z/2}$, where z is a scaling coefficient estimated from data. Using a large-deviations property of multifractal fields, Castro *et al.* (2004) find that

$$i_{A,D,T} \propto D^{-1} A^{-z/2} T^{\delta} \quad (1.27)$$

where δ is a positive constant independent of T , which is estimated from data. Castro *et al.* (2004) do not discuss the exact derivation of equation (1.27). They also argue that δ is given by

$$\delta = \frac{1-\gamma}{1-c(\gamma)} \quad (1.28)$$

where $c(\gamma)$ is the co-dimension function of rainfall when approached as a 1D multifractal process in time. Although not explicitly stated, the analysis of Castro *et al.* (2004) is valid only for large values of T . This is so because the ratio $\frac{1-\gamma}{1-c(\gamma)}$ becomes a constant independent of γ , and thus T , only for $\gamma \geq \gamma^*$, i.e.

$$\frac{1-\gamma}{1-c(\gamma)} = \frac{1}{q^*}, \quad \gamma \geq \gamma^* \quad (1.29)$$

where γ^* is the highest singularity order for which the moment scaling function of the temporal rainfall process is finite, and q^* is the associated moment order greater than 1; see Section 2.2.2. From an application to a rainfall event in Mexico, Castro *et al.* (2004) find $\delta = 1.227$ and $z = 1.161$. Since $z \approx 1$ one can conclude that rainfall is in approximation isotropically multifractal in space and time. However, one should be cautioned that $\delta = 1.227$ corresponds to $\frac{1-\gamma}{1-c(\gamma)} = \frac{1}{0.82}$. Thus $\gamma < \gamma^*$ and hence δ is not a constant independent of T as argued by Castro *et al.* (2004).

In this thesis, we study the behavior of Areal Reduction Factors (ARFs) under multifractality, determine the effects of deviations from exact multifractality, and quantify the bias from the estimation of ARF from sparse spatial data. We also study the effect of rainfall advection on the ARF. The effect of advection depends on the shape, size and response time of the basin. Finally we discuss observed features of empirical Areal Reduction Factors (ARFs) and show how these features can be explained using scaling properties of rainfall, deviations from perfect scaling, and biases from sparse spatial sampling.

2 Extremes of multifractal rainfall in time

In hydrological risk analysis and design, knowledge of the probability of rainfall extremes is essential. However, available data rarely allow one to directly estimate rainfall intensities over the range of areas, durations and return periods of practical interest. One way to make the inference of rainfall extremes more robust is to use model predictions. Multifractal models provide a good representation of space-time rainfall fields (Lovejoy and Schertzer, 1995; Gupta and Waymire, 1993; Deidda, 2000). Therefore, one can use the theory of multifractality as a framework to elucidate the behaviour of empirical rainfall extremes and extend the results beyond the empirical range of A , D and T . For example, Bendjoudi *et al.* (1999) and Veneziano and Furcolo (2002a) used multifractal rainfall models to determine certain scaling properties of the Intensity Duration Frequency (IDF) curves.

We start in Section 2.1 by reviewing a result in large deviation theory known as Cramer's Theorem. This theorem forms the basis of the analysis that follows.

In Section 2.2, we review certain extreme properties of discrete multifractal cascades, which are the simplest models displaying multifractal behaviour (Gupta and Waymire, 1993). First we describe how a multiplicative cascade is generated and define the concepts of bare and dressed measure densities. Then we derive properties of extremes of bare and dressed densities through linkage to and an extension of Cramer's Theorem.

Section 2.3 uses the previous results on cascades to derive properties of the IDF curves. In particular, we review the approaches by Bendjoudi *et al.* (1999) and Veneziano and Furcolo (2002a). Bendjoudi *et al.* (1999) focus on the limiting case when D is finite and $T \rightarrow \infty$, while Veneziano and Furcolo (2002a) derive the scaling properties of the IDF curves for: (1) $D \rightarrow 0$ and T finite and (2) D finite and $T \rightarrow \infty$. For the second case with D finite and $T \rightarrow \infty$ the results of Veneziano and Furcolo (2002a) are the same as those of Bendjoudi *et al.* (1999).

Conclusions and comments on the foresaid approaches are summarized in Section 2.4.

2.1 Cramer's Theorem for sums of independent random variables

Cramer's Theorem is a fundamental result in large deviation theory. The theorem deals with a property of extremes of sums or averages of independent and identically distributed variables. The reason why normal theory does not apply is that the extremes of interest move farther and

farther into the tail of the distribution as the number of added or averaged variables increases. These extremes are in a region of the distribution that has not yet converged to a normal shape. We review in detail the derivation of the theorem, because this result is essential to all the developments that follow in this chapter. For additional information on Cramer's Theorem and related results the reader is referred to Den Hollander (2000), Dembo and Zeitouni (1993) and Stroock (1994).

Let $S_n = \frac{1}{n}(X_1 + \dots + X_n)$ be the average of n independent copies of a random variable X with Cumulative Distribution Function (CDF) F . Assume that X is unbounded and that the moment generating function,

$$M(q) = E[e^{qX}] = \int_{-\infty}^{\infty} e^{qX} dF(x) \quad (2.1)$$

is finite for all $q \geq 0$. Using the fact that the X_i are independent and identically distributed, one obtains

$$E[e^{nqS_n}] = \prod_{i=1}^n E[e^{qX_i}] = M(q)^n \quad (2.2)$$

Next we use a result in probability theory called Markov's inequality (Papoulis, 1990, p. 131). This inequality states that, for any non negative random variable U and any positive constant δ ,

$$P[U \geq \delta E[U]] \leq \frac{1}{\delta} \quad (2.3)$$

Application to $U = e^{nqS_n}$ and use of equation (2.2) gives

$$P[e^{nqS_n} \geq \delta M(q)^n] \leq \frac{1}{\delta}, \quad \delta > 0 \text{ and } q \geq 0 \quad (2.4)$$

or, solving for S_n

$$P\left[S_n \geq \frac{1}{nq} \ln(\delta) + \frac{1}{q} \ln\{M(q)\}\right] \leq \frac{1}{\delta}, \quad \delta > 0 \text{ and } q \geq 0 \quad (2.5)$$

If we define $\gamma = \frac{1}{nq} \ln(\delta) + \frac{1}{q} \ln\{M(q)\}$, then $\delta = M(q)^n e^{nq\gamma}$ and equation (2.5) becomes

$$P[S_n \geq \gamma] \leq M(q)^n e^{-nq\gamma} = e^{-n(q\gamma - K(q))} \text{ for any real } \gamma \text{ and } q \geq 0 \quad (2.6)$$

where $K(q) = \ln(M(q))$. By minimizing the right hand side of equation (2.6) with respect to q we obtain

$$P[S_n \geq \gamma] \leq \exp(-n \max_{q \geq 0} \{q\gamma - K(q)\}) \quad (2.7)$$

We now introduce the Legendre transform of $K(q)$ as the function $c(t)$ given by

$$c(t) = \max_q \{qt - K(q)\}, \quad -\infty < t < \infty \quad (2.8)$$

Using $c(t)$ and taking logs, equation (2.7) becomes,

$$\frac{\ln(P[S_n \geq \gamma])}{n} \leq -c(\gamma) \quad (2.9)$$

For $\gamma > E[X]$ one can show (for details, see Stroock 1994, p. 30) that, in the limit as $n \rightarrow \infty$, the inequality in equation (2.9) becomes an equality, giving

$$\lim_{n \rightarrow \infty} \frac{\ln(P[S_n \geq \gamma])}{n} = -c(\gamma) \quad (2.10)$$

This result is known as Cramer's Theorem (Cramer, 1938).

The condition $M(q) < \infty$ for all $q \geq 0$ is not necessary for equation (2.10) to hold. For example, equation (2.10) is known to hold also for $M(q)$ finite in an infinitesimal right and left neighborhood of zero (Dembo and Zeitouni, 1993, section 2.2.1). Under the latter condition and for X continuous, equations (2.9) and (2.10) can be refined (Cramer, 1938, p. 5-23) as

$$\begin{cases} P[S_n \geq \gamma] = g(\gamma, n) e^{-nc(\gamma)} \\ g(\gamma, n) = \left(2\pi n \frac{[c'(\gamma)]^2}{c''(\gamma)}\right)^{-1/2} (1+o(1)) \end{cases} \quad (2.11)$$

where the ' and '' signs denote the first and second derivative respectively, and $o(1)$ is a term that vanishes as n goes to infinity. Similar asymptotic results have been derived by Bahadur and Ranga Rao (1960) for X not continuous. Equation (2.11) is used next to derive properties of multifractal extremes.

2.2 Extremes of bare and dressed multifractal cascades

There is a direct analogy between certain multifractal extremes and the large deviation behavior of sums of independent identically distributed random variables.

Consider an isotropic multiplicative cascade. The cascade construction starts at level 0 as a uniform unit measure in the d -dimensional cube S_d . The multiplicity of the cascade is m , where m is an integer larger than one. This means that, after n cascade levels, S_d is divided into m^{nd} cubic tiles T_{ni} ($i = 1, \dots, m^{nd}$) with linear size m^{-n} . The measure density inside T_{ni} is obtained by multiplying the measure density of the parent tile at level $n-1$ by a random variable Y_{ni} with unit mean value. Although in general the random variables Y_{ni} may be dependent both within and among cascade levels, here we consider only the case when the Y_{ni} are independent copies of a random variable Y , called the generator of the cascade.

Let ε_{m^n} be the average measure density of the cascade inside a cube of linear size m^{-n} , or at resolution m^n . One may distinguish between two types of such average densities: the bare measure density $\varepsilon_{m^n,b}$ and the dressed measure density $\varepsilon_{m^n,d}$. The difference between bare and dressed densities is that the former does not include fluctuations at scales smaller than m^{-n} . Thus, $\varepsilon_{m^n,b}$ is the measure density within a tile T_{ni} when the multiplicative cascade construction is terminated at level n . By contrast, the dressed measure density is the average density in T_{ni} for the completely developed cascade. The two measure densities are given by

$$\begin{cases} \varepsilon_{m^n,b} = \prod_{i=1}^n Y_i \\ \varepsilon_{m^n,d} = \varepsilon_{m^n,b} Z \end{cases} \quad (2.12)$$

where Y_1, Y_2, \dots, Y_n are n independent copies of Y and Z is the so-called *dressing factor*, which is independent of $\varepsilon_{m^n,b}$ and has the same distribution as $\varepsilon_{1,d}$, the dressed measure in S_d .

Next we derive extreme value properties of the bare and dressed measure densities from Cramer's Theorem.

2.2.1 Extremes of bare densities

Let $X_i = \log_m(Y_i)$, so that

$$\log_m(\varepsilon_{m^n,b}) = \sum_{i=1}^n \log_m(Y_i) = \sum_{i=1}^n X_i = n S_n \quad (2.13)$$

where $S_n = \frac{1}{n}(X_1 + \dots + X_n)$. In multifractal analysis one often characterizes the distribution of Y through the function $K_b(q)$ defined as,

$$K_b(q) = \log_m E[Y^q] = \frac{K(q)}{\ln(m)} \quad (2.14)$$

and its associated Legendre transform

$$c_b(\gamma) = \max_{q \geq 0} \{qx - K_b(q)\} = \frac{c(\gamma)}{\ln(m)}, \quad -\infty < x < \infty \quad (2.15)$$

The function $K_b(q)$ is the *bare moments scaling function* of the cascade. In fact, for any q for which $E[Y^q]$ exists, equations (2.12) and (2.14) give

$$E[(\varepsilon_{m^n, b})^q] = E[Y^q]^n = m^{nK_b(q)} \quad (2.16)$$

Using equation (2.13) and the results on S_n in equations (2.10) and (2.11) one obtains the following extreme properties of bare multifractal measures:

$$\lim_{n \rightarrow \infty} \frac{1}{n} \log_m(P[\varepsilon_{m^n, b} \geq m^{n\gamma}]) = -c_b(\gamma), \quad \gamma > E[\log_m(Y)] \quad (2.17)$$

and

$$\begin{cases} P[\varepsilon_{m^n, b} \geq m^{n\gamma}] = g(\gamma, n) m^{-nc_b(\gamma)} \\ g(\gamma, n) = \left(2\pi n \ln(m) \frac{[c_b'(\gamma)]^2}{c_b''(\gamma)}\right)^{-1/2} (1+o(1)) \end{cases} \quad (2.18)$$

Since $n \ln(m) = \ln(m^n)$, the function $g(\gamma, n)$ varies slowly with the resolution of the cascade m^n . One often states equation (2.18) as

$$P[\varepsilon_{m^n, b} \geq m^{n\gamma}] \sim m^{-nc_b(\gamma)} \quad (2.19)$$

where \sim denotes equality up to a factor that varies slowly with the resolution m^n .

2.2.2 Extremes of dressed densities

The main novelty when dealing with dressed densities $\varepsilon_{m^n, d}$ is that the moments of $\varepsilon_{m^n, d}$ above some finite order q^* may diverge. This critical order q^* is given by the conditions $q^* > 1$ and $K_b(q^*) = d(q^* - 1)$ (Kahane and Peyriere, 1976; Schertzer and Lovejoy, 1987), where d is the Euclidean space dimension. Therefore, q^* is a function of d . When needed for clarity we shall indicate this dependence by using the notation $q^* = q^*(d)$. Similarly to bare densities, the moments of the dressed densities have a power law dependence on the resolution m^n . In fact,

$$E[(\varepsilon_{m^n, d})^q] = E[Z^q] E[(\varepsilon_{m^n, b})^q] = E[Z^q] m^{nK_b(q)} \propto m^{nK_d(q)} \quad (2.20)$$

where the dressed moment scaling function $K_d(q)$ is given by

$$K_d(q) = \begin{cases} K_b(q), & q < q^* \\ \infty, & q \geq q^* \end{cases} \quad (2.21)$$

Veneziano (2002) showed that the dressed densities $\varepsilon_{m^n, d}$ satisfy a large-deviation relationship similar to equation (2.18),

$$P[\varepsilon_{m^n, d} \geq m^{n\gamma}] = h(\gamma, n) m^{-nc_d(\gamma)} \quad (2.22)$$

where $c_d(\gamma)$ is the Legendre transform of $K_d(q)$,

$$c_d(\gamma) = \max_q \{q\gamma - K_d(q)\} = \begin{cases} c_b(\gamma), & \gamma \leq \gamma^* \\ q^* \gamma + d(q^* - 1), & \gamma > \gamma^* \end{cases} \quad (2.23)$$

d is the Euclidean space dimension, $\gamma^* = K_b'(q^*)$ and $h(\gamma, n)$ is a function that varies slowly with the resolution m^n ; see Veneziano (2002) for details on the form of the function h . In analogy with equation (2.19), one can write

$$P[\varepsilon_{m^n, d} \geq m^{n\gamma}] \sim m^{-nc_d(\gamma)} \quad (2.24)$$

For q^* finite, the moments of $\varepsilon_{m^n, d}$ above order q^* diverge and the distribution of $\varepsilon_{m^n, d}$ must have an algebraic upper tail of the type

$$\lim_{s \rightarrow \infty} P[\varepsilon_{m^n, d} \geq s] \sim s^{-q^*} \quad (2.25)$$

This tail behavior of the dressed densities is due to the algebraic tail of the dressing factor Z .

2.3 Scaling properties of the intensity duration frequency curves

This section reviews past work on the scaling properties of the IDF curves under the assumption that rainfall is a stationary multifractal process. Two approaches are presented, one by Bendjoudi *et al.* (1999) and the other by Veneziano and Furcolo (2002a), which in different ways utilize the extremal properties of multifractal cascades given in Section 2.2.

First, we introduce some notation. Let I_D be the average rainfall intensity in a time period of duration D . We assume that I_D is stationary multifractal with random generator A_r . This means that

$$I_D =_d A_r I_{rD} \quad (2.26)$$

This scaling property is hypothesized to hold below some maximum temporal aggregation D_{max} .

Also define $T(D, i)$ to be the return period of the event $I_D > i$. The return period $T(D, i)$ can be expressed in different ways. A standard definition is

$$T_1(D, i) = \frac{1}{P[I_{max,D} > i]} \quad (2.27)$$

where $I_{max,D}$ is the maximum of I_D over a unit time period (e.g. one year). Equation (2.27), with a unit time period of one year, is appropriate when, as in rainfall, the phenomenon of interest has seasonal variations. In the context of a stationary model an often more convenient definition is,

$$T_2(D, i) = \frac{D}{P[I_D > i]} \quad (2.28)$$

which is the reciprocal of the expected number of D intervals in a uniform partition of the unit time interval when $I_D > i$. This second definition of return period is the one used by Bendjoudi *et al.* (1999) and Veneziano and Furcolo (2002a) and is the one used in the rest of this chapter.

2.3.1 Bendjoudi *et al.* approach

Although not explicitly stated, the analysis of Bendjoudi *et al.* (1999) aims at deriving the scaling properties of the IDF curves for large T and small D .

Since rainfall at a point is a multifractal process in time, the Euclidean dimension of the observation space is $d = 1$. Bendjoudi *et al.* (1999) do not use this condition and rather consider d as a parameter to be determined. As in equation (2.23), they write the co-dimension function of the rainfall process for $\gamma \geq \gamma^*$ as

$$c_d(\gamma) = q^* \gamma - d(q^* - 1) \quad (2.29)$$

where q^* depends on d . Then, using equation (2.22) with $\varepsilon_{m^n, d} = I_D$ and $m^n = D_{max}/D$, Bendjoudi *et al.* (1999) write

$$P\left[I_D \geq \left(\frac{D_{max}}{D}\right)^\gamma\right] = \tilde{h}(\gamma, D_{max}/D) \left(\frac{D_{max}}{D}\right)^{-q^* \gamma + d(q^* - 1)}, \quad \gamma \geq \gamma^* \quad (2.30)$$

where $\tilde{h}(\gamma, D_{max}/D) = h(\gamma, \log_m(D_{max}/D))$. Introducing the condition $P\left[I_D \geq \left(\frac{D_{max}}{D}\right)^\gamma\right] = \frac{D}{T}$, which comes from the definition of the return period in equation (2.28), and replacing $(D_{max}/D)^\gamma$ with $i(D, T)$,

$$\frac{D}{T} = \tilde{h}(\gamma, D_{max}/D) i(D, T)^{-q^*} \left(\frac{D_{max}}{D}\right)^{d(q^*-1)}, \quad \gamma \geq \gamma^* \quad (2.31)$$

Next, Bendjoudi *et al.* (1999) argue that the function $\tilde{h}(\gamma, D_{max}/D)$ may be considered constant. Thus,

$$i(D, T) \propto D^{-(d(q^*-1)+1)/q^*} T^{1/q^*} \quad (2.32)$$

If one now sets $d = 1$ (the physical dimension of the observation space for point rainfall) one obtains

$$i(D, T) \propto D^{-1} T^{1/q^*(1)} \quad (2.33)$$

where $q^*(1)$ is q^* for $d = 1$. This implies that the yearly maxima $I_{max,D}$ scale with D in the self similar way

$$I_{max,D} =_d r I_{max,rD} \quad (2.34)$$

2.3.2 Veneziano and Furcolo approach

First, Veneziano and Furcolo (2002a) extend equation (2.22) to obtain an expression for $P[\varepsilon_{m^a,d} \geq a m^a]$, where a is a given positive constant.

Writing $a r^\gamma = r^{\gamma + \log_r a}$, one may use equation (2.22) to obtain

$$P[\varepsilon_{r,d} \geq a r^\gamma] = P[\varepsilon_{r,d} \geq r^{\gamma + \log_r a}] = \tilde{h}(\gamma + \log_r a, r) r^{-c_d(\gamma + \log_r a)} \quad (2.35)$$

where $\tilde{h}(\gamma, r) = h(\gamma, \log_m r)$. Using Taylor series expansion, one can approximate the function $c_d(\gamma + \log_r a)$ for large r as

$$c_d(\gamma + \log_r a) \approx c_d(\gamma) + c_d'(\gamma) \log_r a \quad (2.36)$$

Then equation (2.35) becomes

$$P[\varepsilon_{r,d} \geq a r^\gamma] \approx \tilde{h}(\gamma + \log_r a, r) a^{-c_d'(\gamma)} r^{-c_d(\gamma)} \quad (2.37)$$

Using equation (2.23) one can prove that $c_d'(\gamma)$ in equation (2.37) is given by

$$c_d'(\gamma) = \begin{cases} q(\gamma), & \gamma \leq \gamma^* \\ q^*, & \gamma > \gamma^* \end{cases} \quad (2.38)$$

Veneziano and Furcolo (2002a) use equations (2.35) and (2.37) to derive results on the IDF curves, as summarized below.

If rainfall intensity has mean value $\mu = E[I_D]$, then I_D has the unit-mean cascade representation,

$$I_D = \mu \varepsilon_{D_{max}/D, d} \quad (2.39)$$

where $\frac{D_{max}}{D}$ is the resolution. Thus, using equation (2.35),

$$P \left[I_D \geq \mu a \left(\frac{D_{max}}{D} \right)^\gamma \right] = \tilde{h} \left(\gamma + \log_{D_{max}/D} (a), \frac{D_{max}}{D} \right) \left(\frac{D_{max}}{D} \right)^{-c_d(\gamma + \log_{D_{max}/D} (a))} \quad (2.40)$$

Recalling from equation (2.28) that $i(T, D)$ satisfies $P[I_D \geq i] = \frac{D}{T}$, one wants to find a and γ such as the right hand side of equation (2.40) equals $\frac{D}{T}$, i.e.

$$\tilde{h} \left(\gamma + \log_{D_{max}/D} (a), \frac{D_{max}}{D} \right) \left(\frac{D_{max}}{D} \right)^{-c_d(\gamma + \log_{D_{max}/D} (a))} = \frac{D}{T} \quad (2.41)$$

Veneziano and Furcolo (2002a) examine two limiting cases of equation (2.41). The first case is when $\log_{D_{max}/D} (a)$ is infinitesimal. This condition attains for any finite T and $\frac{D_{max}}{D} \rightarrow \infty$. This means that $\log_{D_{max}/D} (a) \rightarrow 0$. Hence using equation (2.36), equation (2.41) becomes,

$$\tilde{h} \left(\gamma, \frac{D_{max}}{D} \right) a^{-c_d(\gamma)} \left(\frac{D_{max}}{D} \right)^{-c_d(\gamma)} = \frac{D}{T} \quad (2.42)$$

The property that $\tilde{h}(\gamma, r)$ is slow varying in r implies that, for any given D_1 and D_2 ,

$$\lim_{D_{max} \rightarrow \infty} \frac{\tilde{h}(\gamma, D_{max}/D_1)}{\tilde{h}(\gamma, D_{max}/D_2)} = 1 \quad (2.43)$$

i.e. for large D_{max}/D the function $\tilde{h} \left(\gamma, \frac{D_{max}}{D} \right)$ may be considered independent of D . Then equation (2.42) is satisfied by taking,

$$\gamma = \gamma_1 \quad \text{and} \quad a \propto \left(\frac{T}{D_{max}} \right)^{1/q_1} \quad (2.44)$$

where γ_1 is such that $c_d(\gamma_1) = 1$ and $q_1 = q(\gamma_1)$ is the associated moment order. Since $\gamma_1 < \gamma^*$, for the derivation of equation (2.44) we have used $c_d'(\gamma_1) = q(\gamma_1)$ in equation (2.38). Also, it is a direct consequence of equations (2.21) and (2.23), that the quantities γ_1 and q_1 do not depend on

the dimension of the observation space d . Equations (2.42) and (2.44) imply the following scaling relationship of $i(D, T)$ with D and T .

$$i(D, T) \propto D^{-\gamma_1} T^{1/q_1} \quad (2.45)$$

Equation (2.45) gives the scaling properties of the IDF values for T finite and $D \rightarrow 0$. An interpretation of equation (2.45) is that for D small the annual maxima $I_{max,D}$ satisfy the self similarity condition,

$$I_{max,D} = r^{\gamma_1} I_{max,rD} \quad (2.46)$$

However, notice that equation (2.45) was derived using the definition of return period in equation (2.28) not (2.27) and hence without reference to the definition of the annual maxima. Therefore the interpretation in equation (2.46) is not strictly correct.

The second case considered by Veneziano and Furcolo (2002a) is when $\gamma + \log_{D_{max}/D}(a) > \gamma^*$, which occurs for large T and relatively small D_{max}/D ratios. Given that $\gamma + \log_{D_{max}/D}(a) > \gamma^*$ and using equation (2.29) for $d=1$ (Euclidean dimension of the observation space), the co-dimension function has the form

$$c_d(\gamma + \log_{D_{max}/D} a) = (\gamma + \log_{D_{max}/D} a) q^*(1) - (q^*(1) - 1) \quad (2.47)$$

and equation (2.41) becomes,

$$\tilde{h}\left(\gamma + \log_{D_{max}/D}(a), \frac{D_{max}}{D}\right) a^{-q^*(1)} \left(\frac{D_{max}}{D}\right)^{-q^*(1)\gamma + q^*(1) - 1} = \frac{D}{T} \quad (2.48)$$

If $\tilde{h}\left(\gamma + \log_{D_{max}/D}(a), \frac{D_{max}}{D}\right)$ does not vary much with either D_{max}/D or a , then equation (2.48) is satisfied for

$$\gamma = 1 \quad \text{and} \quad a \propto \left(\frac{T}{D_{max}}\right)^{1/q^*(1)} \quad (2.49)$$

Therefore, for very large T the IDF values scale as

$$i(D, T) \propto D^{-1} T^{1/q^*(1)} \quad (2.50)$$

This is the same as the relation derived by Bendjoudi *et al.* (1999); see equation (2.33). From equation (2.50) one concludes that, in the extreme upper tail, the annual maxima $I_{max,D}$ satisfy the self-similarity condition

$$I_{max,D=d} = r I_{max,rD} \quad (2.51)$$

The scaling properties of the IDF curves for the above limiting cases have been validated numerically by Veneziano and Furcolo (2002a).

2.4 Conclusions and comments

The analysis of Bendjoudi *et al.* (1999) aims at deriving the parameters q^* and d from IDF curves estimated empirically from rainfall records. Although not explicitly stated, their analysis is valid for large T and small D . If the empirical IDF curves have the form,

$$i(D, T) \propto D^\zeta T^b \quad (2.52)$$

then Bendjoudi *et al.* (1999) find q^* and d by equating the scaling exponents in equations (2.32) and (2.52). For example, using an empirical formula of the type in equation (2.52) obtained by Farthouat (1962) for the Bordeaux area, Bendjoudi *et al.* (1999) find $q^* = 2.78$ and $d = 0.64$. However one should be cautioned that q^* is a function of d , and independent estimation of these two quantities from rainfall data is not mathematically correct. Moreover, values of d (dimension of the observation space) other than 1 seems to make little physical sense. The likely reason why values of d smaller than 1 are obtained, is that the empirical IDF curves were derived for return periods $T \leq 20$ years and in this range the theoretical analysis of Bendjoudi *et al.* (1999) does not apply.

The analysis of Veneziano and Furcolo (2002a) is more complete. It derives the scaling properties of the IDF curves for two limiting cases: (1) $D \rightarrow 0$ and T finite and (2) D finite and $T \rightarrow \infty$. For $D \rightarrow 0$ and T finite, the theoretical dependence of $i(D, T)$ on D is of the type D^{γ_1} with $0 < \gamma_1 < 1$. This corresponds better to the empirical results of Farthouat (1962) and indeed to the value of the exponent ζ of the empirical IDF functions, which is typically in the range $[-0.7, -0.6]$. For the second case with D finite and $T \rightarrow \infty$, the results of Veneziano and Furcolo (2002a) are the same as those of Bendjoudi *et al.* (1999) for Euclidean dimension of the observation space $d = 1$.

3 Extremes of multifractal rainfall in time and space

In Chapter 2 we analyzed the behavior of rainfall extremes when rainfall is observed at a point on the geographical plane. Here we extend the analysis to the average rainfall intensity inside regions of various shapes with maximum linear size L . Specifically, we consider regular (square or circular) regions and highly elongated regions in which the narrowest dimension is much smaller than L . On the geographical plane (x, y) the maximum elongation is assumed to be in the y direction; see Figure 3.1.

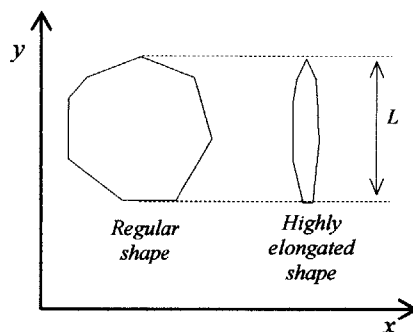


Figure 3.1: Schematic representation of regular and highly elongated regions.

In a Lagrangian reference the rainfall field in (x, y, t) space is assumed multifractal. The field advects with constant velocity $\mathbf{v}_{ad} = [v_{ad,x}, v_{ad,y}]^T$, where the superscript T denotes the transpose of a vector. We consider first the case when $\mathbf{v}_{ad} = \mathbf{0}$ and then examine the effect of $\mathbf{v}_{ad} \neq \mathbf{0}$. For each case we study the scaling properties of the Intensity Duration Area Frequency (IDAF) curves and the Areal Reduction Factor (ARF). These properties further depend on the shape of the region.

The chapter is organized as follows. Section 3.1 derives properties of the IDAF curves for the case $\mathbf{v}_{ad} = \mathbf{0}$. This is mainly an extension of the work of Veneziano and Furcolo (2002a) on the Intensity Duration Frequency (IDF) curves for the case of point rainfall. Using these results, we obtain the scaling properties of the IDAF curves and the ARFs with the size of the region L , the period of aggregation D and the return period T . We do so for three limiting geometries of the rainfall collecting region: a regular 2D region (a square or a disc), a line segment and a point. A key parameter in this analysis is the ratio $u_{res} = v_{res}/v_e$ between the “response velocity” $v_{res} = L/D$ and the “evolution velocity” $v_e = L_e/D_e$, where L_e and D_e are the characteristic linear

dimension and duration of rainfall generating features. Finally, we study how the IDAF curves and the ARFs behave for rectangular rainfall collecting regions (for regions with intermediate geometry between a line segment and a square).

In Section 3.2, we study the effect of advection ($\mathbf{v}_{ad} \neq \mathbf{0}$) on the IDF, IDAF curves and ARFs. In particular, we analyze the effect of advection for three spatial sampling cases: sampling at a geographical point (which might idealize the small collection area of a rain gauge), sampling along a line segment (which idealizes a highly elongated rainfall collection region), and sampling over a disc (which idealizes collection over a regular shaped region). We find that the scaling properties of the IDF and IDAF curves and the ARFs are affected by advection. For highly elongated basins, both the direction and magnitude of advection are influential, whereas for rainfall collection at a point or over a regular shaped region only the magnitude of advection, v_{ad} , matters. An important parameter for advection is the ratio $u_{ad} = v_{ad}/v_e$ between the magnitudes of the advection velocity and the evolution velocity.

Section 3.3 validates numerically the theoretical results previously obtained. This is done for two separate cases: (1) no advection of the rainfall field (Section 3.3.1) and (2) constant advection velocity (Section 3.3.2).

In Section 3.4 we discuss the range of velocities v_{res} , v_e and v_{ad} that are encountered in typical hydrologic applications. Focusing on problems of flood estimation, v_{res} is estimated by setting D equal to the concentration time of the basin, t_c . In this case, v_{res} ranges from about 3 to 7.5 Km/h. v_{res} depends mostly on the average slope of the basin and much less on its size. The rainfall evolution velocity, v_e , ranges from about 5 to 20 Km/h and v_{ad} usually takes values between 30 and 50 Km/h at small scales (a few kilometers) and from 20 to 40 Km/h at large scales (say 100 or more kilometers). However, local conditions have important effect on v_{ad} .

Comments are presented in Section 3.5.

3.1 Extremes of Multifractal Space-Time Rainfall for $\mathbf{v}_{ad} = \mathbf{0}$

In this section we extend the analysis of Veneziano and Furcolo (2002a) from point to spatially averaged rainfall, for the case without advection. We assume that space-time rainfall intensity is an infinitely dressed multifractal measure and derive the scaling properties of the Intensity Duration Area Frequency (IDAF) curves for different dimensions of the observation space, d . We do so for three limiting geometries of rainfall collecting regions: a square ($d = 3$), a line

segment ($d = 2$) and a point ($d = 1$). We then use these results to obtain properties of the Areal Reduction Factor (ARF).

When $d = 1$ (sampling at a point) only the temporal dimension of rainfall is considered and the IDAF curves reduce to the familiar Intensity Duration Frequency (IDF) curves. For $d = 2$ rainfall is observed along a line segment, which is the limiting case for rainfall collection over a very elongated region, whereas for $d = 3$ rainfall is observed inside a square region in space.

Finally we discuss the case of rectangular rainfall collecting regions.

3.1.1 Infinite dressing and limiting geometries of the observation region

In the analysis that follows, we make use of two quantities with the physical dimension of velocity [Length/Time]: The “evolution velocity” $v_e = L_e/D_e$, where L_e and D_e are the characteristic linear size and lifetime of rainfall structures, and the “response velocity” $v_{res} = L/D$, where L and D are the maximum linear size of the rainfall collecting region (for example a basin) and the duration of rainfall averaging (e.g. the response time of the basin). One may relate these two velocities using the dimensionless parameter $u_{res} = v_{res}/v_e$, which we call the “response velocity parameter”. Hence u_{res} indicates whether the response is faster ($u_{res} > 1$) or slower ($u_{res} < 1$) than the evolution of rainfall features such as convective cells, cell clusters and mesoscale precipitation regions. For example, in hydrologic application, u_{res} might be larger or smaller than 1 depending on whether the hydrologic response of the basin is dominated by fast runoff (as for example in highly saturated basins, flash-floods, and urban watersheds) or by slow infiltration, subsurface flow and exfiltration processes. For a more detailed analysis of v_e and v_{res} , see Section 3.4.

Suppose space-time rainfall is stationary and isotropically multifractal. Then $I(t|L, D)$, the average rainfall intensity in the time period $[t, t + D]$ inside a region of linear size L , satisfies

$$I(t|L, D) =_d B_r I(rt|rL, rD), \quad r \geq 1 \quad (3.1)$$

where B_r is an appropriate random variable. This scaling relation holds below some duration D_e for temporal aggregation and below some length L_e for spatial aggregation. If we assume that the evolution velocity v_e does not depend on the size of the rainfall generating features then $v_e = L_e/D_e$. For simplicity and without loss of generality, we set $D_e = 1$ and $L_e = 1$. Therefore, the region of multifractal behaviour is the unit square $\Omega = \{0 < L \leq 1, 0 < D \leq 1\}$ and $v_e = 1$.

Equation (3.1) can be represented graphically by noting that, on the $(\ln(L), \ln(D))$ plane, I has “ B_r multifractal scaling” along 45° lines; see Figure 3.2 for a schematic representation and Section 3.3.1 for numerical validation. Each 45° line in Figure 3.2 is characterized by one value of the response velocity parameter $u_{res} = L/D$. The 45° line with $D = L$ and $u_{res} = 1$, denoted by L_1 , passes through the origin and has special importance for the analysis that follows. Notice that points on L_1 correspond to cubic “cascade tiles” of different size in space-time and square regions on the (L, D) plane. Below L_1 , the (L, D) rectangles are elongated in the spatial direction and $u_{res} > 1$, whereas above L_1 the rectangles are elongated in the temporal direction and $u_{res} < 1$. We shall refer to these regions as the high- and low-velocity regions, respectively. The regions with $u_{res} \gg 1$ (e.g. $u_{res} > 5$) and $u_{res} \ll 1$ (e.g. $u_{res} < 1/5$) are called the very high and very low velocity regions.

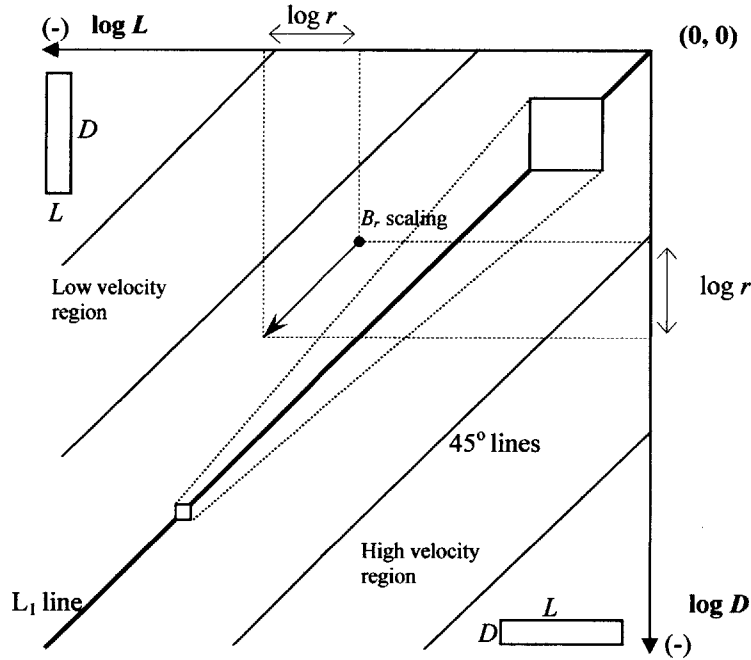


Figure 3.2: 45° scaling in $(\ln(L), \ln(D))$ plane.

Strictly speaking, equation (3.1) is the only scaling relation for I inside Ω . However, in good approximation, scaling relations of different types hold in the very high and very low velocity regions. For $u_{res} \gg 1$ (in practise, for u_{res} larger than about 5), the region (L, D) is highly elongated in the spatial direction. Therefore the process $I(t|L, D)$ is nearly identical to the process $I(t|L, rD)$ (for a justification of this, see Veneziano and Furcolo (2002b)). Also, the

processes $I(t|L, D)$ and $I(rt|rL, rD)$ are related through B_r - multifractal scaling according to equation (3.1). Therefore, for $u_{res} \gg 1$,

$$I(t|L, D) \approx_d B_{r_i} I(r_i t|r_i L, r_i D), r_i \geq 1 \quad (3.2)$$

The scaling factor r_d in equation (3.2) is arbitrary, provided that $\frac{r_i L}{r_d D} \gg 1$. For $u_{res} \ll 1$ (in practise, for u_{res} smaller than about 1/5), the region (L, D) is highly elongated in the temporal direction. Therefore,

$$I(t|L, D) \approx_d B_{r_d} I(r_d t|r_d L, r_d D), r_d \geq 1 \quad (3.3)$$

In this case r_i is arbitrary, provided that $\frac{r_i L}{r_d D} \ll 1$.

The scaling relations in equations (3.2) and (3.3) are presented symbolically in Figure 3.3. What is shown along each arrow is the scaling factor in the associated transformation (“1” means that the distribution is unchanged). For example, raingauge records have minimal area coverage, and thus scaling in time is essentially of the B_{r_d} multifractal type, as given by equation (3.3) and shown at the top left of Figure 3.3.

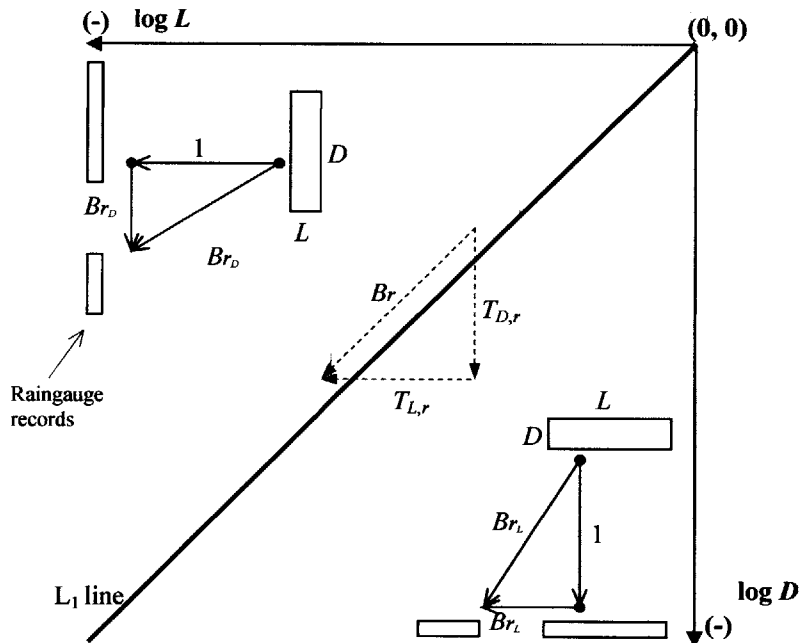


Figure 3.3: Approximate scaling relations.

In the region around the L_1 line (for velocities u_{res} in the approximate range $[1/5, 5]$), equations (3.2) and (3.3) do not apply (Veneziano and Furcolo, 2002b). Rather, there are complicated transformations, say $T_{D,r}$ and $T_{L,r}$ in the directions of the $\log(D)$ and $\log(L)$ axes, which in combination produce Br multifractal scaling; see dashed triangle in Figure 3.3.

Next, we consider how the T -year value $i(L, D, T)$ of the process $I(t|L, D)$ scales with L and D in the very high and very low velocity regions, where equations (3.2) and (3.3) hold. In the very high velocity region equation (3.2) holds, and recalling equations (2.45) and (2.50) from the Veneziano and Furcolo analysis, we obtain

$$i(L, D, T) \propto \begin{cases} L^{-\gamma_1} T^{1/q_1} & , \text{ for } T \text{ finite and } L \rightarrow 0 \\ L^{-1} T^{1/q^*(d)} & , \text{ for } L \text{ finite and } T \rightarrow \infty \end{cases} \quad (3.4)$$

Notice that the analysis of Veneziano and Furcolo (2002a) is for temporal rainfall (i.e. $d = 1$ and thus $q^* = q^*(1)$), whereas in equation (3.4) $q^* = q^*(d)$ with d that depends on the Euclidean dimension of the rainfall observing region ($d = 2$ for rainfall observed along a line segment, $d = 3$ for rainfall observed in a square region).

In the very low velocity region equation (3.3) holds, and recalling again equations (2.45) and (2.50), we obtain

$$i(L, D, T) \propto \begin{cases} D^{-\gamma_1} T^{1/q_1} & , \text{ for } T \text{ finite and } D \rightarrow 0 \\ D^{-1} T^{1/q^*(d)} & , \text{ for } D \text{ finite and } T \rightarrow \infty \end{cases} \quad (3.5)$$

Similarly to equation (3.4), when L is finite $q^* = q^*(3)$ for rainfall observed in a square region, and $q^* = q^*(2)$ for observation along a line segment. When $L \rightarrow 0$ (i.e. rainfall at a point), rainfall is a 1D process in time and $q^* = q^*(1)$.

Next we use equations (3.4), and (3.5) to derive expressions for the ARF. We denote by $i(D, T)$ the T -year rainfall intensity at a point for averaging duration D and write,

$$i(L, D, T) = \eta(L, D, T) i(D, T) \quad (3.6)$$

where $\eta(L, D, T)$ is the ARF we want to obtain.

In the very low velocity region, equation (3.5) gives,

$$\eta(L, D, T) \propto \begin{cases} 1 & , \text{ for } T \text{ finite and } D \rightarrow 0 \\ T^{[1/q^*(d) - 1/q^*(1)]} & , \text{ for } D \text{ finite and } T \rightarrow \infty \end{cases} \quad (3.7)$$

whereas in the very high velocity region equations (3.4) and (3.5) give,

$$\eta(L, D, T) \propto \begin{cases} \left(\frac{L}{D}\right)^{-\gamma_1} & , \text{ for } T \text{ finite and } L \rightarrow 0 \\ \left(\frac{L}{D}\right)^{-1} T^{[1/q^*(d) - 1/q^*(1)]} & , \text{ for } L \text{ finite and } T \rightarrow \infty \end{cases} \quad (3.8)$$

where $d = 3$ for rainfall observed inside a square region, and $d = 2$ for rainfall observed along a line segment. The relations in equations (3.7) and (3.8) are illustrated schematically in Figure 3.4.

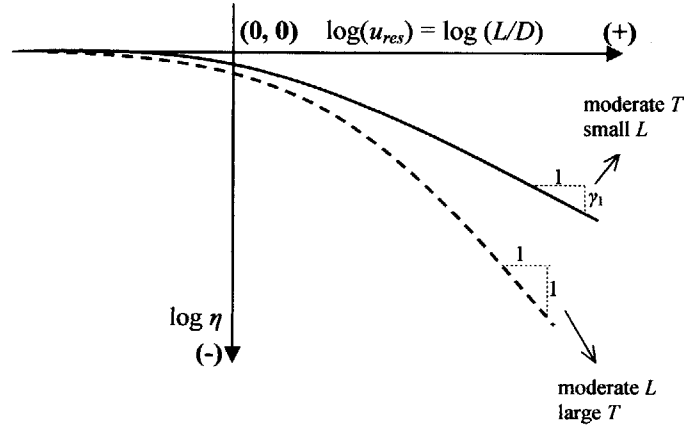


Figure 3.4: Behavior of the areal reduction factor η .

It is interesting that the ARF depends in an important way on the response velocity parameter u_{res} and on the return period T . Through $q^*(d)$, the geometry of the observation region affects the properties of the IDAF curves and the ARFs for large values of the return period T . Equations (3.7), (3.8) and Figure 3.4 indicate that when the response velocity v_{res} is low relative to the evolution velocity v_e the ARF is nearly constant with L/D and close to 1, whereas for relative fast response the ARF becomes a power function of L/D .

These theoretical results, which are validated numerically in Section 3.3.1, correspond to empirical observations. For example Figure 3.5 shows the ARF derived empirically by Koutsoyiannis (1997) for $D = 1$ hour (see also Section 1.2).

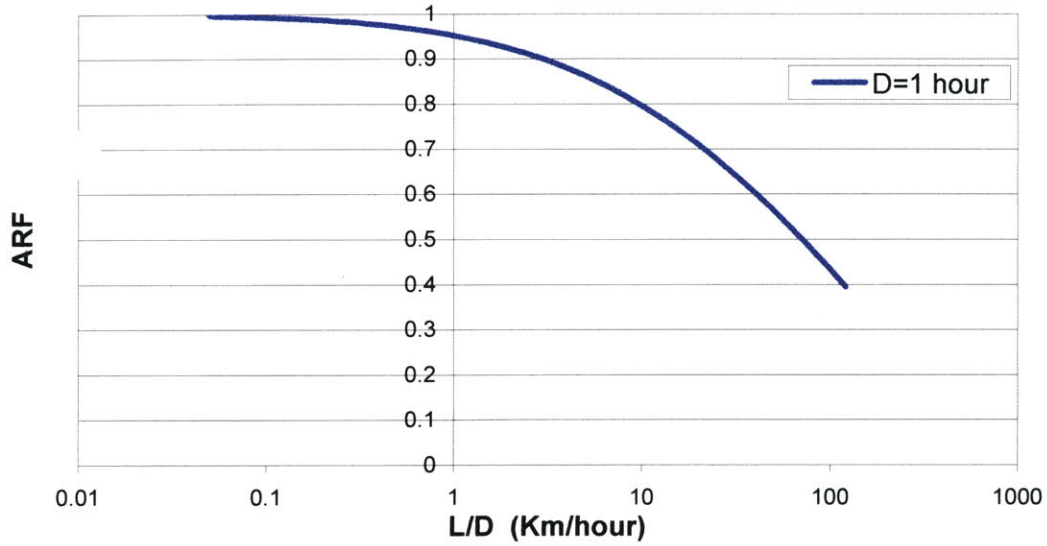


Figure 3.5: Koutsoyiannis ARF curves for duration of 1 hour, return period $T = 2-3$ years and areas up to 30 000 Km².

Evidently, the ARF increases as the ratio L/D decreases, and for values of $\left(\frac{L}{D} / \frac{L_e}{D_e}\right)$ less than about 1/5 the ARF is approximately 1.

Table 3.1 summarizes the previous results on the IDAF curves and the ARF for the case $v_{ad} = 0$.

Table 3.1: Scaling of IDAF curves and ARF with $u_{res}(v_{ad} = 0)$. The Euclidean dimension of the observation region, d , is included.

	Very low velocity region $u_{res} \ll 1$	Very high velocity region $u_{res} \gg 1$
Scaling	$I(t L, D) \approx_d B_{r_D} I(r_D t r_L L, r_D D), r_L, r_D \geq 1$ (no dependence on L)	$I(t L, D) \approx_d B_{r_L} I(r_L t r_L L, r_D D), r_L, r_D \geq 1$ (no dependence on D)
Extremes	$i(L, D, T) \propto \begin{cases} D^{-\gamma_1} T^{1/q_1}, & \text{for } \begin{cases} D \rightarrow 0 \\ T \text{ finite} \end{cases} \\ D^{-1} T^{1/q'(d)}, & \text{for } \begin{cases} D \text{ finite} \\ T \rightarrow \infty \end{cases} \end{cases}$ (no dependence on L)	$i(L, D, T) \propto \begin{cases} L^{-\gamma_1} T^{1/q_1}, & \text{for } \begin{cases} L \rightarrow 0 \\ T \text{ finite} \end{cases} \\ L^{-1} T^{1/q'(d)}, & \text{for } \begin{cases} L \text{ finite} \\ T \rightarrow \infty \end{cases} \end{cases}$ (no dependence on D)
$\eta(L, D, T)$	$\eta(L, D, T) \propto \begin{cases} 1, & \text{for } \begin{cases} D \rightarrow 0 \\ T \text{ finite} \end{cases} \\ T^{[1/q'(d) - 1/q'(1)]}, & \text{for } \begin{cases} D \text{ finite} \\ T \rightarrow \infty \end{cases} \end{cases}$	$\eta(L, D, T) \propto \begin{cases} \left(\frac{L}{D}\right)^{-\gamma_1}, & \text{for } \begin{cases} L \rightarrow 0 \\ T \text{ finite} \end{cases} \\ \left(\frac{L}{D}\right)^{-1} T^{[1/q'(d) - 1/q'(1)]}, & \text{for } \begin{cases} L \text{ finite} \\ T \rightarrow \infty \end{cases} \end{cases}$

3.1.2 Finite dressing and intermediate geometries of the observation region

In Section 3.1.1 we studied the properties of the IDAF curves and the ARF assuming that space-time rainfall intensity is an infinitely dressed multifractal process. We found that for T finite the shape of the rainfall collecting region does not affect the scaling properties of the IDAF curves and the ARF; see Table 3.1. Also, for $T \rightarrow \infty$ and rectangular geometry of the rainfall collecting region, the IDAF curves and ARFs have scaling properties that do not depend on the shape of the region; see Table 3.1. However, natural processes are not infinitely dressed, and therefore one should rather approximate space-time rainfall intensity as a partially dressed quantity than an infinitely dressed one.

In contrast to the behaviour of the marginal distribution of an infinitely dressed measure, which depends only on the dimension of the observation space d , the marginal distribution of a partially dressed measure depends also on the shape of the observation region, and the elongation of the region; see below. The latter is an important parameter for the tail properties of partial dressing factors, and thus for the same properties of partially dressed densities. For simplicity, we study those properties outside the context of rainfall, using a 2D cascade process of multiplicity m . Then, we discuss the implications for space-time rainfall, treated as a 3D

multiplicative cascade. We obtain properties of the IDAF curves and ARFs for rectangular rainfall collecting regions and finite values of the return period T .

Define ε_{L_1, L_2} to be the average measure density inside a $L_1 \times L_2$ rectangular observation region with $L_1 \geq L_2$; see Figure 3.6.

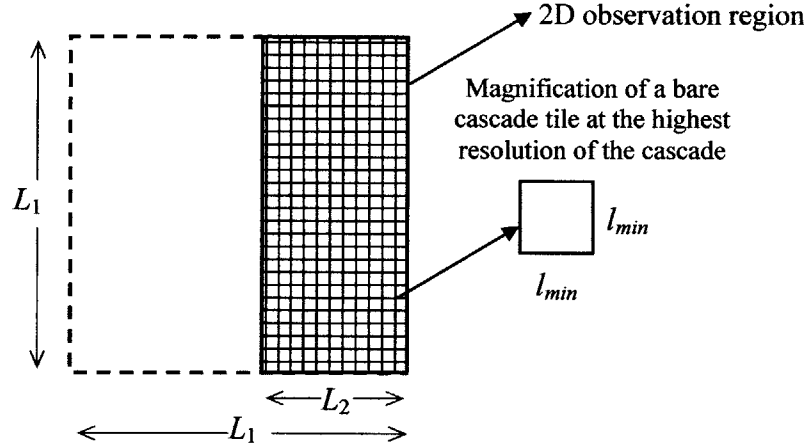


Figure 3.6: 2D observation region with linear dimensions L_1 and L_2 , included in a square region of size L_1 . l_{min} is the linear dimension of the bare tiles at the highest resolution of the cascade.

Denote by l_{min} the linear size of a bare cascade tile at the highest resolution of the cascade; see Figure 3.6. The ratios L_1/L_2 and L_2/l_{min} give the amount of spatial aggregation along each side of the observation region, and the parameters $n_{d1} = \log_m(L_1/L_2)$ and $n_{d2} = \log_m(L_2/l_{min})$ give the associated numbers of dressing levels. One can express ε_{L_1, L_2} by,

$$\varepsilon_{L_1, L_2} =_d \varepsilon_{L_{bare}} Z_{nd_1, nd_2} \quad (3.9)$$

where $\varepsilon_{L_{bare}}$ is the bare measure density inside the square region of side L_1 (see Figure 3.6), and Z_{nd_1, nd_2} is the partial dressing factor inside the rectangular region with side lengths L_1 and L_2 . Next we study the tail behaviour of the partially dressed density ε_{L_1, L_2} for different values of the parameters n_{d1} and n_{d2} .

First we examine cases with limiting values of n_{d1} and n_{d2} . For $n_{d1} = 0$ and $n_{d2} = 0$ the observation region is a square, and the measure ε_{L_1, L_1} is bare. Thus the tail behaviour of the distribution of ε_{L_1, L_1} is not algebraic; case (c) in Figure 3.7. For $n_{d1} = 0$ and $n_{d2} \rightarrow \infty$, the observation region is again a square, but the measure ε_{L_1, L_1} is infinitely dressed in both dimensions. In this case the tail behaviour of ε_{L_1, L_1} is identical to that of the two-dimensional dressing factor $Z_{(d=2)}$ and $q^* = q^*(2)$; case (b) in Figure 3.7. For $n_{d1} \rightarrow \infty$ and $n_{d2} = 0$, the

observation region is a line segment of length L_1 and the measure $\varepsilon_{L_1, l_{min}}$ is infinitely dressed in one spatial dimension. Therefore, the tail behaviour of $\varepsilon_{L_1, l_{min}}$ is the same as that of the one dimensional dressing factor, $Z_{(d=1)}$; case (a) in Figure 3.7.

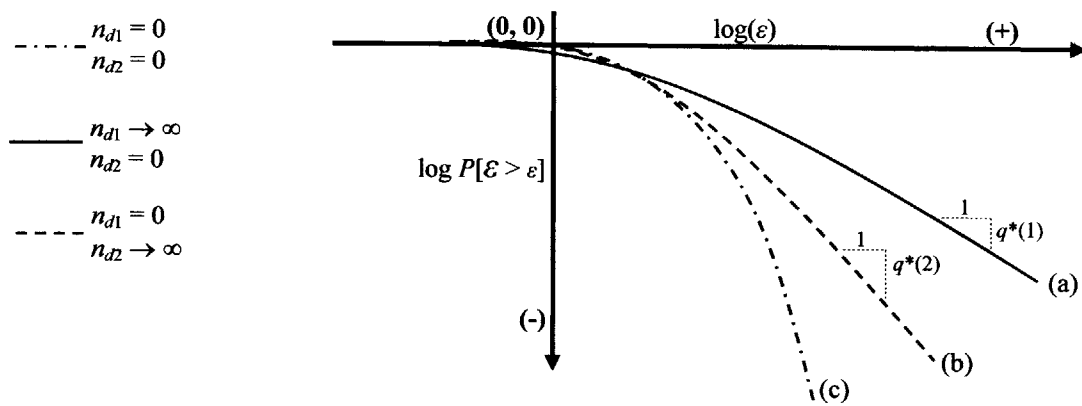


Figure 3.7: Complementary Cumulative Distribution Function (CCDF) of the measure ε_{L_1, L_2} for limiting values of the parameters n_{d1} and n_{d2} . (a) $q^*(1)$ tail behaviour, (b) $q^*(2)$ tail behaviour, (c) no algebraic tail behaviour (bare measure).

Next we consider intermediate (rectangular) geometries and cases with finite dressing. When $n_{d1} = 0$ and n_{d2} is finite, the observation region is a square and the spatial dressing is finite. The distribution of ε_{L_1, L_1} is intermediate between curves (b) and (c) in Figure 3.7. The distribution further depends on the value of n_{d2} . Figure 3.8 shows qualitatively the behaviour of ε_{L_1, L_1} for different n_{d2} .

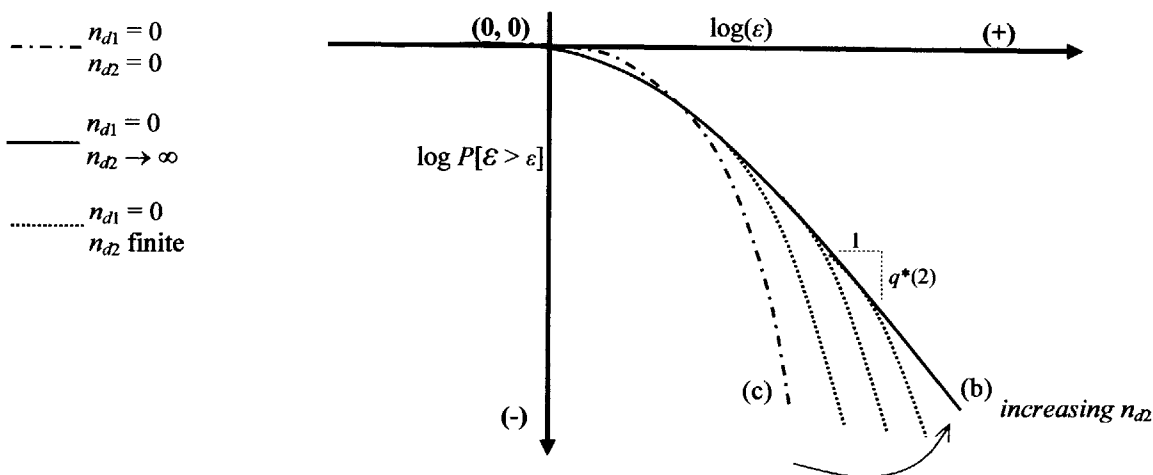


Figure 3.8: Complementary Cumulative Distribution Function (CCDF) of the measure ε_{L_1, L_2} for $n_{d1} = 0$ and n_{d2} finite.

When $n_{d2} = 0$ and n_{d1} is finite, the observation region is a line segment and dressing is one-dimensional and finite. The measure $\varepsilon_{L1,lmn}$ has a slope intermediate between curves (a) and (c) in Figure 3.7. Figure 3.9 shows qualitatively the behaviour of $\varepsilon_{L1,lmn}$ for different values of n_{d1} .

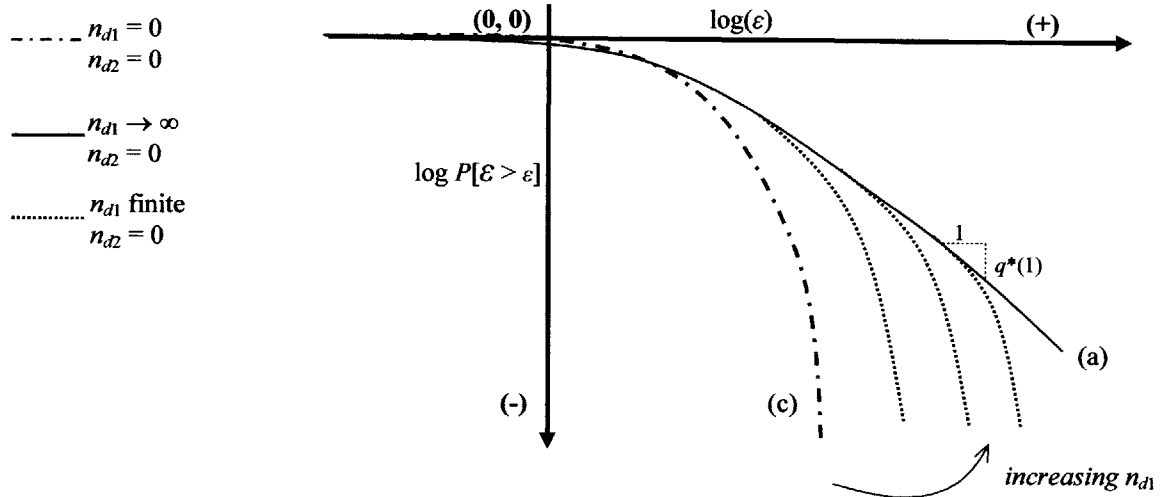


Figure 3.9: Complementary Cumulative Distribution Function (CCDF) of the measure $\varepsilon_{L1,L2}$ for $n_{d2} = 0$ and n_{d1} finite.

When both n_{d1} and n_{d2} are finite, the observation region is elongated. In this case spatial dressing is finite and partly one-dimensional, partly two-dimensional. The distribution of $\varepsilon_{L1,L2}$ has properties from all curves in Figure 3.7. These properties depend on n_{d1} and n_{d2} . Figure 3.10 shows qualitatively how the behaviour of $\varepsilon_{L1,L2}$ depends on n_{d1} and n_{d2} . Notice that Regions 1 and 2, where $\varepsilon_{L1,L2}$ has different algebraic behaviours, have sizes that are increasing functions of n_{d1} and n_{d2} , respectively. For n_{d2} large (say larger than 5) and n_{d1} small (say less than 5) Region 1 tends to disappear and Region 2 dominates, whereas for n_{d2} small (say < 5) and n_{d1} large (say > 5) Region 1 dominates and Region 2 tends to disappear.

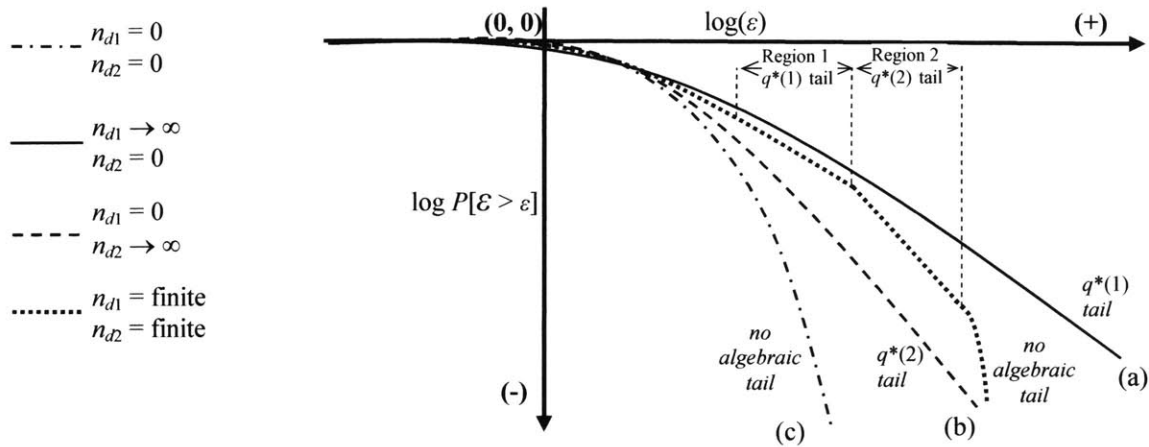


Figure 3.10: Schematic behaviour of the complementary cumulative distribution function of the measure ε_{L_1, L_2} for given values of n_{d1} and n_{d2} .

We now return to space-time rainfall, which we view as a 3D multiplicative cascade process (two spatial dimensions plus time) of multiplicity m . In this case, the observation space is a parallelepiped with spatial dimensions L_1 and L_2 , and temporal dimension D ; see Figure 3.11.

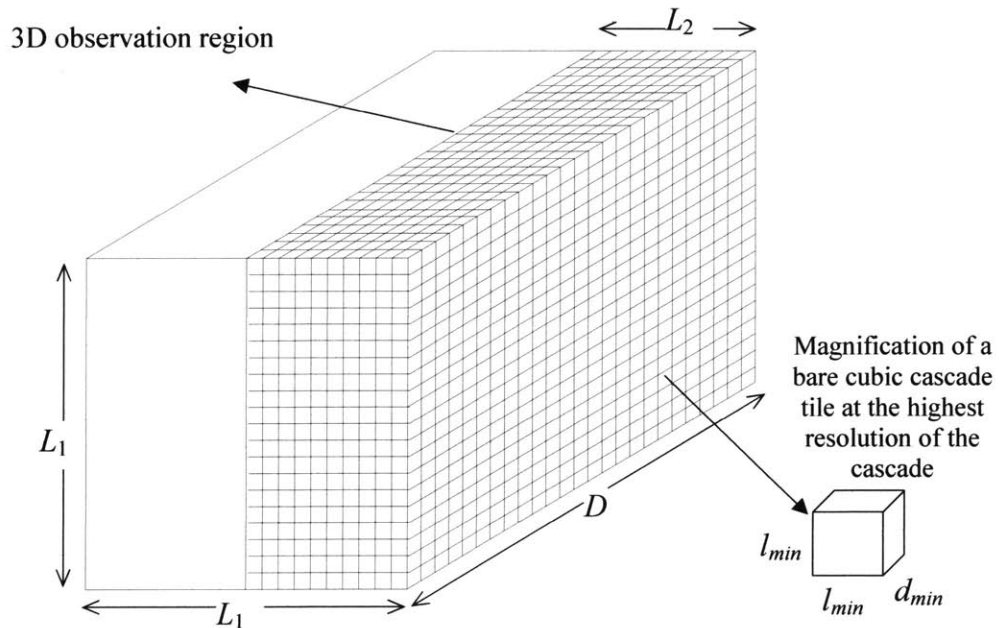


Figure 3.11: 3D observation region with linear dimensions L_1 and L_2 and temporal dimension D . l_{min} and d_{min} are respectively the spatial and temporal dimension of the bare cubic tiles at the highest resolution of the cascade.

The average rainfall intensity inside this parallelepiped, denoted by $i_{L_1, L_2, D}$, is a partially dressed measure with tail properties that depend on the parameters n_{d1} and n_{d2} , defined earlier, and on

$n_{d3} = \log_m(D/d_{min})$, where d_{min} is the temporal size of a tile at the highest resolution of the cascade; see Figure 3.11. These three parameters define the shape of the rainfall collecting region, as well as the number of 1D, 2D and 3D dressing levels. Typical values of d_{min} for rainfall range from 1-5 min (Olson *et al.* 1993, 1995), whereas a similar range for l_{min} does not exist in the literature. However, for typical hydrologic applications one can accept l_{min} to be of about 1 Km.

Figure 3.12 shows qualitatively the dependence of the marginal distribution of $i_{L_1,L_2,D}$ on n_{d1} , n_{d2} and n_{d3} . Notice that Regions 1, 2 and 3, where $i_{L_1,L_2,D}$ has different algebraic behaviours, have sizes that depend on n_{d1} , n_{d2} and n_{d3} .

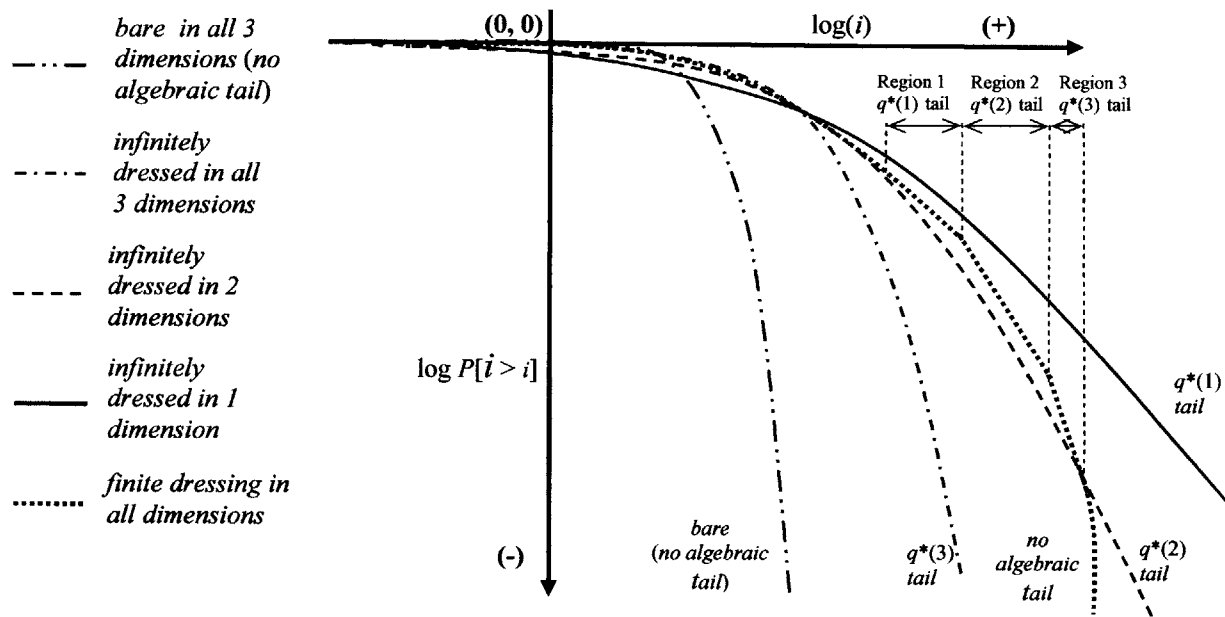


Figure 3.12: Schematic behaviour of the complementary cumulative distribution function of the average rainfall intensity $i_{L_1,L_2,D}$ for given values of n_{d1} , n_{d2} and n_{d3} .

One can use the above results to qualitatively assess the effect of the shape of the rainfall collecting region on IDAF and ARF scaling.

Denote by $i(L_1,L_2,D,T)$ the average rainfall intensity inside the space time region (L_1,L_2,D) with return period T . Also define $\eta(L_1,L_2,D,T)$ to be the associated ARF. In general, $i(L_1,L_2,D,T)$ and $\eta(L_1,L_2,D,T)$ scale with T as $i(L_1,L_2,D,T) \propto T^a$ and $\eta(L_1,L_2,D,T) \propto T^{-b}$; see Section 3.1.1. For $T \rightarrow 0$, a and b equal zero, whereas for $T \rightarrow \infty$, $a = 1/q^*(d)$ and $b = 1/q^*(1) - 1/q^*(d)$, where d is the Euclidean dimension of the observation space ($d=2$ for rainfall observed along a line segment, $d=3$ for rainfall observed over a square or a disc); see Section 3.1.1. This means that for $T \rightarrow \infty$ and rectangular rainfall collecting regions, $d=3$ and the shape of the region does not

affect the asymptotic properties of the IDAF curves and the ARFs. However, for intermediate values of T there is a significant dependence of the parameters a and b on the shape of the observation region. Specifically, a is larger for elongated basins relative to regular ones and decreases as T increases; see Figure 3.13. This decrease is faster for smaller and more symmetric basins.

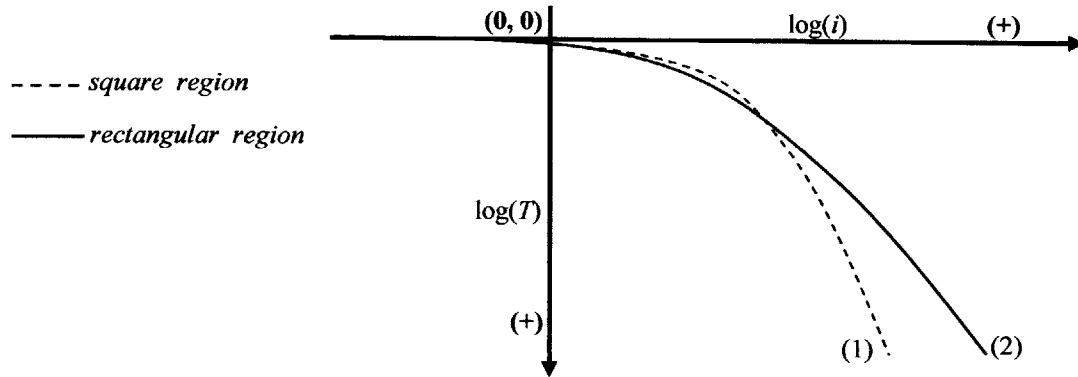


Figure 3.13: Schematic behaviour of the average rainfall intensity $i_{L_1, L_2, D}$ as a function of the return period T , for two different geometries of the observation region: (1) a square region ($L_1=L_2$), and (2) a rectangular region ($L_1>L_2$). The averaging area and duration are kept constant.

On the other hand, b is larger for regular basins relative to elongated ones and increases as T increases; see Figure 3.14. This increase is faster for smaller and more symmetric basins.

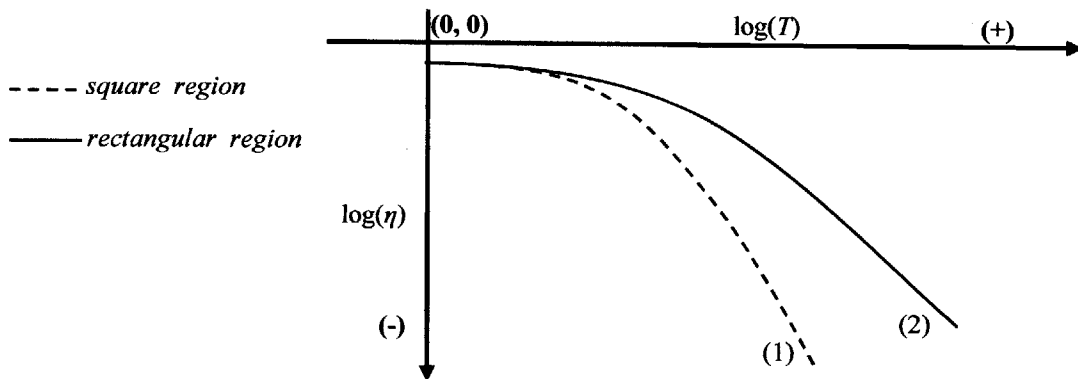


Figure 3.14: Schematic behaviour of the Areal Reduction Factor $\eta_{L_1, L_2, D}$ as a function of the return period T , for two different geometries of the observation region: (1) a square region ($L_1=L_2$), and (2) a rectangular region ($L_1>L_2$). The averaging area and duration are kept constant.

Notice that the tail of curves (1) and (2) in Figures 3.13 and 3.14 may or may not be of the power law type depending on the number of 1D, 2D and 3D dressing levels.

One concludes that, for intermediate values of T the shape of the rainfall collecting region becomes influential. The ARF decreases faster for regularly shaped basins relative to elongated ones. The rate of this decrease further depends on T with higher rates for larger values of T .

3.2 The Effect of Advection

In the previous section, we studied the scaling properties of the IDAF curves and the ARF with L , D and T for $u_{ad} = 0$ (or when collecting rainfall in a Lagrangian reference system). We found that a key parameter describing the behaviour of the IDAF curves and the ARFs is the ratio $u_{res} = v_{res}/v_e$ between the response velocity $v_{res} = L/D$ and the evolution velocity of the rainfall field.

Next we study the effect of advection. We define the ‘‘advection velocity parameter’’ as the dimensionless ratio $u_{ad} = v_{ad}/v_e$. Rainfall is considered to be isotropically multifractal, as before. Again we set $L_e = 1$ and $D_e = 1$. Thus $v_e = 1$ and $u_{res} = v_{res}$. Notice that in an Eulerian reference the rainfall distribution remains multifractal with scaling properties identical to those in a Lagrangian reference. This is so because isotropically scaled (homothetical) space-time regions remain homothetical under constant advection velocity. For example, Figure 3.15 shows the effect of advection on a cylindrical rainfall averaging region in space-time. The cylinder becomes slanted in the direction of u_{ad} .

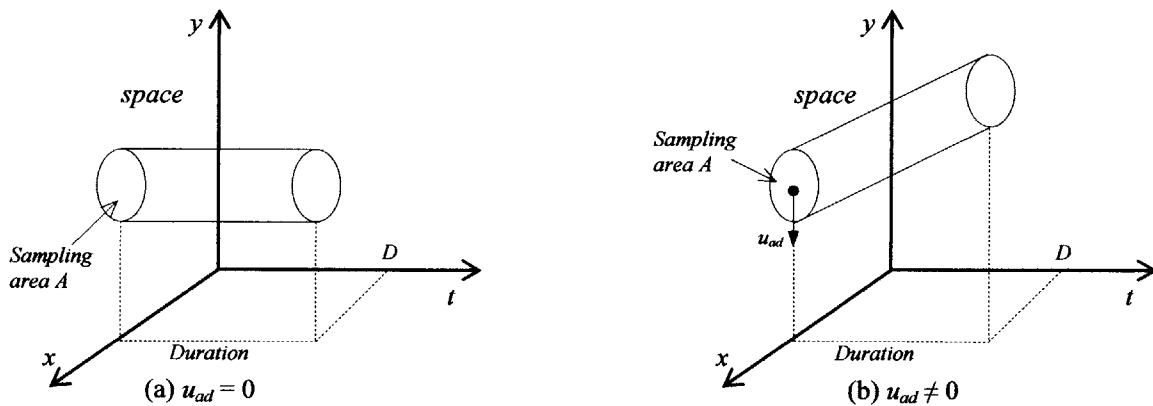


Figure 3.15: The effect of advection. Regions where rainfall intensity is averaged for (a) $u_{ad} = 0$ and (b) $u_{ad} \neq 0$; (x, y, t) are Lagrangian coordinates.

In what follows we analyze how advection affects the sampling region in space-time and the return period T when changing from an Eulerian to a Lagrangian coordinate system. We do so separately for three spatial sampling cases: sampling at a geographical point, a line segment or over a disc. This transformation allows us to then use the results of Section 3.1 (for $\mathbf{v}_{ad} = \mathbf{0}$), which apply in a Lagrangian framework for any \mathbf{v}_{ad} .

3.2.1 Sampling at a point

Suppose that the sampling area is small enough that it may be approximated as a point. As shown in Figure 3.16, when sampling an advected field over a duration D , the sampling segment in a Lagrangian framework has length D' given by

$$D' = \sqrt{D^2 + D^2 (u_{ad})^2} = D \sqrt{1 + u_{ad}^2} \quad (3.10)$$

where $\sqrt{1 + u_{ad}^2}$ can be seen as a correction factor for D when passing from an Eulerian to a Lagrangian coordinate system.

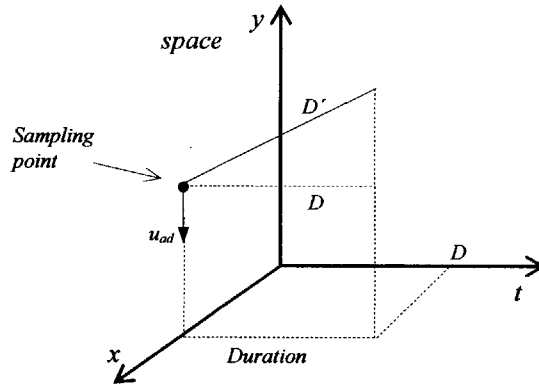


Figure 3.16: Sampling at a point in a time interval of duration D .

In analogy to equation (3.10), the return period T' in a Lagrangian framework that corresponds to T in an Eulerian framework is

$$T' = T \sqrt{1 + u_{ad}^2} \quad (3.11)$$

Equations (3.10) and (3.11) indicate that the effect of advection on the IDF curves is to increase both the effective averaging time and the return period by a factor $\sqrt{1 + u_{ad}^2}$. Therefore, if the IDF values for $u_{ad} = 0$ vary with D and T as $D^{-a} T^b$ where a and b are constants such that $a > b$, then the IDF curves for $u_{ad} \neq 0$ are displaced downward by a factor $(1 + u_{ad}^2)^{(a-b)/2}$. The latter is shown schematically in Figure 3.17.

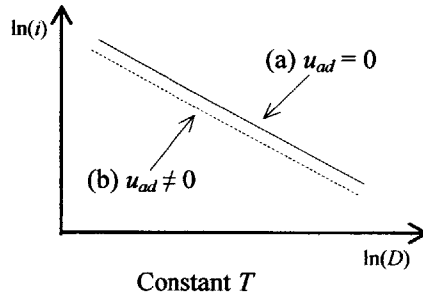


Figure 3.17: Expected displacement of the IDF curves due to advection.

In Section 2.3 we showed that a varies between γ_1 and 1. Also, for $a = \gamma_1$ then $b = 1/q_1$ and for $a = 1$ then $b = 1/q^*(1)$. Thus the inequality $a > b$ is always maintained and the IDF curves for $u_{ad} \neq 0$ are displaced downwards as shown schematically in Figure 3.17.

3.2.2 Sampling on a segment line

Suppose that rainfall is observed on a straight line segment of length L . In this case, the averaging region in space and time is a parallelogram whose shape and size depends on L , D and the amplitude and direction of the advection velocity vector; see Figure 3.18.

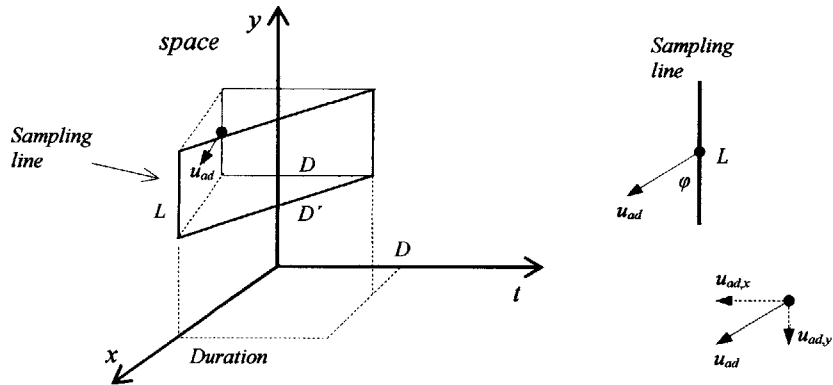


Figure 3.18: Sampling along a line in an Eulerian reference system.

If $0 \leq \varphi \leq \pi/2$ is the angle between the advection velocity vector u_{ad} and the sampling line L , then one can decompose the advection velocity vector into a component normal to L ,

$$u_{ad,x} = u_{ad} \sin\varphi \quad (3.12)$$

and a component parallel to L ,

$$u_{ad,y} = u_{ad} \cos\varphi \quad (3.13)$$

The normal component $u_{ad,x}$ affects the size of the sampling region in space and time but not its shape which remains rectangular; see Figure 3.19. Under only $u_{ad,x}$, the sides of this rectangular observation region have lengths,

$$\begin{cases} L' = L \\ D' = D\sqrt{1+u_{ad,x}^2} \end{cases} \quad (3.14)$$

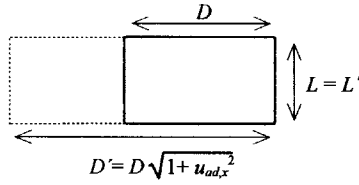


Figure 3.19: Effect of $u_{ad,x}$ on the size of the sampling region in space-time.

By contrast, the parallel component $u_{ad,y}$ affects the shape but not the size of the sampling region. The region is now a parallelogram with side lengths L and $D' = D\sqrt{1+u_{ad,y}^2}$ and the value of the “height” L' in Figure 3.20 is $L' = L/\sqrt{1+u_{ad,y}^2}$.

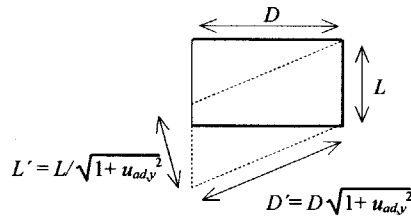


Figure 3.20: Effect of $u_{ad,y}$ on the shape of the sampling region.

The Lagrangian observation region under the combined effect of $u_{ad,x}$ and $u_{ad,y}$ is a parallelogram with side lengths L and $D' = D\sqrt{1+u_{ad}^2}$ and the value of the height L' in Figure 3.21 is $L' = L/\sqrt{1+u_{ad,y}^2}$.

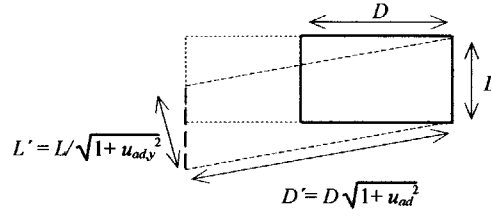


Figure 3.21: Effect of u_{ad} on the shape and size of the sampling region.

The Lagrangian return period is given by

$$T' = T \sqrt{1 + u_{ad}^2} \quad (3.15)$$

To understand the implications of advection on the IDAF curves and the ARF we consider two limiting cases. One is $u_{res} \gg 1$ (very high response velocity) and the other is $u_{res} \ll 1$ (very low response velocity).

For $u_{res} \gg 1$ the parallelogram is highly elongated in the spatial direction and one can approximate it with a rectangle as shown in Figure 3.22. Thus L , D and T are translated to L' , D' , and T' given by

$$\begin{cases} L' = L \\ D' = D \sqrt{1 + u_{ad,x}^2} \\ T' = T \sqrt{1 + u_{ad,x}^2} \end{cases} \quad (3.16)$$

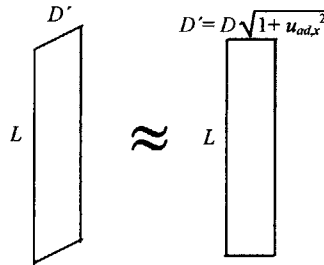


Figure 3.22: Approximation of the observation region with a rectangle when $u_{res} \gg 1$.

In the other limiting case, $u_{res} \ll 1$, the parallelogram is highly elongated in the temporal direction and can be approximated by a rectangle as shown in Figure 3.23. Thus,

$$\begin{cases} L' = L\sqrt{1+u_{ady}^2} \\ D' = D\sqrt{1+u_{ad}^2} \\ T' = T\sqrt{1+u_{ad}^2} \end{cases} \quad (3.17)$$

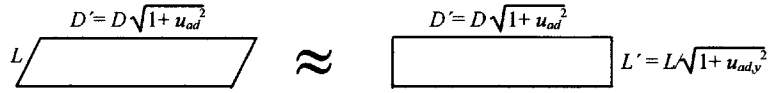


Figure 3.23: Approximation of the observation region with a rectangle when $u_{res} \ll 1$.

Hence in the case of sampling along a line, the effective values L' , D' and T' depend not only on the magnitude of the advection velocity, but also on the direction of advection relative to the sampling line.

3.2.3 Sampling over a disc

Contrary to the case of observation on a line, when sampling over a disc of diameter L the direction of the advection velocity vector has no effects. This is so because the observation region has radial symmetry; see Figure 3.24.

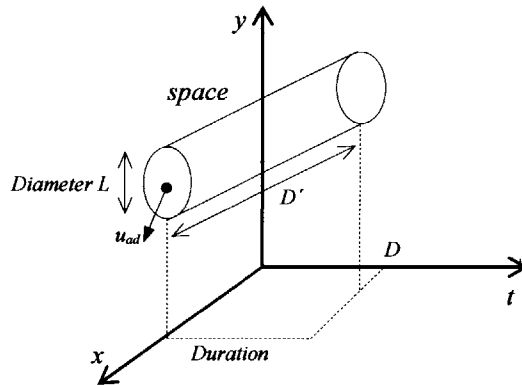


Figure 3.24: Sampling over a disc of diameter L in an Lagrangian reference system.

Equation (3.18) gives the effects of the advection velocity on L , D and T for the limiting cases when $u_{res} \gg 1$ and $u_{res} \ll 1$.

$$\left[\begin{array}{l} u_{res} \gg 1 \\ u_{res} \ll 1 \end{array} \right. \left\{ \begin{array}{l} L' = L \\ D' = D \\ T' = T \end{array} \right. \left\{ \begin{array}{l} (L')^2 = L^2 \sqrt{1 + u_{ad}^2} \\ D' = D \sqrt{1 + u_{ad}^2} \\ T' = T \sqrt{1 + u_{ad}^2} \end{array} \right. \quad (3.18)$$

3.2.4 Effect of Advection on the IDAF curves and the ARFs

One can use the results in equations (3.16), (3.17) and (3.18) to modify Table 3.1 and include the effects of advection on the IDAF curves and the ARFs for two limiting geometries of drainage basins: Very elongated basins (i.e. Length Width⁻¹ >> 1), and relatively symmetric basins (i.e. Length Width⁻¹ ≈ 1). Very elongated basins can be approximated as segment lines along which rainfall is observed; see Section 3.2.2. On the other hand, relatively symmetric basins can be approximated as observation discs; see Section 3.2.3. The resulting expressions are listed in Table 3.2 for very elongated basins, and in Table 3.3 for relatively symmetric basins.

Table 3.2: Scaling of the IDAF curves and ARFs with u_{res} for very elongated basins; the effect of advection is included ($u_{ad} \neq 0$). $d = 2$ for $n_{d1} > 5$ and $n_{d2} < 5$, and $d = 3$ for $n_{d1} < 5$ and $n_{d2} > 5$; see Section 3.1.2.

	Very low velocity region $u_{res} \ll 1$	Very high velocity region $u_{res} \gg 1$
Scaling	$I(t L, D) \approx_d B_{r_i} I(r_d t r_L L, r_D D), r_L, r_D \geq 1$ (no dependence on L)	$I(t L, D) \approx_d B_{r_i} I(r_L t r_L L, r_D D), r_L, r_D \geq 1$ (no dependence on D)
Extremes	$i(L, D, T, u_{ad}) \propto$ $\left\{ \begin{array}{l} (1+u_{ad}^2)^{(1/q_1 - \gamma_1)/2} D^{-\gamma_1} T^{1/q_1}, \text{ for } \begin{cases} D \rightarrow 0 \\ T \text{ finite} \end{cases} \\ (1+u_{ad}^2)^{[1/q^*(d) - 1]/2} D^{-1} T^{1/q^*(d)}, \text{ for } \begin{cases} D \text{ finite} \\ T \rightarrow \infty \end{cases} \end{array} \right.$ (no dependence on L)	$i(L, D, T, u_{ad}) \propto$ $\left\{ \begin{array}{l} (1+u_{ad,x}^2)^{0.5/q_1} L^{-\gamma_1} T^{1/q_1}, \text{ for } \begin{cases} L \rightarrow 0 \\ T \text{ finite} \end{cases} \\ (1+u_{ad,x}^2)^{0.5/q^*(d)} L^{-1} T^{1/q^*(d)}, \text{ for } \begin{cases} L \text{ finite} \\ T \rightarrow \infty \end{cases} \end{array} \right.$ (no dependence on D)
$\eta(L, D, T, u_{ad})$	$\eta(L, D, T, u_{ad}) \propto$ $\left\{ \begin{array}{l} 1, \text{ for } \begin{cases} D \rightarrow 0 \\ T \text{ finite} \end{cases} \\ ((1+u_{ad}^2)^{0.5} T)^{[1/q^*(d) - 1/q^*(1)]}, \text{ for } \begin{cases} D \text{ finite} \\ T \rightarrow \infty \end{cases} \end{array} \right.$	$\eta(L, D, T, u_{ad}) \propto$ $\left\{ \begin{array}{l} \left(\frac{1+u_{ad,x}^2}{(1+u_{ad}^2)^{1-\gamma_1/q_1}} \right)^{0.5/q_1} \left(\frac{L}{D} \right)^{-\gamma_1}, \text{ for } \begin{cases} L \rightarrow 0 \\ T \text{ finite} \end{cases} \\ \left(\frac{(1+u_{ad,x}^2)^{1/q^*(d)}}{(1+u_{ad}^2)^{[1/q^*(d) - 1/q^*(1)]}} \right)^{0.5} \left(\frac{L}{D} \right)^{-1} T^{[1/q^*(d) - 1/q^*(1)]}, \text{ for } \begin{cases} L \text{ finite} \\ T \rightarrow \infty \end{cases} \end{array} \right.$

Table 3.3: Scaling of the IDAF curves and ARFs with u_{res} for relatively symmetric basins; the effect of advection is included ($u_{ad} \neq 0$).

	Very low velocity region $u_{res} \ll 1$	Very high velocity region $u_{res} \gg 1$
Scaling	$I(t L, D) \approx_d B_{r_i} I(r_i t r_i L, r_i D), r_i, r_D \geq 1$ (no dependence on L)	$I(t L, D) \approx_d B_{r_i} I(r_i t r_i L, r_i D), r_i, r_D \geq 1$ (no dependence on D)
Extremes	$i(L, D, T, u_{ad}) \propto$ $\begin{cases} (1+u_{ad}^2)^{(1/q_1 - \gamma)/2} D^{-\gamma} T^{1/q_1}, & \text{for } \begin{cases} D \rightarrow 0 \\ T \text{ finite} \end{cases} \\ (1+u_{ad}^2)^{[1/q^*(3) - 1]/2} D^{-1} T^{1/q^*(3)}, & \text{for } \begin{cases} D \text{ finite} \\ T \rightarrow \infty \end{cases} \end{cases}$ (no dependence on L)	$i(L, D, T, u_{ad}) \propto$ $\begin{cases} L^{-\gamma} T^{1/q_1}, & \text{for } \begin{cases} L \rightarrow 0 \\ T \text{ finite} \end{cases} \\ L^{-1} T^{1/q^*(3)}, & \text{for } \begin{cases} L \text{ finite} \\ T \rightarrow \infty \end{cases} \end{cases}$ (no dependence on D)
ARF(L, D, T, u_{ad})	$\eta(L, D, T, u_{ad}) \propto$ $\begin{cases} 1, & \text{for } \begin{cases} D \rightarrow 0 \\ T \text{ finite} \end{cases} \\ ((1+u_{ad}^2)^{0.5} T)^{[1/q^*(3) - 1/q^*(1)]}, & \text{for } \begin{cases} D \text{ finite} \\ T \rightarrow \infty \end{cases} \end{cases}$	$\eta(L, D, T, u_{ad}) \propto$ $\begin{cases} (1+u_{ad}^2)^{(\gamma - 1/q_1)/2} \left(\frac{L}{D}\right)^{-\gamma}, & \text{for } \begin{cases} L \rightarrow 0 \\ T \text{ finite} \end{cases} \\ (1+u_{ad}^2)^{[1 - 1/q^*(1)]/2} \left(\frac{L}{D}\right)^{-1} T^{[1/q^*(3) - 1/q^*(1)]}, & \text{for } \begin{cases} L \text{ finite} \\ T \rightarrow \infty \end{cases} \end{cases}$

Notice that the expressions in Table 3.2 include the parameter $q^*(d)$ instead of $q^*(2)$, which is the theoretically correct value since rainfall collection is along a line segment. Use of the general space-time dimension d indicates that one should consider independently the shape of an elongated region for defining the dimension of the observation space (i.e. $d = 2$ or $d = 3$), and for selecting the right prefactor to account for advection effects. For example an elongated rainfall collecting region may be approximated as a segment line to account for advection effects, however the dimension of the observation space, which characterizes the IDAF and ARF scaling under no advection conditions (i.e. $v_{ad} = 0$), may still be with high accuracy $d = 3$, as shown in Section 3.1.2.

For moderate values of the return period T , one should substitute $1/q^*(d)$ in the expressions of Table 3.2 and $1/q^*(3)$ in the expressions of Table 3.3 with the parameter a , discussed in Section 3.1.2. This parameter accounts for the shape of the rainfall collecting region, which becomes influential for moderate T .

Figure 3.25 shows qualitatively the effect of advection on the ARF curves. For $u_{res} \ll 1$ and T large, the ARF depends on the magnitude of the advection velocity, whereas for T moderate the ARF is not affected by u_{ad} and remains constant with L/D and close to 1. For $u_{res} \gg 1$ and T

either small or large, the ARF remains a power function of L/D but the prefactor depends on the magnitude of u_{ad} ; for a numerical validation see Section 3.3.2.

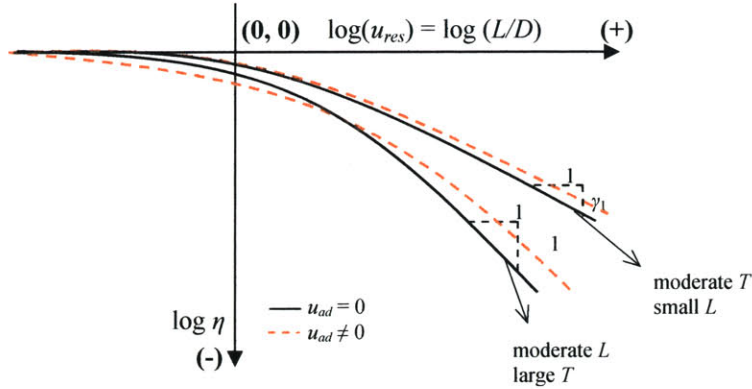


Figure 3.25: Behavior of the areal reduction factor η for $u_{ad} = 0$ and $u_{ad} \neq 0$.

3.3 Numerical validation

In the previous sections we derived scaling properties of the IDAF curves and the ARFs with the size of the region L , the period of aggregation D and the return period T . This was done for two separate cases: (1) no advection of the rainfall field (Section 3.1), and (2) constant advection velocity (Section 3.2).

Here we validate numerically the theoretical results obtained in the previous sections, first for the case with $\mathbf{v}_{ad} = \mathbf{0}$ and then for the case with $\mathbf{v}_{ad} \neq \mathbf{0}$.

3.3.1 Numerical validation for the case without advection

To validate the theoretical results in Section 3.1 we use two types of multifractal cascade models in two spatial dimensions plus time. The first cascade model has lognormal generator, whereas the second model has beta-lognormal generator (for more information on beta-lognormal cascades see Section 4.1.3). Both cascades have multiplicity 2 in all dimensions.

3.3.1.1 Lognormal cascade

The generator of the cascade, B , has a lognormal distribution,

$$\ln(B) \sim N(-C_1 \ln(2), 2C_1 \ln(2)) \quad (3.19)$$

where $N(\mu, \sigma^2)$ is the normal distribution with mean value μ and variance σ^2 and C_1 is the so-called co-dimension coefficient.

To reduce the computational time needed, only the relevant part of the 3D cascade was generated; see Figure 3.26. The parallelepiped that is embedded in the 3D cascade has spatial dimensions $2^6 \times 2^6$ tiles and temporal dimension 2^9 tiles. This parallelepiped represents in an idealized way a rainy period (season) of the year. The size of 2^9 cascade tiles is assumed to represent the outer limit of multifractal rainfall behavior in both space and time.

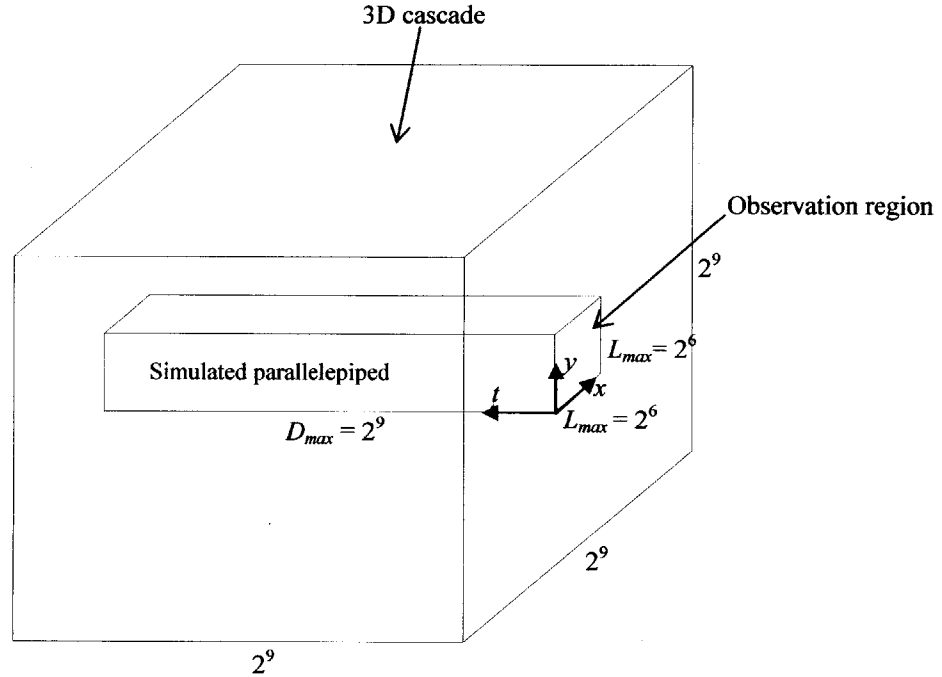


Figure 3.26: Schematic representation of the simulated region of the 3D cascade.

Numerical estimation of the ARF requires knowledge of area-averaged rainfall intensities at catchment scales, as well as at the raingauge scale. The latter may be assimilated to a point.

The cascade is generated down to the scale of unit space-time tiles and then “dressed” as described below.

Denote by $I_b(x, y, t)$ the bare rainfall intensity at the highest bare resolution, i.e. in the unit 3D tile centered at (x, y, t) . The dressed rainfall intensity at that same unit scale is obtained as,

$$I_{d,3}(x, y, t) =_d Z_{3D} I_b(x, y, t) \quad (3.20)$$

where Z_{3D} is the dressing factor of a 3D binary cascade with generator given by equation (3.19).

Consider now a raingauge at a point inside this tile, for example at location (x, y) . During the unit time interval centered at t , the dressed rainfall intensity measured by the raingauge, $I_{d,1}(x, y, t)$, is given by,

$$I_{d,1}(x, y, t) =_d Z_{1D} I_b(x, y, t) \quad (3.21)$$

where Z_{1D} is the dressing factor of a 1D binary cascade with generator identical to that of Z_{3D} .

For each simulated season one can estimate numerically the ARFs for different values of L and D . These ARFs have return period $T = 1$ season or 1 year. Estimation is through,

$$ARF(L, D) = \frac{IDAF(L, D)}{IDF(D)} = \frac{E \left[\max_i \left(\int_L \int_L \int_{D_i} I_{d,3}(x, y, t) dt dx dy \right) \right]}{E \left[\max_i \left(\int_{D_i} I_{d,1}(x, y, t) dt \right) \right]}, \text{ for } L \leq L_{max}, D_i \leq D_{max} \quad (3.22)$$

where $E[.]$ denotes averaging over different seasons and spatial locations of the catchment or raingauge, and i is the index of cascade tile of duration D inside each season; see Figure 3.27. To reduce variability among different realizations, we have averaged over 10 simulated seasons.

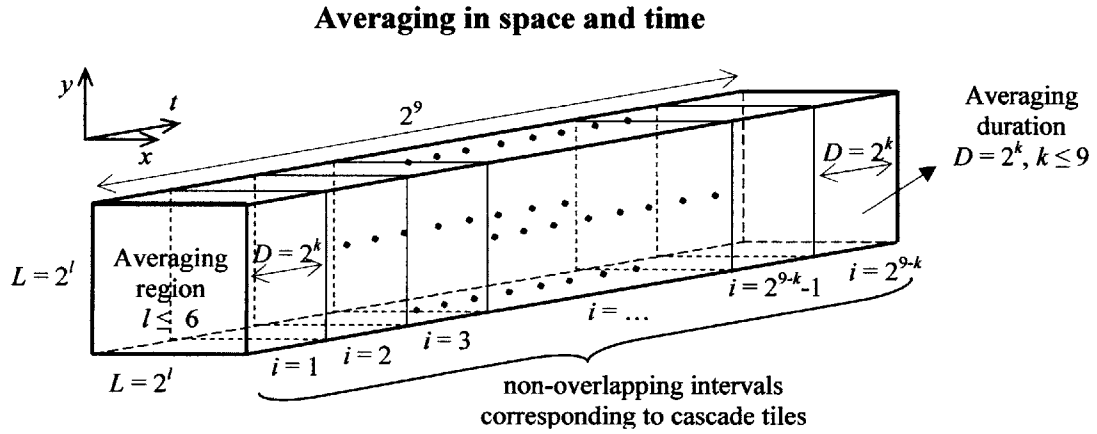


Figure 3.27: Simulation procedure using a binary 3D cascade.

Figure 3.28 shows the iso-ARF lines from a simulation with $C_1 = 0.1$. The theoretical log-log slope for large L/D ($\gamma_1 = 0.532$), is very closely matched by the simulation results; see Figure 3.29.

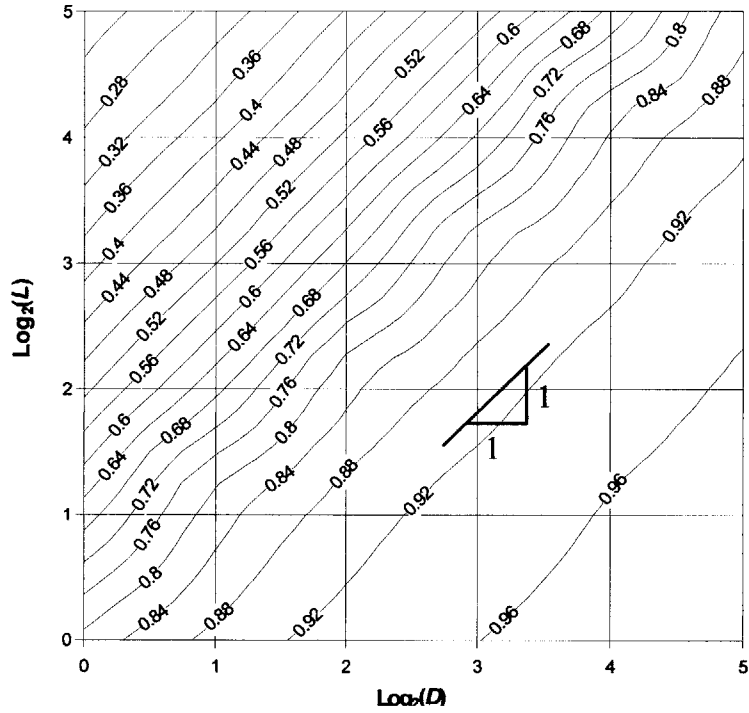


Figure 3.28: ARF scaling behaviour with L and D for the exact multifractal case. The model used is a 3D binary LN discrete cascade with co-dimension coefficient $C_1 = 0.1$.

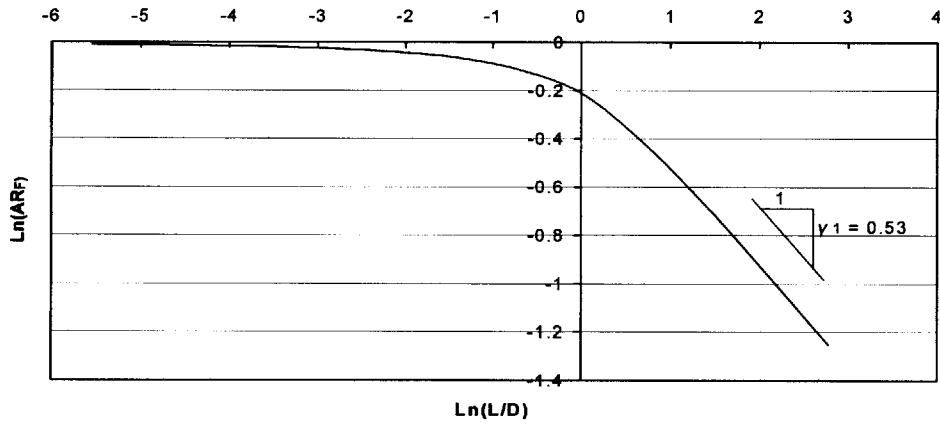


Figure 3.29: ARF scaling behavior with the ratio L/D for the exact multifractal case. The model used is a 3D binary LN discrete cascade with co-dimension coefficient $C_1 = 0.1$ and associated $\gamma_1 = 0.532$.

3.3.1.2 Beta-lognormal cascade

The generator of the cascade, B , has a non zero probability mass at $B = 0$ and $[B|B > 0]$ has lognormal distribution,

$$\ln(B) \sim N(-C_1 \ln(2), 2C_1 \ln(2)) \quad (3.23)$$

where $N(\mu, \sigma^2)$ is the normal distribution with mean value μ and variance σ^2 and C_1 is the co-dimension coefficient. The relationship between C_0 and the probability $P_0 = P[B = 0]$ is,

$$C_0 = -\log_2(1-P_0) \quad (3.24)$$

The procedure followed for the numerical simulations is identical to the one described in Section 3.3.1.1. The simulation region has spatial dimension $2^6 \times 2^6$ tiles and temporal dimension 2^9 tiles, and the results were averaged over 10 independent simulations. Figure 3.30 shows the ARF for $C_1=0.1$ and $P_0 = 0.25$.

Comparing Figure 3.30 with Figure 3.28 for a LN cascade with $C_1=0.1$, one observes that in both cases the contour lines have unit slope. However, the ARF values in Figure 3.28 are smaller and this difference becomes pronounced for both high and low L/D ratios. This can be explained as follows.

First, the overall co-dimension coefficient of the beta cascade model, $C_t = C_0 + C_1 = 0.52$, is much higher than that of the LN cascade with $C_t = C_1 = 0.1$. Thus, for the beta-LN cascade in Figure 3.28 γ_1 is much higher than for the LN cascade. This increase of γ_1 corresponds to smaller ARFs for high L/D ratios.

Second, averaged values in either space or time appear to be smaller for a beta-LN cascade than for a LN cascade with the same C_t . This is so because averaging in a beta-LN cascade accounts also for zero valued tiles. At the same time, the maximum value of an averaged quantity in a beta-LN cascade decreases as the averaging region increases, but this decrease becomes slower for larger regions. This is so because when averaging is small, the averaged field remains heterogeneous (i.e. zero valued tiles separately exist) and close to the non-averaged one. Thus, maximizing over this field is equivalent to maximizing over an equivalent LN field with co-dimension coefficient C_1 approximately equal to the one of the beta-LN field. As the averaging region increases the co-dimension coefficient of the equivalent LN field decreases and tends to a constant value, which is smaller than the one of the co-dimension coefficient of the beta-LN field. Since the ARF is the ratio of the maximum spatially averaged rainfall intensity for a certain time period D to the maximum point rainfall intensity for the same period D , one can conclude that the ARF values of a beta-LN cascade are smaller than these of a LN cascade with the same C_t , and that the spacing of the contour lines of a beta-LN cascade is larger than that of a LN cascade. These two statements hold for both high and low L/D ratios.

Third, the ARF contour lines for a beta-lognormal cascade should have unit slope as happens in the log-normal case. This is so because the generator of the cascade is scale and “state” invariant, and thus the cascade model remains multifractal.

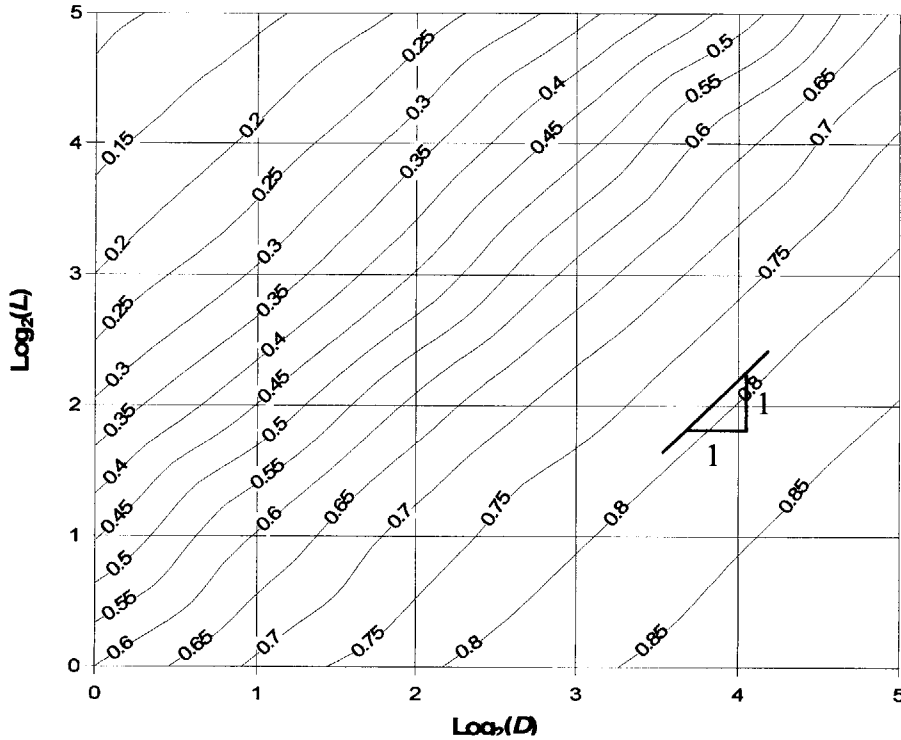


Figure 3.30: ARF scaling behaviour with L and D for a beta LN cascade with $C_1=0.1$ and $P_0 = 0.25$.

3.3.2 Validation of advection effects

Next we investigate numerically the effects of advection on the ARF.

For efficiency of the calculations this is done for the case of spatial averaging on a segment of length L (see Section 3.2.2) and advection velocity vector \mathbf{v}_{ad} parallel to the segment (i.e. $\varphi = 0$ and $\mathbf{v}_{ad} = [0, v_{ad}]^T$). The numerical model used is a 2D binary LN cascade in a $2^{10} \times 2^{10}$ Lagrangian space-time region; see Figure 3.31.

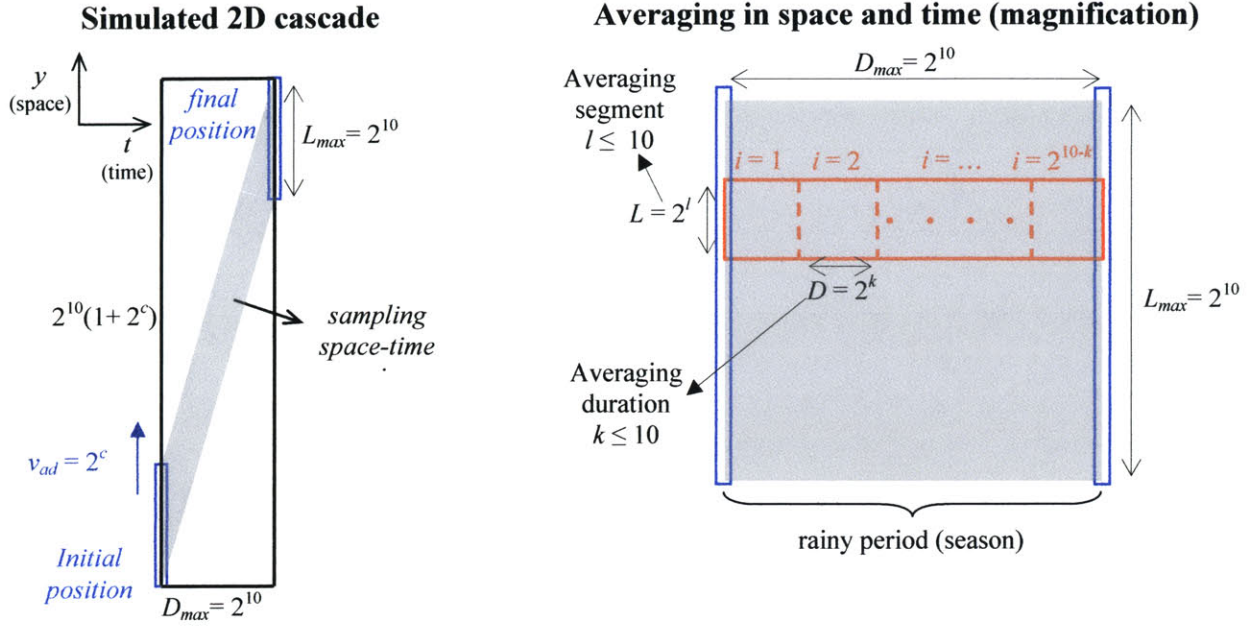


Figure 3.31: Simulation procedure of an advective field using a binary 2D cascade.

The size of the needed simulation region in a Lagrangian frame depends on both the maximum linear dimension L_{max} of the sampling segment and the advection velocity v_{ad} .

In analogy with the 3D cascade in Section 3.3.1, the dressed measures $I_{d,2}(y, t)$ and $I_{d,1}(y, t)$ can be obtained using,

$$\begin{cases} I_{d,2}(y, t) =_d Z_{2D} I_b(y, t) \\ I_{d,1}(y, t) =_d Z_{1D} I_b(y, t) \end{cases} \quad (3.25)$$

where Z_{2D} and Z_{1D} are the dressing factors of a 2D and 1D binary cascade, respectively, having identical generators.

Similar to the 3D case without advection (Section 3.3.1), for each simulated 2D cascade (see Figure 3.31) and for a given advection velocity v_{ad} one can estimate the ARFs for different values of L and D using,

$$ARF(L, D) = \frac{IDAF(L, D)}{IDF(D)} = \frac{E \left[\max_i \left(\int_L \int_{D_i} I_{d,2}(x, y, t) dt dx dy \right) \right]}{E \left[\max_i \left(\int_{D_i} I_{d,1}(x, y, t) dt \right) \right]}, \text{ for } L \leq L_{max}, D_i \leq D_{max} \quad (3.26)$$

Equation (3.26) is a simplified version of equation (3.22) for a 2D cascade. The ARFs estimated have return period $T = 1$ season or 1 year.

To reduce variability among different realizations we averaged the ARF results over 20 independent simulations. The final estimates are shown in Figure 3.32 for no advection ($v_{ad} = 0$), $v_{ad} = 4$ space units per time unit, and $v_{ad} = 8$ space units per time unit.

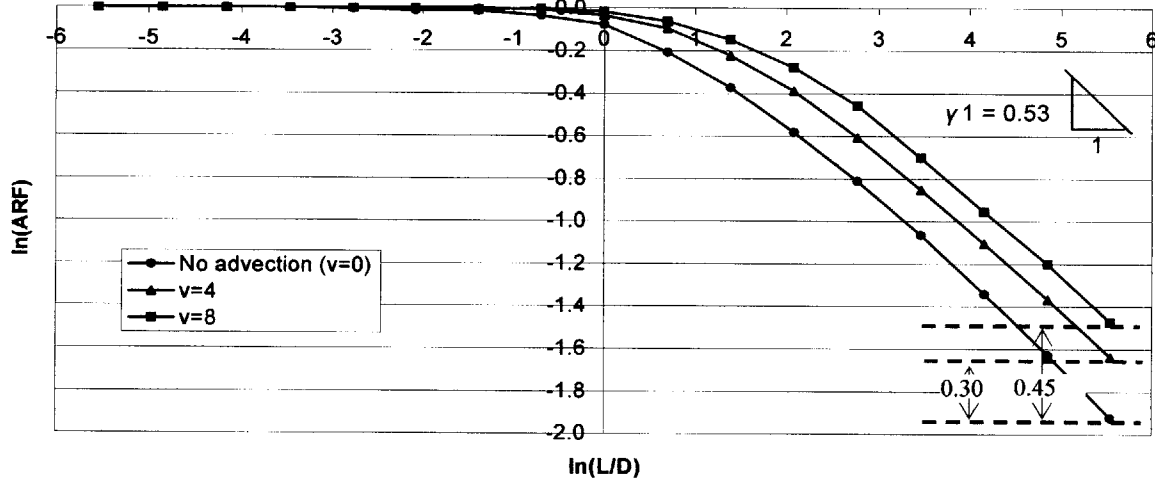


Figure 3.32: ARF scaling behavior with the ratio L/D for different values of v_{ad} . The model used is a 2D binary LN discrete cascade with co-dimension coefficient $C_1 = 0.1$ and $\gamma_1 = 0.532$.

One can use the numerical results in Figure 3.32 to validate the theoretical prefactor changes shown in Table 3.2 (i.e. very elongated basins). In our simulations $C_1 = 0.1$ with associated $\gamma_1 = 0.532$ and $q_1 = 3.162$. Also, $u_{ad,x} = 0$. Using the relationship of Table 3.2 for $u_{res} \gg 1$, T finite and $L \rightarrow 0$, one obtains

$$ARF(L, D, T, u_{ad}) \propto (1 + u_{ad}^2)^{0.108} \left(\frac{L}{D}\right)^{-0.532} \quad (3.27)$$

Thus, the $u_{ad} = 4$ and the $u_{ad} = 8$ curves in Figure 3.32 should be shifted by 0.30 and 0.45, respectively, relative to the $u_{ad} = 0$ curve. These theoretical results are in agreement with those obtained numerically.

3.4 Velocity parameters

Here we discuss the range of velocities v_{res} , v_e and v_{ad} and related velocity parameters $u_{res} = v_{res}/v_e$ and $u_{ad} = v_{ad}/v_e$. For the v_{res} and u_{res} , we focus on problems of flood estimation; hence L is the linear size of a basin and D its characteristic response time.

3.4.1 Response velocity v_{res}

Estimation of the “response velocity” of a drainage basin requires the estimation of both the linear dimension L and the response time D . While L may be approximated as the square root of the drainage area, the estimation of D is not a trivial issue. Many studies have focused on the definition and estimation of a characteristic time scale for the hydrologic response of a basin.

There are many definitions of response time for a basin and different methods of estimation. For example, Tessier *et al.* (1996) suggest a characteristic response time estimated through the spectral analysis of runoff hydrographs, while Morin *et al.* (2001) estimate the characteristic time through cross-analysis of rainfall radar and flood runoff data.

Here we focus on one of the most commonly used definitions in theoretical and practical hydrology, the concentration time t_c , which is defined as the time needed for a water particle falling on the most remote part of the basin to reach the basin outlet (Singh, 1992). t_c cannot be easily measured and in practice is approximated using empirical formulas that include the length of the main stream L_s , the average slope of the basin S or maximum relief H , and possibly other parameters. Table 3.4 summarizes a number of such empirical formulas.

Thus, one can approximate D as the characteristic time scale expressed by t_c and then estimate the response velocity $v_{res} = L/D$ of the basin. Next we obtain some rough limits of v_{res} .

First we find a relation between the average slope S and linear size L of a basin. According to Veneziano and Niemann (2000) the slope s of a basin scales proportionally to $A^{-0.4}$, where A is the area of the basin. Approximating L as the square root of A we write

$$s(L) = c L^{-0.8} \quad (3.28)$$

where c is a constant. Using equation (3.28) and Figure 11 (moment plots of the slope-area relation for Buck and Racoon Creeks) of Veneziano and Niemann (2000), one can estimate

$$\begin{cases} c = 0.17 & , \text{ for highly sloped basins} \\ c = 0.026 & , \text{ for low sloped basins} \end{cases} \quad (3.29)$$

The average slope S of the basin can be approximated as,

$$S = \int_{L_0}^L s(x) dx / (L - L_0) = 5c \frac{L^{0.2} - L_0^{0.2}}{L - L_0}, \text{ for } L > L_0 \quad (3.30)$$

where L_0 is a linear size of reference. For the rest of the analysis we set $L_0 = 0.25\text{Km}$.

Table 3.4: Summary of concentration time empirical formulas.

Method and date	Formula for t_c (min)	Remarks
Kirpich (1940)	$t_c = 3.98 L_s^{0.77} S^{-0.385}$ L_s = length of the main channel [Km]. S = the average slope of the main channel [m/m].	Developed from SCS data for seven rural basins in Tennessee with well defined channel and steep slopes (3% to 10%); for overland flow on concrete or asphalt multiply t_c by 0.4; for concrete channels multiply by 0.2; no adjustments for overland flow on bare soil or flow in roadside ditches.
USBR Design of Small Dams (1973)	$t_c = 60(0.871 L_s^3 H^{-1})^{0.385}$ L_s = length of the longest water-course [Km]. H = elevation difference between divide and outlet [m].	Essentially the Kirpich formula; developed from small mountainous basins in California (U.S. Bureau of Reclamation, 1973, p. 67-71).
Garti <i>et al.</i> (1948)	$t_c = 5.4 L_s^{0.75} S^{-0.375}$ L_s = length of the main channel [Km]. S = the average slope of the main channel [m/m].	Used by the Soil Conservation Division in Israeli Ministry of Agriculture and Rural Development.
Izzard (1946)	$t_c = \frac{5133(2.76 \cdot 10^{-5} i + c) L_s^{0.33}}{S^{0.333} i^{0.667}}$ L_s = length of flow path [Km]. i = rainfall intensity [mm/hour]. c = retardance coefficient. S = the slope of flow path [m/m].	Developed in laboratory experiments by Bureau of Public roads for overland flow on roadway and turf surfaces; values of the retardance coefficient range from 0.007 for very smooth pavement to 0.012 for concrete pavement to 0.06 for dense turf; product i times L_s should be ≤ 4 ; method requires iterations.
Federal Aviation Administration (1970)	$t_c = 103.1(1.1 - C) L_s^{0.5} S^{-0.333}$ C = rational method runoff coefficient. L_s = length of overland flow [Km]. S = the average slope of the main channel [%].	Developed from airfield drainage data assembled by the Corps of engineers; method is intended for use on airfield drainage problems, but has been used frequently for overland flow in urban basins; C ranges from 0.4 for natural low slope areas to 0.8 for urban highly developed areas.
Kinematic Wave Formulas Morgali and Linsley (1965) Aron and Erborge (1973)	$t_c = 347 L_s^{0.6} n^{0.6} i^{-0.4} S^{-0.3}$ L_s = length of overland flow [Km]. i = rainfall intensity [mm/hour]. n = Manning roughness coefficient. S = average overland slope [m/m].	Overland flow equation developed from kinematic wave analysis of surface runoff from developed surfaces; n of Manning ranges from 0.012 to 0.15 (for a photographic method for estimating n see Chow (1959) pp. 115-123); method requires iterations.
SCS Lag Equation (1972)	$t_c = 0.571[(1000/CN) - 9]^{0.7} L_s^{0.8} S^{-0.5}$ L_s = longest flow path [Km]. CN = SCS runoff curve number. S = average overland slope [%].	Equation developed by SCS from agricultural watershed data; it has been adapted to small urban basins under 2000 acres; found generally good where area is completely paved; for mixed areas it tends to overestimate; adjustment factors are applied to correct for channel improvement and impervious area; the estimation of CN is done from curves provided by SCS (1972).

Letting $L_s = 1.3L$ and combining equations (3.29) and (3.30) with the empirical formulas presented in Table 3.4, we find that for typical values of the parameters C , CN , c and n the response velocity v_{res} ranges from 3Km/hour to 7.5 Km/hour. The values of v_{res} depend on the method used for the estimation of t_c . Moreover, v_{res} does not vary much with L and depends mostly on the average slope S . High values of v_{res} correspond to developed basins and high slopes. Table 3.5 summarizes some results from the analysis performed on the estimation of v_{res} .

Table 3.5: Estimation of the v_{res} .

High slopes										
Basin Area (Km ²)	L (Km)	Ls (Km)	S	ΔH (m)	D [hours] Kirpich	D [hours] USBR	D [hours] Garti <i>et al.</i>	Response velocity [Km/h]		
								Kirpich	USBR	Garti <i>et al.</i>
1	1.00	1.30	0.2744	356.76	0.13	0.13	0.18	7.5	7.5	5.62
10	3.16	4.11	0.1462	601.21	0.41	0.41	0.53	7.7	7.7	5.92
50	7.07	9.19	0.0898	825.79	0.93	0.93	1.17	7.6	7.6	6.03
100	10.00	13.00	0.0721	937.31	1.32	1.32	1.65	7.6	7.6	6.05
500	22.36	29.07	0.0424	1233.48	3.00	3.00	3.68	7.5	7.5	6.07
1000	31.62	41.11	0.0335	1378.23	4.29	4.29	5.22	7.4	7.4	6.06
5000	70.71	91.92	0.0191	1758.54	9.89	9.89	11.78	7.2	7.1	6.00
10000	100.00	130.00	0.0149	1943.06	14.20	14.21	16.76	7.0	7.0	5.97

Low slopes										
Basin Area (Km ²)	L (Km)	Ls (Km)	S	ΔH (m)	D [hours] Kirpich	D [hours] USBR	D [hours] Garti <i>et al.</i>	Response velocity [Km/h]		
								Kirpich	USBR	Garti <i>et al.</i>
1	1.00	1.30	0.0420	54.56	0.28	0.28	0.36	3.6	3.6	2.78
10	3.16	4.11	0.0224	91.95	0.85	0.85	1.08	3.7	3.7	2.93
50	7.07	9.19	0.0137	126.30	1.91	1.91	2.37	3.7	3.7	2.98
100	10.00	13.00	0.0110	143.35	2.71	2.71	3.34	3.7	3.7	2.99
500	22.36	29.07	0.0065	188.65	6.18	6.18	7.45	3.6	3.6	3.00
1000	31.62	41.11	0.0051	210.79	8.83	8.84	10.56	3.6	3.6	3.00
5000	70.71	91.92	0.0029	268.95	20.37	20.38	23.82	3.5	3.5	2.97
10000	100.00	130.00	0.0023	297.17	29.26	29.27	33.89	3.4	3.4	2.95

3.4.2 Evolution velocity v_e and advection velocity v_{ad}

The advection velocity v_{ad} is a physical quantity directly estimated from data. In particular, estimation of v_{ad} requires a procedure known as “rainstorm tracking”. This procedure aims at deriving the advection velocity vector of a rainstorm using rain-gauge, radar or satellite data (Zawadzki, 1973; Takeuchi, 1985; Takeuchi and Guardado, 1990; Upton, 2002). For example, Deidda (2000) suggests a technique for rainstorm tracking using the spatial and temporal autocorrelation functions of a rainfall field. Assuming stationarity of the rainfall process in space and time, Deidda estimates the spatial $\rho_x(|dx|)$, $\rho_y(|dy|)$ and temporal $\rho_t(|dt|)$ autocorrelation functions of the storm. Then the values of three arbitrary constants dx_0 , dy_0 and dt_0 are selected in order for $\rho_x(|dx/dx_0|)$ and $\rho_y(|dy/dy_0|)$ to match $\rho_t(|dt/dt_0|)$. Provided that the advection velocity of the rainfall field is constant for all scales, one can estimate the advection velocity vector as,

$$\mathbf{v}_{ad} = [v_{ad,x}, v_{ad,y}]^T = [dx_0/dt_0, dy_0/dt_0]^T \quad (3.31)$$

Estimation of the evolution velocity v_e requires the estimation of the characteristic linear size L_e and lifetime D_e of rainfall generating structures. Many studies have focused on the estimation of L_e and D_e . For example, Merzin *et al.* (2003) distinguish moisture transport contributing features with respect to their linear size: Atmospheric turbulence when $L_e < 1$ Km, convective cells when $1 \text{ Km} \leq L_e < 3 \text{ Km}$, mesoscale formations (convective bodies) when $3 \text{ Km} \leq L_e \leq 10 \text{ Km}$ and large scale formations when $L_e > 10 \text{ Km}$. Also, Mecklenburg *et al.* (2000) find that

single hail cells have mean linear size $L_e \approx 7$ Km and lifetime $D_e \approx 85$ min, which correspond to $v_e \approx 5$ Km/hour.

A categorization of precipitation areas is given by Austin and Houze (1972), who studied the precipitation patterns of nine storms in New England covering a wide range of seasonal and synoptic conditions. All patterns were found to be composed by sub-synoptic scale precipitation areas with clearly definable characteristics. These areas can be grouped into 4 categories presented in Table 3.6.

Table 3.6: Categories of precipitation areas and their characteristics.

Type	Area covered	Linear size L_e	Lifetime D_e	Evolution velocity v_e [km/hour]
Small areas	10 Km ²	3 Km	< 30 min	~ 10 Km h ⁻¹
Small mesoscale areas	100 Km ² ÷ 400 Km ²	10 Km ÷ 20 Km	1 hour	10 Km h ⁻¹ ÷ 20 Km h ⁻¹
Large mesoscale areas	1 000 Km ² ÷ 10 000 Km ²	30 Km ÷ 100 Km	Several hours	10 Km h ⁻¹ ÷ 20 Km h ⁻¹
Synoptic scale areas	> 10 000 Km ²	> 100 Km	≥ 1 day	~ 5 Km h ⁻¹ ÷ 10 Km h ⁻¹

The results of Austin and Houze (1972) are nearly identical with the spatial and temporal scale subdivision of atmospheric features proposed by Orlanski (1975).

Chaudhry *et al.* (1996) obtained statistics on tropical convective storms. Multiple convective cell events have mean linear size $L_e \approx 16$ Km and lifetime $D_e \approx 50$ min, which correspond to $v_e \approx 19$ Km/hour. The latter value is included in the range given by Austin and Houze (1972). Moreover, the advection velocity of the cells was found to lie mostly in the range between 20 - 50 Km/hour.

Based on analyses of the GATE data set (Tropical North Atlantic Global Atmospheric Research Program (GARP) Atlantic Tropical Experiment (GATE)), Martin and Schreiner (1981) present the Probability Density Functions (PDFs) of the lifetime of cloud clusters with linear dimension ranging between 100 and 1000 Km. One can estimate that the corresponding evolution velocity takes values in the range between 6 to 12 Km/h. The latter is in agreement with the results of Austin and Houze (1972), and Orlanski (1975). Martin and Schreiner (1981) find the advection velocity of the cloud clusters to be almost 30 Km/h. They argue that this value of v_{ad} is almost 10 km/h higher than the one expected, and this magnification can be ascribed to local conditions.

Based on correlation analysis results, Kawamura *et al.* (1996) argue that the speed at which a rainfall cell is advected is not dependent on the cell development stage. Thus, one can manage

advection and evolution of the features independently. Also, Kawamura *et al.* (1996) find that the advection velocity of rainfall cells ranges from zero to 38.5 Km/hour with mean value 20.5 Km/hour. Same range of v_{ad} values has been obtained by Upton (2002).

Generally, the evolution velocity v_e ranges from 5 to 20 Km/hour as presented in Table 3.6. The advection velocity v_{ad} , ranges from zero to 50 Km/hour with commonly met values of 35 - 50 Km/hour for small features and 20 - 40 Km/hour for large features. However, these values can only be considered as rough approximations and might be largely altered by local conditions (for an example see: Martin and Schreiner, 1981).

3.5 Comments

In the previous sections we analyzed the behavior of rainfall extremes when space-time multifractal rainfall is observed over an area.

First we considered the case of zero advection velocity (i.e. $v_{ad} = 0$) and we obtained the scaling properties of the IDAF curves and ARFs with L , D and T .

Next we examined the effects of $v_{ad} \neq 0$ on the IDF, IDAF curves and ARFs and we found that their scaling properties are affected by advection. For highly elongated basins both the direction and magnitude of advection affect the results, while for relatively symmetric basins only the magnitude of advection is important.

However when over land flow is studied, the storm direction and pattern become, also, important factors determining the shape of the runoff hydrograph. Lima and Singh (2002) find that the peak discharges and hydrograph shapes depend strongly on the storm pattern, the characteristics of the catchment area and the direction and speed of storms. Storms moving upstream (i.e. opposite to the flow direction) are normally characterized by hydrographs with early rise, low peak discharge, not steep rising limb and long base time. Also, the sensitivity of the hydrographs to rainfall patterns decreases as the advection velocity of the storm increases. In particular, rainfall intensity patterns become an important parameter when advection velocity is low and less than about 10 Km/hour.

4. Imperfect scaling of rainfall, sparse sampling and their effects on the ARF

Although rainfall is thought to inherit its scaling properties from atmospheric turbulence (see for example Frish, 1985; Frish and Parisi, 1985; Meneveau and Sreenevasan, 1987), the exact transfer mechanisms of multifractality from turbulence to rainfall are not known. Complications arise when one considers the atmospheric mechanisms associated with water vapor transfer and rainfall generation. For example, unconditional stability of the prestorm environment results to thermal stratification of the atmosphere with layers that have different temperature and moisture content. In those layers the generated eddies remain isolated, with scaling properties that depend on the thermal characteristics of the layer, and maximum linear size that does not exceed the height of the layer. Therefore, even if perfect multifractality of turbulence holds in any of those layers, their integrated result, observed as ground-level rainfall, may violate perfect scale invariance.

Many studies (e.g. Fraedrich and Larnder, 1993; Olsson *et al.*, 1993; Olsson, 1995) show violations of scaling in temporal rainfall records for aggregation periods larger than about 2 weeks or smaller than a few minutes. A possible break of scaling for aggregation periods 2-3 hours has also been detected. However, these observations are associated with some uncertainties (Olsson, 1995).

In the case of perfect isotropic multifractality, rainfall intensity $I(x, y, t)$ is the product of independent and identically distributed (id) fluctuations $W_j(x, y, t)$ at different log resolutions $j = 1, 2, \dots$. The fluctuations satisfy the scaling relation,

$$W_j(x, y, t) =_d W_j(r_0^j x, r_0^j y, r_0^j t) \quad (4.1)$$

where $r_0 > 1$ is a contraction factor, $W(x, y, t)$ is a non-negative random field with unit mean value, and $=_d$ denotes equality in distribution. The main features of this construction is that the fluctuations at different log-scales combine in a multiplicative way (multiplicative property) and are statistically identical after scaling of the support (id property).

Although the multiplicative property is generally supported by data (Veneziano *et al.*, 1996; Carsteanu and Foufoula-Georgiou, 1996; Menabde *et al.*, 1997), deviations from the id property have been found in the form of dependences of W_j on the scale j (Perica and Foufoula-Georgiou,

1996b; Veneziano *et al.*, 1996; Menabde *et al.*, 1997; Menabde and Sivapalan, 2000) and on covariates such as large-scale rainfall intensity (Over and Gupta, 1996; Veneziano *et al.*, 2003).

Section 4.1 reviews observed deviations from equation (4.1) and models that have been proposed to capture such deviations. The models reviewed include:

- (1) The bounded cascade model proposed by Menabde and Sivapalan (2000) for temporal rainfall downscaling. This model is based on the technique of Breakdown Coefficients (BDC) and accounts for changes with scale j of the marginal distribution of W_j .
- (2) A model developed by Perica and Foufoula-Georgiou (1996b) for spatial rainfall downscaling using wavelet decomposition. This model was initially developed for simulating rainfall variability at scales unresolved by numerical mesoscale atmospheric models. The model assumes that the standardized rainfall fluctuations have normal distribution and simple scaling in space. The scaling parameters of the standardized rainfall fluctuations depend on the spatial scale, and are related to the Convective Available Potential Energy (CAPE) of the prestorm environment.
- (3) Two multiplicative cascade models by Over and Gupta (1996) and Veneziano *et al.* (2003) for rainfall generation with beta-lognormal and beta-logstable generators. The model of Over and Gupta (1996) is for spatial rainfall. It considers the beta-lognormal generators W_j to be independent and identically distributed, but allows the distribution to depend on the average rainfall intensity over the radar frame. The model of Veneziano *et al.* (2003) assumes that W_j has beta-logstable distribution with parameters that depend on the scale j and the bare rainfall intensity $I_{b,j-1} = I_0 \prod_{k < j} W_k$ in the parent cascade tile $j-1$.

- (4) The 3-parameter universal multifractal model of Lovejoy and Schertzer (1995). This model is based on properties of turbulence and uses three parameters: the co-dimension coefficient C_1 , the Levy index of the generator α , and the order H of fractional integration.

Section 4.2 discusses how estimates of spatially averaged rainfall from raingauge networks are affected by the network density. This is an important problem because the ARF estimation is typically based on raingauge records.

Section 4.3 investigates numerically the effects that deviations from multifractality and sparse spatial sampling have on the estimated ARFs. First we investigate how the ARF behaves for a bounded cascade representation of rainfall in space and time. Then we present the effects

of sparse spatial sampling on the estimated ARFs for different densities of the raingauge network.

4.1 Observed deviations of rainfall from multifractality

4.1.1 Bounded cascade models for temporal rainfall

First we review the definition of the Breakdown Coefficients (BDC), which form the basis of the bounded cascade model of temporal rainfall proposed by Menabde *et al.* (1997b), Harris *et al.* (1998) and Menabde and Sivapalan (2000).

Let $I_D(t)$ be the total accumulated rainfall in the time interval $[t, t + D]$. The BDC is defined as the ratio of the total accumulated rainfall in a time period D to the total accumulated rainfall in a longer time period rD , i.e.

$$R(t, D, r) =_d \frac{I_D(t)}{I_{rD}(rt)}, \quad r > 1 \quad (4.2)$$

Generally, the BDC is a random variable that depends on t , D and r . If the process $I_D(t)$ is stationary multifractal then the statistical properties of BDC depend only on r , i.e.

$$R(t, D, r) =_d R(r), \quad r > 1 \quad (4.3)$$

However, analyses of many rainfall time series (Menabde *et al.*, 1997b; Harris *et al.*, 1998) suggest that R depends also on the scale of aggregation D . Dependence on D is an indication of deviation from multifractality.

The bounded cascade model of Menabde and Sivapalan (2000) includes dependence of the BDC on r and D .

Using a dyadic cascade representation, one can directly estimate the empirical Probability Density Functions (PDFs) of the BDCs of a rainfall time series for different standardized accumulation periods,

$$D_n = 2^n (D_0/d), \quad n = 0, 1, \dots \quad (4.4)$$

where D_0 is the outer limit of the cascade (i.e. maximum scale of aggregation), d is the minimum accumulation period (i.e. scale of maximum resolution), and n is the cascade level. The empirically derived PDFs can then be smoothed by fitting an analytic PDF with parameters that depend on D_n .

For example, Menabde and Sivapalan (2000) analyzed a continuous rainfall record from Melbourne (Menabde *et al.*, 1999) with $d = 6$ min. The value of D_0 , was set to 192 min (i.e. $\max(n) = 5$). They found that the empirical PDFs of the BDCs are well approximated by the beta density,

$$p_X(x) = \frac{1}{B(a)} x^{a-1} (1-x)^{a-1} \quad (4.5)$$

where $B(a)$ is the beta function and the parameter a scales with D_n as,

$$a(D_n) = a_0 D_n^{-b} \quad (4.6)$$

where $a_0 = 12.27$ and $b = 0.47$. This corresponds to a bounded cascade representation of temporal rainfall. This is so because the standard deviation of the BDCs decreases as the temporal resolution or equivalently the level n increases.

Thus, a micro-canonical multiplicative cascade (discussed next) with random generator W_n described by equations (4.4)-(4.6) preserves the dependence of the BDCs on D observed in the data.

In a micro-canonical cascade for rainfall totals, the multiplicative factors $w_{n,0}(j)$ and $w_{n,1}(j)$ in Figure 4.1 satisfy,

$$w_{n,0}(j) + w_{n,1}(j) = 1, \quad n = 0, 1, \dots; \quad j = 1, \dots, 2^n \quad (4.7)$$

and no dressing is required.

One can use equations (4.5) and (4.6) to obtain the standard deviation $\sigma_w(n)$ of the generator w_n at level n . Then one can estimate the standard deviation $\sigma_q(n)$ of the generator q_n of a micro-canonical cascade model for rainfall intensities by using the relationship,

$$\sigma_q(n) = 2 \sigma_w(n) \quad (4.8)$$

This is a direct consequence of the fact that $q_n = 2 w_n$.

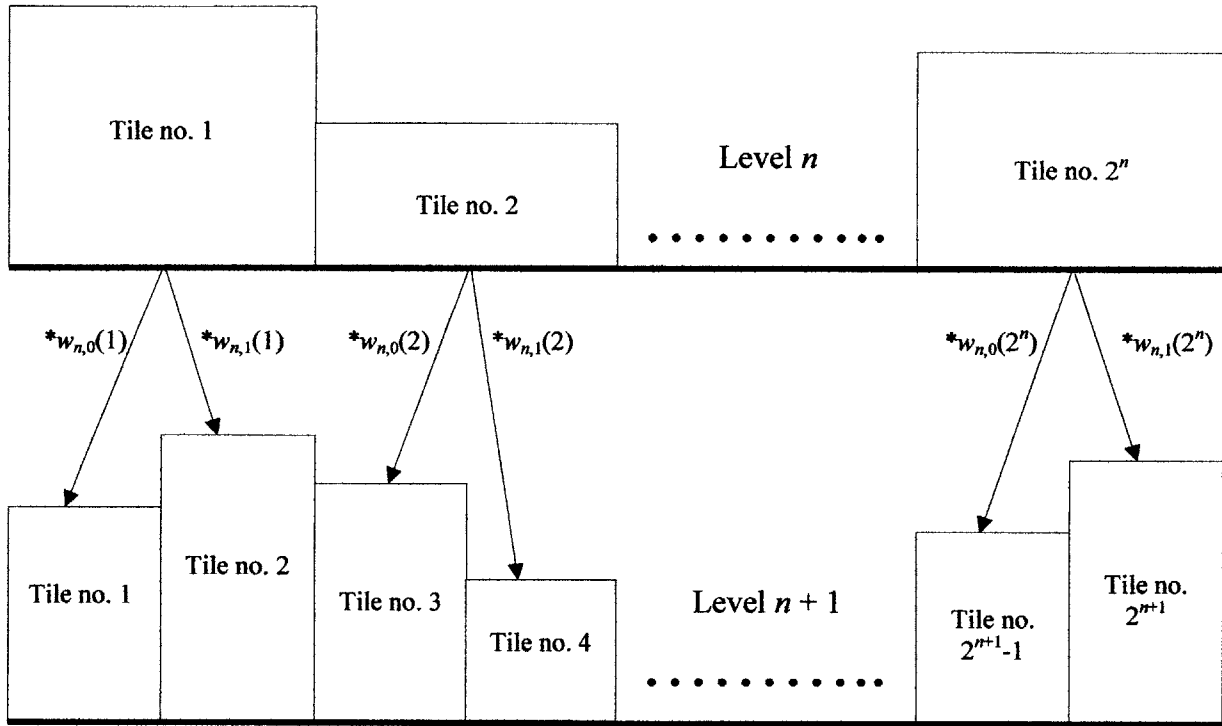


Figure 4.1: Generation of a micro-canonical cascade for rainfall totals.

For the data set from Melbourne (Menabde *et al.*, 1999) one obtains the values in Table 4.1. These values are shown graphically in Figure 4.2.

Table 4.1: Standard deviation $\sigma_q(n)$ of the generator q_n of an equivalent micro-canonical cascade for rainfall intensities. $a_0 = 12.27$, $b = 0.47$, $d = 6$ min, and $D_0 = 192$ min.

Level (n)	Duration (min)	D_n	$a(D_n)$	$\sigma_q(n)$
0	192	32	2.407	0.415
1	96	16	3.334	0.361
2	48	8	4.617	0.313
3	24	4	6.396	0.269
4	12	2	8.859	0.231
5	6	1	-	-

The above bounded-cascade model was used by Menabde and Sivapalan (2000) to simulate rainfall time series with 6 min resolution. The statistics of the synthetic time series were compared to those of the data set from Melbourne. The model showed good behaviour and reproduced well the observed extremes.

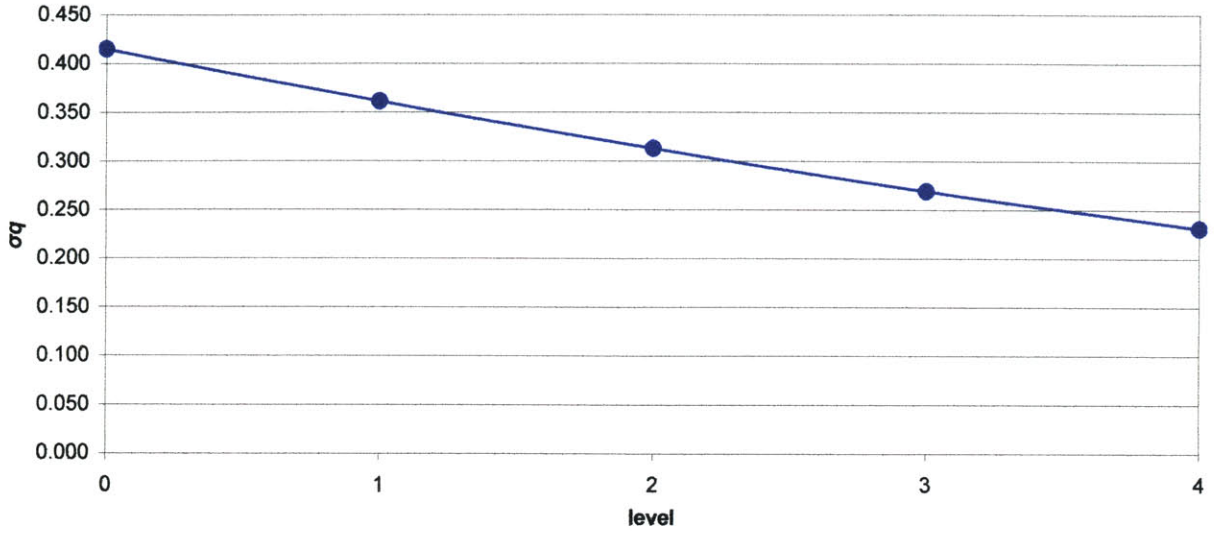


Figure 4.2: Standard deviation $\sigma_q(n)$ of the generator q_n of an equivalent micro-canonical cascade for rainfall intensities. $a_0 = 12.27$, $b = 0.47$, $d = 6$ min, and $D_0 = 192$ min.

4.1.2 Spatial rainfall model of Perica and Foufoula-Georgiou (1996b)

Perica and Foufoula-Georgiou (1996b) proposed a model for spatial down scaling of rainfall based on wavelets.

The model aims at simulating rainfall variability at scales unresolved by numerical mesoscale atmospheric models. The precipitation output of these models is the average rainfall intensity over a grid with typical cell dimensions 30×30 Km to 60×60 Km. Thus, spatial rainfall downscaling is essential if rainfall intensity is needed at sub-grid scales (i.e. scales smaller than a grid cell).

Let $I_m(i, j)$ be the average rainfall intensity at relative scale 2^m ($m = 0, 1, 2, 3$) around location (i, j) . Perica and Foufoula-Georgiou (1996b) take $m = 0$ to correspond to the smallest scale of interest (4×4 Km) and $m = 3$ to the largest scale (64×64 Km).

For the discrete field $I_m(i, j)$, Perica and Foufoula-Georgiou (1996b) use a 2D Haar wavelet representation. Specifically, $I_m(i, j)$ can be expressed as the sum of the average $I_{m+1}(n, k)$ at the next higher scale and three fluctuation fields $I'_{m+1,l}(n, k)$ ($l = 1, 2, 3$),

$$I_{m+1}(n, k) = \frac{1}{4} [I_m(i, j) + I_m(i, j+1) + I_m(i+1, j) + I_m(i+1, j+1)] \quad (4.9)$$

$$I'_{m+1,1}(n, k) = \frac{1}{4} \{ [I_m(i, j) + I_m(i, j+1)] - [I_m(i+1, j) + I_m(i+1, j+1)] \} \quad (4.10)$$

$$I'_{m+1,2}(n, k) = \frac{1}{4} \{ [I_m(i, j) + I_m(i+1, j)] - [I_m(i, j+1) + I_m(i+1, j+1)] \} \quad (4.11)$$

$$I'_{m+1,3}(n, k) = \frac{1}{4} \{ [I_m(i, j) - I_m(i+1, j)] - [I_m(i, j+1) - I_m(i+1, j+1)] \} \quad (4.12)$$

The indices (i, j) denote the spatial position at scale m , while the indices (n, k) denote the spatial position at scale $m+1$; see Figure 4.3.

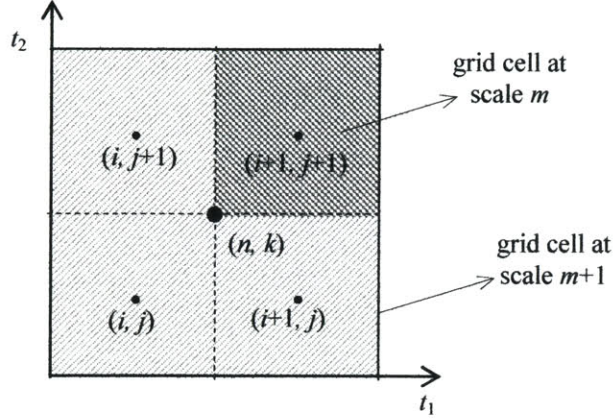


Figure 4.3: Discretization on a two dimensional grid at relative scales m (dashed lines) and $m+1$ (solid lines).

The fluctuation components on the left hand side of equations (4.10), (4.11) and (4.12) may be viewed as discrete representations of the spatial derivatives $\frac{\partial I_m}{\partial t_1}$, $\frac{\partial I_m}{\partial t_2}$ and $\frac{\partial^2 I_m}{\partial t_1 \partial t_2}$ respectively.

Based on the analysis of several storms from the PRE-STORM data set, Perica and Foufoula-Georgiou (1996a) suggest that the rainfall fluctuations standardized by the corresponding scale averages,

$$\zeta_{m,i} = \begin{cases} \frac{I'_{m,i}}{I_{m,i}}, & \text{if } I_{m,i} > 0 \\ 0 & \text{if } I_{m,i} = 0 \end{cases}, \quad i = 1, 2, 3 \quad (4.13)$$

have normal distribution and simple scaling behavior. This behavior is described by the equation,

$$\sigma_{m,i} = 2^{(m-1)H_i} \sigma_{1,i}, \quad i = 1, 2, 3; \quad m \geq 1 \quad (4.14)$$

where $\sigma_{m,i}$ is the standard deviation of $\zeta_{m,i}$, and H_i and $\sigma_{1,i}$ are dimensionless constants.

Perica and Foufoula-Georgiou (1996b) found that directional differences among the parameters H_i and $\sigma_{1,i}$ were insignificant, and thus only two parameters H and σ_1 were required

for all directions i . These parameters are given by empirical formulas that include the Convective Available Potential Energy (CAPE) of the prestorm environment:

$$\begin{cases} H = 0.0516 + 0.9646 (\text{CAPE} \times 10^{-4}) \\ \sigma_1 = 0.539 - 0.8526 (\text{CAPE} \times 10^{-4}) \end{cases} \quad (4.15)$$

where CAPE is in $[\text{m}^2/\text{sec}^2]$. The formulas in equation (4.15) have a regression R value of 0.82 and -0.73 respectively.

Starting from a given spatially averaged rainfall intensity and following the inverse procedure (i.e. from higher to lower m), one can perform spatial rainfall disaggregation.

One can directly relate ξ_m to the generator q_m of a micro-canonical cascade for rainfall intensity (see Appendix A). Therefore, dependence of ξ_m on the spatial scale m indicates deviation from multifractality similar to a bounded cascade model.

Specifically, the standard deviation $\sigma_q(m)$ of the generator q_m of a 1D micro-canonical cascade is given by (for a detailed analysis see Appendix A),

$$\sigma_q(m) = 2^{(m-1)H+0.5} \sigma_1, \quad m \geq 1 \quad (4.16)$$

Table 4.2 and Figure 4.4 show the values of $\sigma_q(m)$ for two values of CAPE: (1) CAPE = $2500 \text{ m}^2/\text{sec}^2$, and (2) CAPE = $2880 \text{ m}^2/\text{sec}^2$.

Table 4.2: Standard deviation $\sigma_q(m)$ of the generator q_m of a 1D micro-canonical cascade for two values of CAPE: (1) CAPE = $2500 \text{ m}^2/\text{sec}^2$, and (2) CAPE = $2880 \text{ m}^2/\text{sec}^2$.

Level	m	Linear scale (Km)	$\sigma_q(m)$ (CAPE=2500)	$\sigma_q(m)$ (CAPE=2880)
0	4	64	0.847	0.823
1	3	32	0.691	0.655
2	2	16	0.564	0.521
3	1	8	0.461	0.415
4	0	4	-	-

Given the uncertainty under which CAPE is estimated and the limited accuracy of equations (4.15), one can conclude that for a value of CAPE $\approx 2500 \text{ m}^2/\text{sec}^2$ the last value of $\sigma_q(m)$ in Table 4.2 is in good agreement with the first value of Table 4.1. If this is so, then the “*evolution velocity*” (see Section 3.4) v_e of the organized rainfall features would be constant and approximately equal to 2.5 Km/h (i.e. $v_e \approx \frac{8 \text{ Km}}{192 \text{ min}} = 2.5 \text{ Km/h}$). This value of v_e is small compared to the value 10-20 Km/h shown in Table 3.6. This is due at least in part to the

different scaling behaviour of the data sets used in the two studies. Specifically, Menabde and Sivapalan (2000) use continuous rainfall records and thus include the effects of dry periods and different precipitation patterns (e.g. convective cells, cloud clusters, stratiform patterns etc.), whereas Perica and Fofoula-Georgiou (1996b) use data from specific storm types with CAPE in the range from 1000 to 2800 m^2/sec^2 .

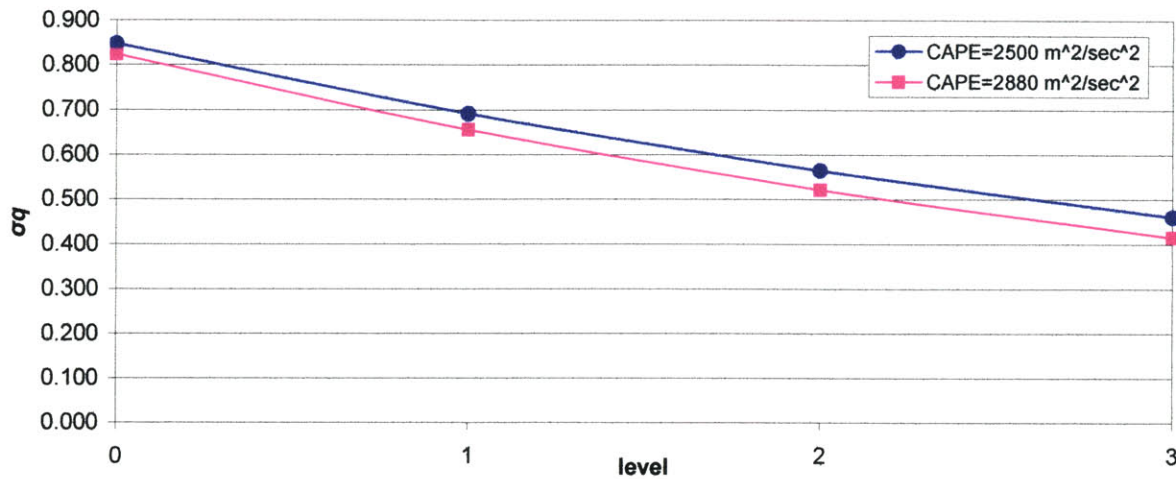


Figure 4.4: Standard deviation $\sigma_q(m)$ of the generator q_m of a 1D micro-canonical cascade for two values of CAPE: (1) CAPE = 2500 m^2/sec^2 , and (2) CAPE = 2880 m^2/sec^2 .

The ability of the model to reproduce the variability of rainfall at small spatial scales was validated by Perica and Fofoula-Georgiou (1996b).

4.1.3 Cascade models with dependence on large scale rainfall intensity

Several studies (Over and Gupta 1994, 1996; Veneziano *et al.*, 1996; Menabde *et al.*, 1997a; Veneziano *et al.*, 2003) have found that the fractal dimension of rain and the amplitude of the multifractal fluctuations depend on the large-scale rain rate, and possibly on scale itself.

In particular, Over and Gupta (1994, 1996) and Veneziano *et al.* (2003) concluded that the fractal dimension of the rain support increases with increasing rain rate. The latter study further observed that the amplitude of the multiplicative fluctuations depends on the observation scale. This is an indication that rainfall fields deviate from an exact multifractal behavior, which requires the generator to be scale and “state” invariant. Notice that dependencies of the generator on scale have also been observed by Menabde and Sivapalan (2000) and Perica and Fofoula-Georgiou (1996b); see Sections 4.1.1 and 4.1.2.

Next we describe in greater detail two specific rainfall models that incorporate dependencies of this type. One is a beta-lognormal model of Over and Gupta (1996) and the other is a beta-logstable model of Veneziano *et al.* (2003). The former accounts only for dependencies of the generator on the average rainfall intensity over the radar frame, and thus it does not deviate from exact multifractality, whereas the latter accounts also for dependencies of the generator on the scale in the form of a bounded cascade model.

Beta-lognormal cascade model of Over and Gupta

Over and Gupta (1996) fitted a spatial beta-lognormal cascade to each frame of the GATE-1 and GATE-2 (GARP Atlantic Tropical Experiment, phases 1 and 2) radar sequences. They then examined how the multifractal parameters depend on the mean rainfall intensity I over the frame.

The generator W of the cascade is assumed to have a non zero probability mass at $W = 0$, while $[W|W > 0]$ is assumed to have lognormal distribution such that $E[W] = 1$.

The bare moment scaling function $K_w(q)$ of this beta-lognormal model is,

$$K_w(q) = C_0 (q - 1) + C_1 (q^2 - q) \quad (4.17)$$

where C_0 and C_1 are parameters. The relationships among C_0 , the probability $P_0 = P[W = 0]$ and the fractal dimension of the rainfall support \tilde{d} are,

$$C_0 = -\log_m(1-P_0) = d - \tilde{d} \quad (4.18)$$

where d is the Euclidean dimension of the observation space (e.g. $d = 1$ for temporal rainfall, $d = 3$ for space-time rainfall) and m is the multiplicity of the cascade. The co-dimension coefficient C_1 is related to the variance σ^2 of $[\log_m W|W > 0]$ as $C_1 = \frac{\sigma^2}{2\ln(m)}$. The parameters C_0 and C_1 control the lacunarity of rainfall (alterations of wet/dry periods) and the intensity of the multiplicative fluctuations, respectively, and can be inferred from data in various ways (e.g. best fitting of the empirical $K_w(q)$ function).

Over and Gupta (1996) find that C_0 increases strongly for decreasing large-scale average rainfall intensity I . By comparison, the dependence of C_1 on I was found to be modest with a maximum of C_1 at intermediate values of I . Similar results have been obtained by Deidda (2000) and Ferraris *et al.* (2003). However, one should be aware that conditioning on I introduces biases. In particular, when I is low, precipitation tends to be sparse with low \tilde{d} and high C_0 .

Another source of bias is the sensitivity threshold of the radar. Below this threshold rainfall intensity is reported as zero and the artificial zeros increase the sparseness of reported rainfall and hence increase the estimates of C_0 for low I .

Beta-logstable cascade model of Veneziano *et al.*

The rainfall model of Veneziano *et al.* (2003) differs from the one by Over and Gupta (1996) in three respects:

First, Over and Gupta (1996) consider the random generators W_j at all levels j to be independent and identically distributed with distribution that depends on the average rainfall intensity over the radar frame. By contrast, Veneziano *et al.* (2003) assume that the generator

from level $j-1$ to j depends on the bare rainfall intensity $I_{b,j-1} = I_0 \prod_{k < j} W_k$ in the parent cascade

tile $j-1$. Notice that $I_{b,j-1}$ is the intensity when the cascade construction is terminated at level $j-1$, while I is a dressed intensity. Second, Veneziano *et al.* (2003) assume that rainfall is approximately multifractal in space and time not just in space. Thus, the cascade tiles are “cubes” in space-time with size depending on the level j . Third, Veneziano *et al.* (2003) allow W_j to depend not only on $I_{b,j-1}$ but also on the level j .

The generator W_j has probability mass P_0 at $W = 0$, which depends on the level j of the cascade and the bare measure $I_{b,j-1}$. Also, $[W_j | W_j > 0]$ is considered to have Levy stable distribution with skewness coefficient $\beta = -1$ and stability index $0 < \alpha \leq 2$ (on Levy stable distributions see for example Samorodnitsky and Taqqu, 1994) that depends on both j and $I_{b,j-1}$. In the beta-logstable case, the bare moment scaling function is (Schertzer and Lovejoy, 1987),

$$K_w(q) = C_0 (q - 1) + \frac{C_1}{\alpha - 1} (q^\alpha - q) \tag{4.19}$$

Given that the distribution of W_j varies with j and $I_{b,j-1}$, the parameters C_0 , C_1 and α vary also with j and $I_{b,j-1}$. One can group the parameters C_0 , C_1 and α into a vector $\theta_w(j, I_{b,j-1}) = [C_0, C_1, \alpha]$.

Strictly speaking,

$$W_j = \frac{I_{b,j}}{I_{b,j-1}} \tag{4.20}$$

However, the bare densities I_b cannot be observed and one must infer the distribution of W_j using observable dressed quantities. Veneziano *et al.* (2003) adjust the parameters $\theta_w(j, I_{b,j-1})$ to match statistics of the partition coefficients,

$$Q_j = \frac{I_{dj}}{I_{dj-1}} \quad (4.21)$$

which are similar ratios involving dressed quantities.

Veneziano *et al.* (2003) estimated $\theta_w(j, I_{b,j-1})$ for three data sets: (1) The rain gauge record from the Osservatorio Ximeniano in Florence, Italy, (2) the radar sequences GATE-1 and GATE-2 from the tropical North Atlantic Global Atmosphere Research Program (GARP) Atlantic Tropical Experiment (GATE), and (3) a sequence of measurements from the doppler radar at S. Pietro Capofiume near Bologna, Italy.

Veneziano *et al.* (2003) find that C_0 decreases with increasing I_{dj-1} . This is so because: (1) more intense precipitation is generally associated with more compact rainfall support, and (2) the limited sensitivity of radars artificially increases the number of zeros in the sample and hence the sparseness of the rainfall support. They also find that C_0 increases with decreasing region size. This decrease is due at least in part to the radar sensitivity threshold.

The index of stability α ranges from 1 to 1.8, with higher values for smaller averaging volumes and higher I_{dj-1} . Also the parameter C_1 is found to depend on both I_{dj-1} and the size of the averaging volume.

4.1.4 Universal multifractal model

Based on properties of hydrodynamic turbulence, Lovejoy and Schertzer (1995) developed a multifractal model for rainfall. The model uses three parameters: C_1 , α , and H , to describe the scaling properties of rainfall and is obtained as follows.

In turbulent fields the velocity shear u^* between two points at distance l scales with l as,

$$u^* \sim (\varepsilon_l)^{1/3} l^{1/3} \quad (4.22)$$

where ε_l is the kinetic energy flux per unit mass at scale l . This energy transfer takes place from larger to smaller scales and follows the conservation property $E[\varepsilon_l] = \text{constant}$ (independent of scale).

In analogy with turbulence, Lovejoy and Schertzer (1995) hypothesize the existence for rainfall of a fundamental field φ_l with the same conservation property as ε_l . Then they argue that the rainfall fluctuations ΔR_l at scale l are given by:

$$\Delta R_l \sim (\varphi_l)^\alpha l^H \quad (4.23)$$

where α and H are constants independent of scale l . Notice that the model is in terms of fluctuations of the rainfall intensity field and contrasts with stationary multifractal cascade models. Also, the amplitude of the rainfall fluctuations is scale dependent and decreases as the observation scale l decreases. This is in agreement with the findings of Menabde and Sivapalan (2000) for temporal rainfall scaling, and Perica and Foufoula-Georgiou (1996b) for spatial rainfall scaling.

Lovejoy and Schertzer (1995) do not specify the physical meaning of φ_l and α . In fact, they state that a physical meaning cannot be given, since no proper dynamical theory for rain exists.

However, H has a straight forward interpretation: it specifies the extent to which the measured field R differs from the conserved field φ . In fact, H is the order of fractional integration required to obtain R from φ . This concept can be related to energy dissipation mechanisms existing in the atmosphere.

The conserved field φ is modeled by Lovejoy and Schertzer (1995) as a multiplicative cascade with log-Levy generator with index α and maximum negative skewness $\beta = -1$ (on Levy stable distributions see for example Samorodnitsky and Taqqu, 1994). The bare moment scaling function is,

$$K_{b,\varphi}(q) = \begin{cases} \frac{C_1}{(\alpha-1)} (q^\alpha - q), & \alpha \neq 1 \\ C_1 q \ln(q) & , \alpha = 1 \end{cases}, \text{ for } 0 < \alpha \leq 2 \text{ and } q \geq 0 \quad (4.24)$$

with associated Legendre transform (see Section 2.2),

$$c_{b,\varphi}(y) = \begin{cases} C_1 \left(\frac{y}{\alpha' C_1} + \frac{1}{\alpha} \right)^{\alpha'}, & \alpha \neq 1 \\ C_1 \exp\left(\frac{y}{C_1} - 1 \right), & \alpha = 1 \end{cases}, \text{ for } 0 < \alpha \leq 2 \quad (4.25)$$

where $\frac{1}{\alpha} + \frac{1}{\alpha'} = 1$.

One can prove that the bare moment scaling function of the fractionally integrated R field, $K_{b,R}(q)$ is

$$K_{b,R}(q) = \begin{cases} \frac{C_1}{(\alpha-1)} (q^\alpha - q) + qH, & \alpha \neq 1 \\ C_1 q \ln(q) + qH & , \alpha = 1 \end{cases}, \text{ for } 0 < \alpha \leq 2 \text{ and } q \geq 0 \quad (4.26)$$

with Legendre transform,

$$c_{b,R}(\gamma - H) = \begin{cases} C_1 \left(\frac{\gamma}{\alpha' C_1} + \frac{1}{\alpha} \right)^{\alpha'}, & \alpha \neq 1 \\ C_1 \exp\left(\frac{\gamma}{C_1} - 1\right), & \alpha = 1 \end{cases}, \text{ for } 0 < \alpha \leq 2 \quad (4.27)$$

The critical order of dressed moment divergence, q^* , is the same for φ and R and satisfies:

$$K_{b,\varphi}(q^*) = K_{b,R}(q^*) - (q^*)H = (q^* - 1) d \quad (4.28)$$

where d is the Euclidean dimension of the observation space.

Applications of this model to various gauge and radar rainfall records (Seed, 1989; Tessier *et al.*, 1993; Hubert *et al.*, 1993; Ladoy *et al.*, 1993) give $\alpha \approx 1.35 \pm 0.1$ and $C_1 \approx 0.16 \pm 0.05$. The value of H is poorly conditioned and ranges from 0 to 0.75.

4.1.5 Discussion and review

Several studies find that rainfall fields deviate from an exact multifractal behavior, which requires the cascade generator to be scale and “state” invariant. Specifically, these studies find dependence of the generator (i.e. fractal dimension and amplitude of multiplicative fluctuations) on the scale (Perica and Foufoula-Georgiou, 1996b; Veneziano *et al.*, 1996; Menabde *et al.*, 1997; Menabde and Sivapalan, 2000) and on the rain rate of the immediately higher scale (Veneziano *et al.*, 2003). In the previous sections we reviewed rainfall models proposed to capture such deviations.

The bounded cascade model of Menabde and Sivapalan (2000) is for temporal rainfall, and uses the technique of Breakdown Coefficients (BDCs) to account for changes with scale j of the marginal distribution of the generator W_j . The PDFs of the BDCs are empirically derived and then smoothed by fitting an analytic PDF with parameters that depend on j . This dependence accounts for almost linear decrease of the standard deviation of the BDCs with increasing scale j ; see Table 4.1 and Figure 4.2.

The model of Perica and Foufoula-Georgiou (1996b) is for spatial rainfall downscaling, and it is based on wavelet decomposition. The model assumes that the standardized rainfall fluctuations have normal distribution and simple scaling behavior. The scaling parameters of the model are the same for all spatial directions and they are linearly related to the Convective Available Potential Energy (CAPE) of the prestorm environment. This is equivalent to accounting for dependencies of the generator on the spatial scale in the form of a bounded cascade model similar to the one of Menabde and Sivapalan (2000); see Table 4.2 and Figure 4.4.

Although both previous studies found an almost linear decay of the standard deviation of the generator with increasing log-resolution, reconciliation of the obtained results assuming isotropy of rainfall in space and time is not feasible; see Section 4.1.2. However, one should be cautioned that this is not an indication of anisotropy of rainfall in space and time, since the data sets used by the two studies have different scaling behavior. Specifically, Menabde and Sivapalan (2000) use continuous rainfall records, whereas Perica and Foufoula-Georgiou (1996b) use data from storms; see Section 4.1.2.

Next, we reviewed two multiplicative cascade models with dependence on the large scale rainfall intensity. The model of Over and Gupta (1996) is for spatial rainfall with beta-lognormal generators that depend on the average rainfall intensity over the radar frame but are independent of scale. Thus the model of Over and Gupta (1996) is multifractal in space. The model of Veneziano *et al.* (2003) is similar to the one of Over and Gupta (1996) but assumes that the generator has beta-logstable distribution with parameters that depend on the scale and the bare rainfall intensity in the parent cascade tile.

Finally, we discussed the universal multifractal model of Lovejoy and Schertzer (1995). This model is based on properties of turbulence and uses three parameters: the co-dimension coefficient C_1 , the Levy index of the generator α , and the order H of fractional integration. The model is in terms of fluctuations of the rainfall intensity field and contrasts with stationary multifractal cascade models. Also the model accounts for decrease of the amplitude of the multiplicative fluctuations with increasing resolution. Such a scaling behavior is in agreement with the findings of Menabde and Sivapalan (2000) for temporal rainfall scaling, and Perica and Foufoula-Georgiou (1996b) for spatial rainfall scaling.

Concluding, one can say that space-time rainfall violates perfect scale invariance, since the amplitude of the multiplicative fluctuations decreases with increasing space-time resolution. Therefore, one can describe the effect of scale on rainfall using a bounded cascade model in two spatial dimensions plus time, where the standard deviation of the generator decreases with increasing resolution. A model of this type is used in Section 4.3.1 to simulate ARFs for a bounded space-time representation of rainfall.

4.2 Raingauge network density and deviations from multifractality

Areal reduction factors are typically estimated from raingauge network records, which have time intervals much larger than radar measurements. A problem with raingauge networks is that they have a finite density ρ . For example the network used in the N.E.R.C. (1975) study is shown in Figure 4.5.

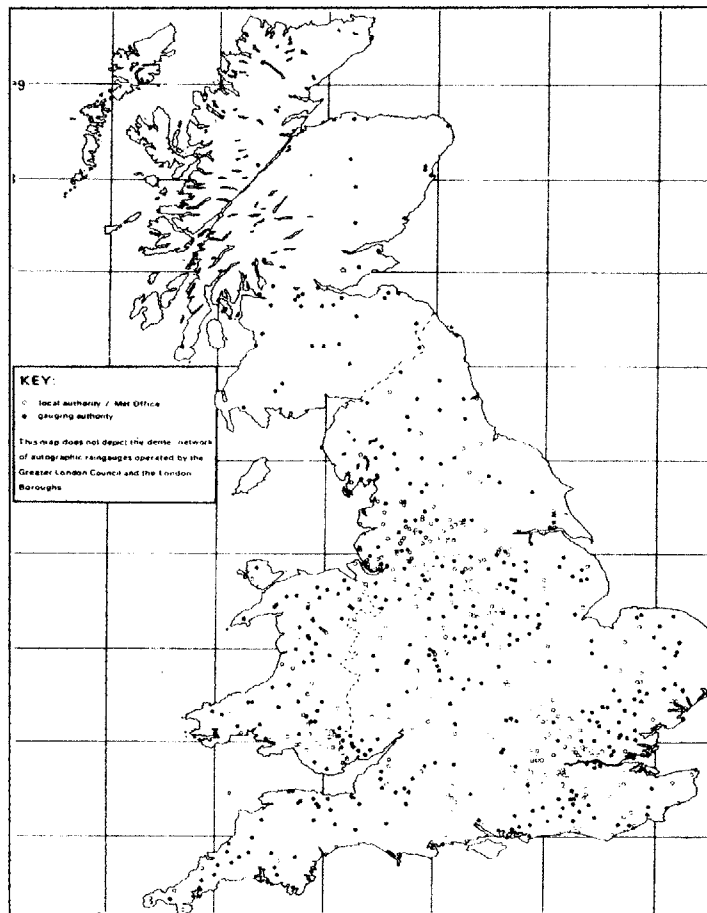


Figure 4.5: Locations of autographic raingauges in Great Britain. Reproduced from N.E.R.C. (1975) *Flood Studies Report*, Vol. IV, p. 24. Grid dimension 100 × 100 Km.

The average rain-rate in a basin of area A is estimated as the average rain-rate measured by the raingauges inside A . If the raingauge network is fixed, the average number of raingauges in A , $\tilde{N}(A)$ is proportional to A . However, not to disturb rainfall scaling relations including the ARF, \tilde{N} should not depend on A .

The bias is larger as A decreases and is maximum when A includes just one raingauge; see Section 4.3.2 for numerical examples.

4.3 Effect of bounded cascade modeling and sparse sampling on the ARF

In Chapter 3 we investigated the scaling properties of the ARF with the maximum linear size of the region L and the averaging duration D , under the assumption of exact multifractal behavior of the rainfall field and perfect observations. Here we illustrate numerically the effects that deviations from multifractality and sparse spatial sampling have on the estimated ARFs.

First we investigate how the ARF behaves under a bounded cascade representation of the rainfall field in space and time (Section 4.3.1). We do so because many studies (e.g. Perica and Foufoula-Georgiou, 1996b; Veneziano *et al.*, 1996; Menabde *et al.*, 1997; Menabde and Sivapalan, 2000; Veneziano *et al.*, 2003) have found that space-time rainfall violates perfect scale invariance with the amplitude of the multiplicative fluctuations to decrease as the space-time resolution increases; see Section 4.1.

Finally, we show the effects that the sparsity of point observations has on the estimated ARFs (Section 4.3.2).

4.3.1 Bounded lognormal cascade

Here we investigate the properties of the ARF for a bounded lognormal cascade representation of rainfall in two spatial dimensions plus time. The model used is a 3D bounded lognormal (LN) cascade.

The cascade has multiplicity 2 in all dimensions. The generator of the cascade, B_n , has unit mean and LN distribution that varies with level n as

$$\ln(B_n) \sim N\left(-\frac{\sigma^2(n)}{2}, \sigma^2(n)\right) \quad (4.29)$$

where $N(\mu, \sigma^2)$ is the normal distribution with mean value μ and variance σ^2 , and $\sigma^2(n)$ is given below.

The numerical simulation procedure is identical to the one described in Section 3.3.1. The 3D cascade was generated in a region with spatial dimension $2^6 \times 2^6$ tiles and temporal dimension 2^9 tiles, embedded in a 3D cascade cube with edge dimension 2^9 tiles; see Figure 3.26.

To reduce statistical variability and focus on the mean effect of using a bounded cascade model, the results were averaged over 10 simulations.

The standard deviation $\sigma(n)$ of the generator B_n is assumed to decay linearly with the cascade level n as shown in Figure 4.6. This type of decay is similar to the one found by Menabde and Sivapalan (2000) and Perica and Foufoula-Georgiou (1996b); see Figures 4.2 and 4.4.

Figure 4.7 shows how the ARF varies with L and D , and should be compared with Figure 3.28, which shows similar results under exact multifractality. These two figures can be compared since $\sigma_B(0) = 0.385$ corresponds to $C_1 = 0.1$.

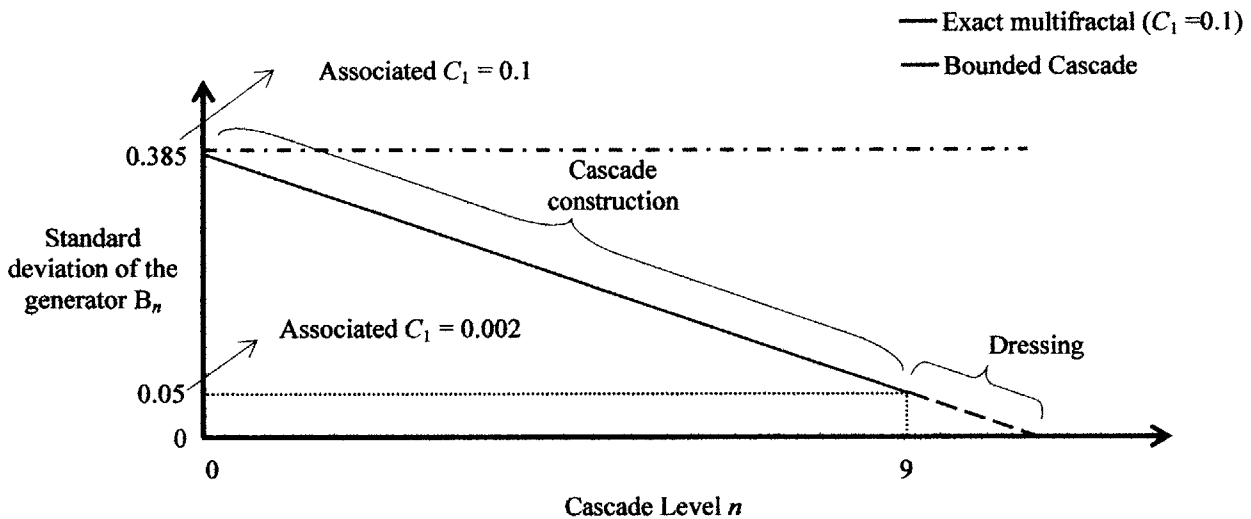


Figure 4.6: Standard deviation of the generator B_n of the bounded cascade with the scale n .

One can observe that the contour lines in Figure 4.7 are displaced upwards relatively to the multifractal case in Figure 3.28. The reason is that the bounded-cascade process is smoother than the multifractal process.

Also, the contour lines in Figure 4.7 are not straight. For small D and large L , the slope of the contour line is less than 1 and increases as L decreases or D increases. For a given L , the slope of the contour lines increases as D increases approaching 1, which is the slope for the multifractal case (see Figure 3.28), for large values of D .

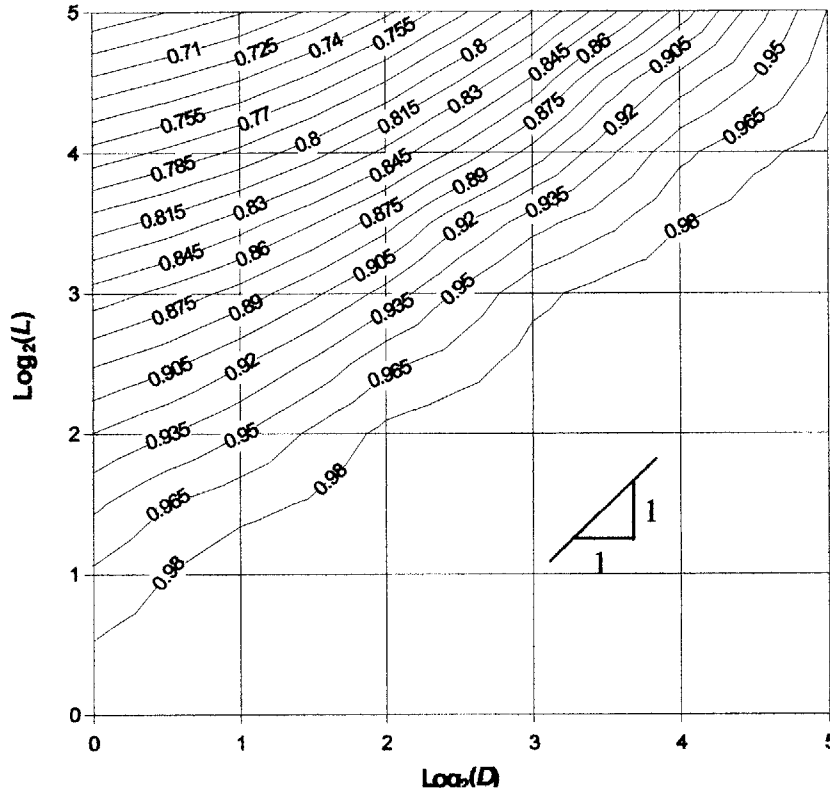


Figure 4.7: ARF scaling behaviour with L and D for a bounded cascade. The standard deviation of the generator of the cascade scales according to Figure 4.6.

4.3.2 Sparse sampling

When the ARF is estimated from raingauge measurements, the areal average rainfall is obtained as the average (or a weighted average; e.g. with Thiessen weights) of the raingauge measurements inside the region.

Unless the observation network scales itself with L , this operation destroys the scaling properties of the ARF. Scaling of the observation network with L can be obtained by the dressing procedure followed in Section 3.3.1, which we call “*continuous*” sampling. Of course, such kind of scaling does not exist in real raingauge networks, which have a finite density.

Discrete sampling can be simulated by substituting $I_{d,3}(x, y, t)$ with $I_{d,1}(x, y, t)$ in equation (3.22), and keeping the rest of the procedure in Section 3.3.1 unchanged. In this case, the area tiles at the highest resolution of the cascade can be viewed as observation points (i.e. raingauges).

One can also study the effects of the observation network density by symmetrically reducing the number of observation points (raingauges) in the simulated space region.

As in Section 3.3.1, the model used is a lognormal multifractal cascade with two spatial dimensions plus time and co-dimension coefficient $C_1 = 0.1$. The simulation region has spatial dimension $2^6 \times 2^6$ tiles and temporal dimension 2^9 tiles. Thus, the maximum possible number of observation points (raingauges) in the simulated region is $2^6 \times 2^6$. To reduce statistical variability, the results were averaged over 10 independent simulations.

Figures 4.8, 4.9 and 4.10 show how the ARF varies with L and D for the case of sparse sampling and different numbers, k , of observations points (i.e. $k = 2^{12}, 2^{10}, 2^8$).

By comparing Figures 4.8, 4.9 and 4.10 with Figure 3.28 (i.e. continuous sampling), one concludes that for large L the ARF values are not influenced by the type of sampling (i.e. continuous or sparse). This means that the effect of sparse sampling becomes less significant as L increases.

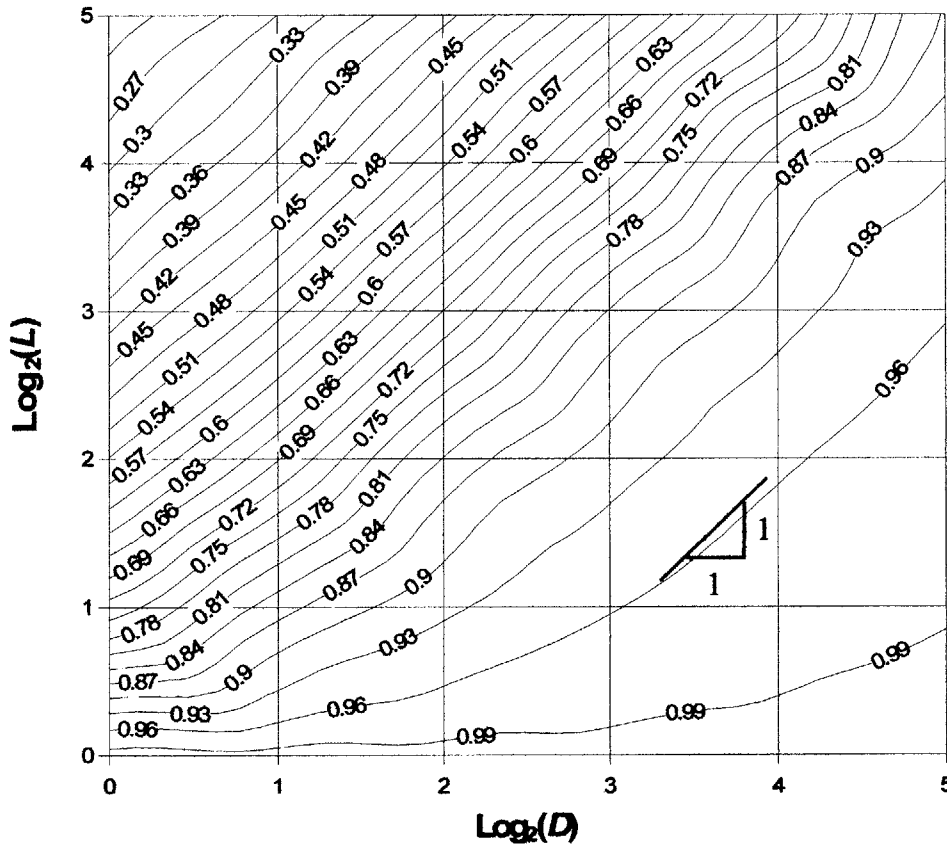


Figure 4.8: ARF scaling behaviour with L and D for sparse sampling ($k = 2^{12}$). The model used is a 3D binary LN discrete cascade with co-dimension coefficient $C_1 = 0.1$.

For the limiting case of regions that include only one observation point the calculated ARF is approximately 1. For intermediate areas, the contour lines are curved indicating no scaling of

the ARF. Quantitatively, this behaviour is similar to that under continuous sampling for a bounded cascade representation of rainfall.

The curvature of the iso-ARF lines becomes larger as the observation network density decreases. Also, the effect of sparse sampling becomes less significant as L increases. This is so because, when the averaging area A increases, the characteristic length of the fluctuation that contributes most to the spatial average increases with $A^{0.5}$. On the other hand, the distance between the equally spaced observation points remains constant. Thus, according to Nyquist theorem when the length of the characteristic fluctuation becomes larger than twice the distance between two observation points at the highest resolution of the grid, the characteristic fluctuation is accurately described and the ARF values obtained are close to those for continuous sampling.

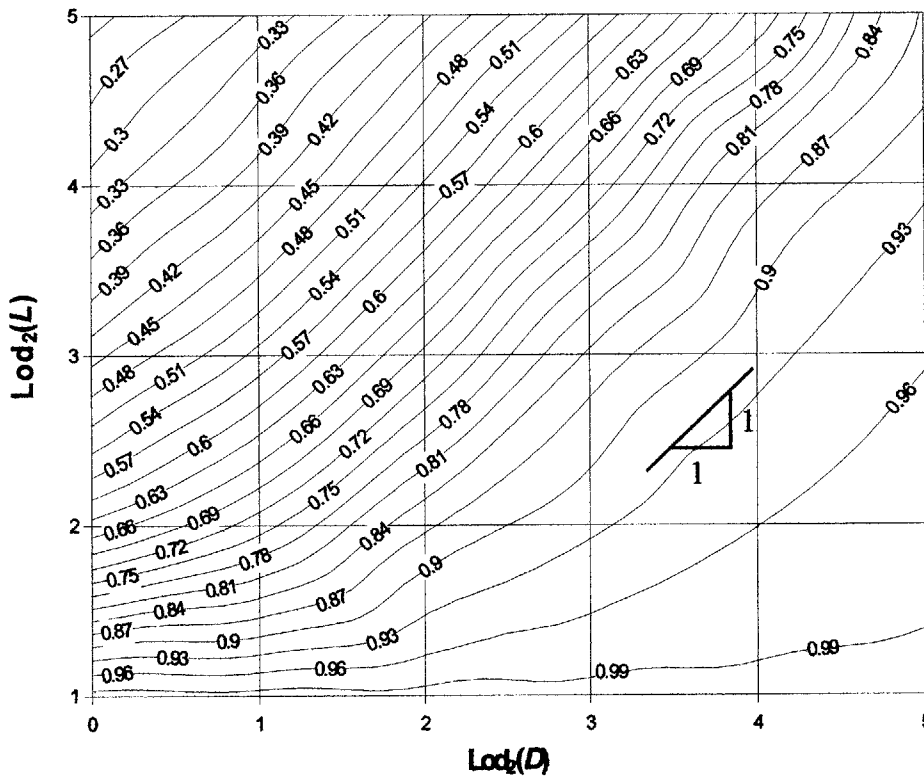


Figure 4.9: ARF scaling behaviour with L and D for sparse sampling ($k = 2^{10}$). The model used is a 3D binary LN discrete cascade with co-dimension coefficient $C_1 = 0.1$.

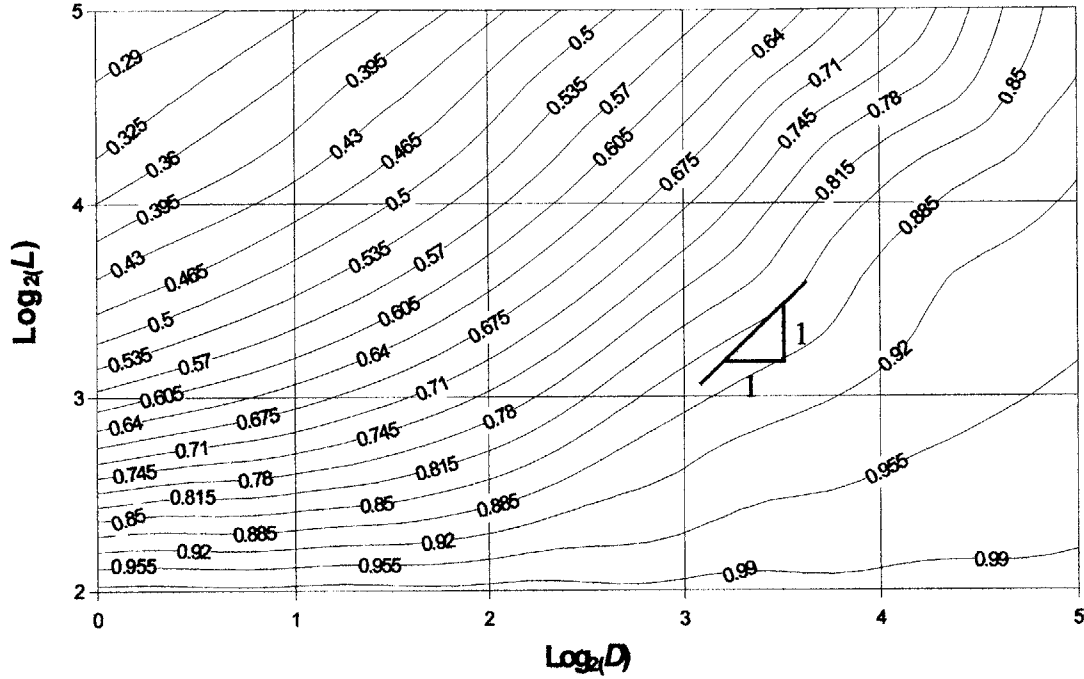


Figure 4.10: ARF scaling behaviour with L and D for sparse sampling ($k = 2^6$). The model used is a 3D binary LN discrete cascade with co-dimension coefficient $C_1 = 0.1$.

For equally spaced raingauges the latter condition is maintained for $A^{0.5}$ larger than about four times the distance between the observation points; see Figures 4.8, 4.9 and 4.10.

4.3.3 Conclusions

We have investigated numerically the effects that deviations of rainfall from multifractality in the form of bounded cascades have on the ARFs. We have also studied the effects of sparse spatial sampling on the estimated ARFs for different densities of the raingauge network. We have found that the ARF values as well as the slope of the iso-ARF curves are affected by both deviations from multifractality and sparse spatial sampling.

In bounded cascades the iso-ARF curves are displaced upwards relatively to the exact multifractal case. Also, the iso-ARF curves in a $(\log D, \log L)$ plane have slopes that vary with L and D . For small D and large L , the slope of the contour lines is less than 1 and increases as L decreases or D increases. For a given L , the slope of the contour lines increases as D increases approaching 1 for large values of D .

In the case of sparse spatial sampling, results for large L are close to those under continuous sampling. This means that the effect of sampling becomes less significant as L increases. For low values of L , the slope of the iso-ARF lines is less than 1 and increases fast as L increases

approaching 1 for high values of L where the effect of sparse sampling is negligible. The value of L over which the effect of the sparse sampling can be neglected increases as the network density decreases.

5. Application to the N.E.R.C. curves

In this chapter we show how various features of empirical Areal Reduction Factors (ARFs) are related to the multifractal character of rainfall, deviations from multifractality in the form of bounded cascades, and sparse spatial sampling. For this purpose we use the ARFs of N.E.R.C. (1975) for area A ranging from 10 to 18 000 Km² and duration D between 2 minutes and 25 days.

The chapter is organized as follows. Section 5.1 discusses N.E.R.C.'s original data and final ARF results. We also re-fit the original data using minimum smoothing. The resulting ARF diagram is used for the rest of the analysis.

In Section 5.2, features of the N.E.R.C. iso-ARF lines are discussed and linked to results under the assumption that space-time rainfall is multifractal (Chapter 3) or deviates from multifractality in certain ways (Chapter 4).

Section 5.3 focuses on reproducing the N.E.R.C. iso-ARF curves using multifractal and bounded cascade models, as well as sparse sampling.

Conclusions and comments are presented in Section 5.4.

5.1 N.E.R.C.'s ARF curves

In 1975, the Natural Environmental Research Council (N.E.R.C.) published results on the dependence of the ARF on catchment area A and averaging duration D . The analysis was based on the estimated ARFs from thirteen basins in the United Kingdom with areas ranging from 10 to 18 000 Km². Averaging durations ranged from 2 minutes to 25 days; see Table 5.1. According to N.E.R.C. (1975), these ARFs correspond to rainfall events with return period $T = 2$ -3 years.

The ARF values in Table 5.1 were first interpolated and then extrapolated by N.E.R.C. to cover a wider range of catchment areas (from 1 to 30 000 Km²) and averaging durations (from 1 minute to 25 days); see Table 5.2. A Contour plot of the ARF for a sub-region of Table 5.2 was also produced by N.E.R.C.; see Figure 5.1. The red dots indicate area-duration combinations in the original data.

Table 5.1: ARFs estimated by N.E.R.C. for widely different region sizes and averaging durations. The values corresponding to the red dots given in Figure 5.1 are denoted on red. Reproduced from N.E.R.C. (1975) *Flood Studies Report*, Vol. II, p. 38-39.

Duration	Area (sq. km)							
	10	100	1000	1500	5000	8000	10000	18000
2 min	0.67	-	-	-	-	-	-	-
4 min	0.74	-	-	-	-	-	-	-
10 min	0.85	-	-	-	-	-	-	-
15 min	-	0.62	0.39	-	-	-	-	-
30 min	0.88	0.73	0.51	-	-	-	-	-
60 min	0.9	0.77	0.62	-	-	0.47	-	0.4
2 hours	-	0.84	0.75	-	-	0.57	-	0.51
3 hours	-	-	-	-	-	0.64	-	0.57
6 hours	-	-	-	-	-	0.74	-	0.67
1 day	-	0.94	-	0.89	0.84	0.83	0.82	0.81
2 days	-	0.97	-	0.91	0.85	0.85	0.83	0.83
4 days	-	0.97	-	0.92	0.88	0.87	0.87	0.84
8 days	-	0.97	-	0.93	0.89	0.91	0.89	0.87
25 days	-	0.99	-	0.97	0.94	0.95	0.94	0.93

Table 5.2: ARFs after interpolation and extrapolation of the original ARF results (Table 5.1). Reproduced from N.E.R.C. (1975) *Flood Studies Report*, Vol. II, p. 41.

Duration	Area (sq. km)									
	1	5	10	30	100	300	1000	3000	10000	30000
1 min	0.76	0.61	0.52	0.40	0.27	-	-	-	-	-
2 min	0.84	0.72	0.65	0.53	0.39	-	-	-	-	-
5 min	0.90	0.82	0.76	0.65	0.51	0.38	-	-	-	-
10 min	0.93	0.87	0.83	0.73	0.59	0.47	0.32	-	-	-
15 min	0.94	0.89	0.85	0.77	0.64	0.53	0.39	0.29	-	-
30 min	0.95	0.91	0.89	0.82	0.72	0.62	0.51	0.41	0.31	-
1 hour	0.96	0.93	0.91	0.86	0.79	0.71	0.62	0.53	0.44	0.35
2 hours	0.97	0.95	0.93	0.90	0.84	0.79	0.73	0.65	0.55	0.47
3 hours	0.97	0.96	0.94	0.91	0.87	0.83	0.78	0.71	0.62	0.54
6 hours	0.98	0.97	0.96	0.93	0.90	0.87	0.83	0.79	0.73	0.67
1 day	0.99	0.98	0.97	0.96	0.94	0.92	0.89	0.86	0.83	0.80
2 days	-	0.99	0.98	0.97	0.96	0.94	0.91	0.88	0.86	0.82
4 days	-	-	0.99	0.98	0.97	0.96	0.93	0.91	0.88	0.85
8 days	-	-	-	0.99	0.98	0.97	0.95	0.92	0.90	0.87
25 days	-	-	-	-	0.99	0.98	0.97	0.95	0.93	0.91

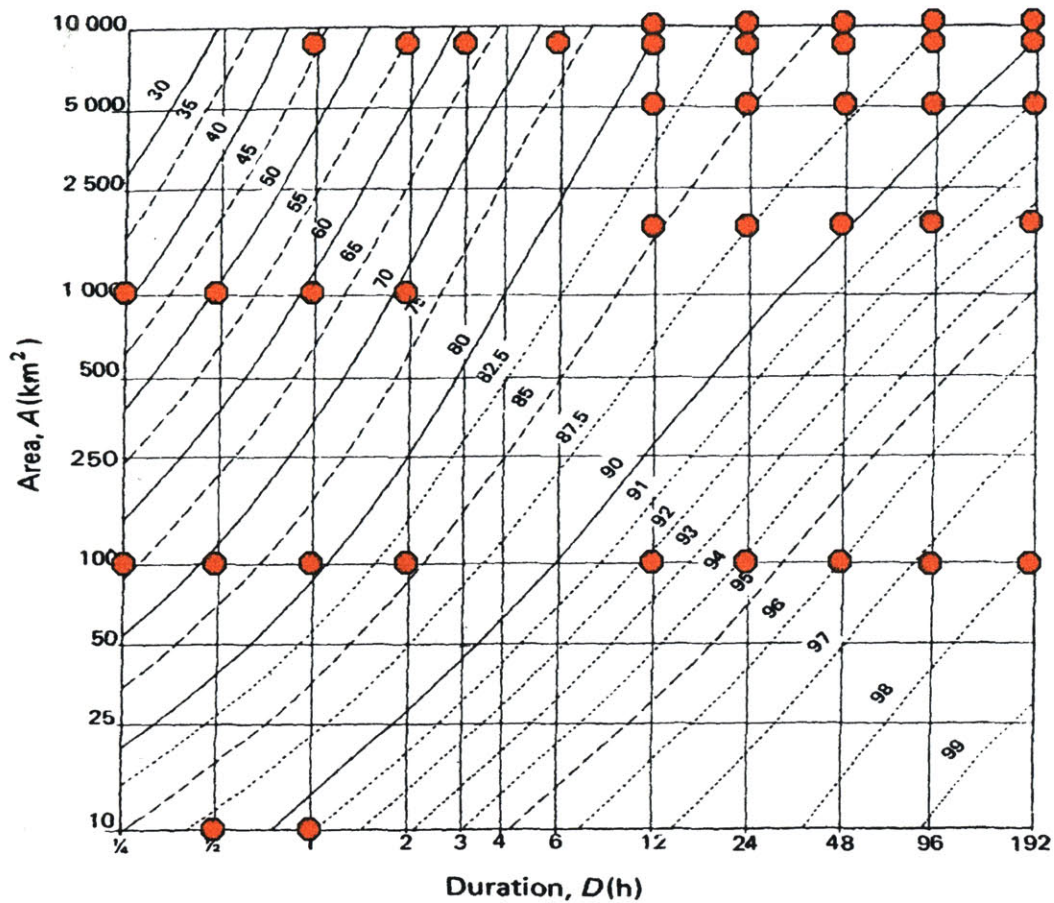


Figure 5.1: ARFs for durations D from 15 minutes to 8 days and areas A from 10 to 10 000 Km^2 . Reproduced from N.E.R.C. (1975) *Flood Studies Report*, Vol. II, p. 40. Red dots correspond to areas and durations from the original results (Table 5.1).

The interpolated results fit well the original data only for certain combinations of A and D . Thus, judgment must have been used in producing the smooth iso-lines in Figure 5.1.

To more faithfully reflect the original data, we have re-interpolated the empirical ARF values in Table 5.1 using simple 1st order triangulation. The results are shown in Figure 5.2.

In this interpolation method a triangular grid is constructed with nodes at the points where the original ARF values are given. Each triplet of points at the highest resolution of the grid defines a plane. This plane is used as a linear approximation of the ARF function inside the associated triangle.

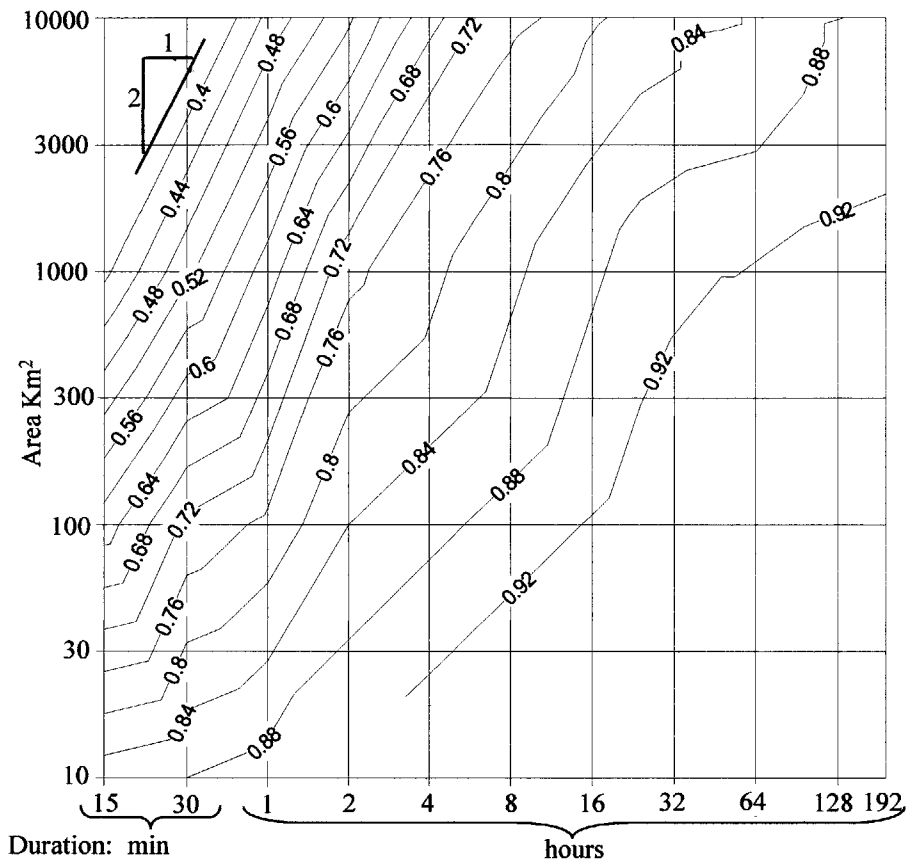


Figure 5.2: Interpolation of the ARF results in Table 5.1 using the method of 1st order triangulation.

Notice that the iso-lines in Figure 5.2 have different shape and overall slope than those in Figure 5.1. This is due to differences in the interpolation method. For the rest of our analysis we use the interpolated ARF results in Figure 5.2. We do so because the interpolation method used is known and the observed values are preserved.

Next we discuss the shape, slope and curvature of the iso-ARF curves in Figure 5.2, and how these features relate to those for exact multifractal rainfall or rainfall that deviates from multifractality.

5.2 Behavior of the ARF in Figure 5.2

In Figure 5.2, one may distinguish four regions where the iso-ARF curves have different behavior. These regions are shown in Figure 5.3.

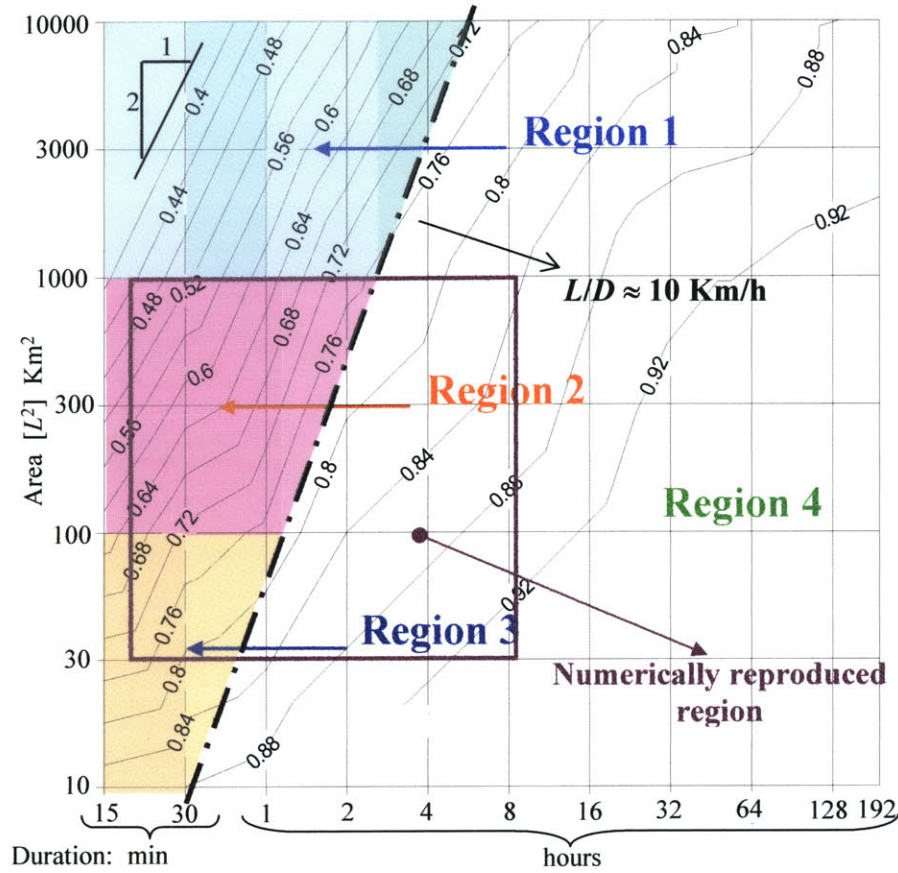


Figure 5.3: Regions of different ARF scaling behavior.

Region 1 displays scaling of the ARF. Specifically, the ARF is constant for D proportional to the square root of the area A (i.e. $D \propto L$). This is in agreement with results in Chapter 3 under the assumption that rainfall is isotropically multifractal in space and time.

In Region 2, one observes that, as the area A or duration D decreases, the slope of the iso-ARF curves decreases. This effect is gradual and the slope changes are small. This behavior can be explained assuming that rainfall is well represented by a bounded cascade in space and time, where the amplitude of the multiplicative fluctuations decreases at smaller scales; see Section 4.3.1.

Region 3 shows a much more pronounced variation of the iso-ARF slope with A and D . The slope becomes quite small for small areas and durations. This behavior is similar to the one produced by sparse spatial sampling; see Section 4.3.2.

In Region 4, where A and D are relatively large, one observes that the spacing of the iso-ARF curves is larger relative to the other three regions and increases as the duration D increases. This effect has been observed in beta log-normal cascades for both small and large values of the ratio L/D ; see Section 3.3.1.2. However, in Figure 5.3 this is observed only for small L/D ratios (say $L/D < 10$ Km/h). This feature of the observed ARFs may be related to the characteristic linear sizes and lifetimes of precipitation areas.

Specifically, in Table 3.6 one can observe that large mesoscale precipitation areas (say $10\,000$ Km²) have relatively small lifetimes (say several hours). This means that for D less than several hours, the non rainy space-time regions are associated with a beta component that characterizes the precipitation event itself, whereas for D larger than several hours non rainy space-time regions are associated with large-scale atmospheric transfer mechanisms (i.e. dry periods between precipitation events). Therefore, one can accept a discontinuity of the beta component in space and time. For D small the effect of a beta component is not significant and can be accurately substituted by increasing the amplitude of the multiplicative fluctuations, whereas for D large the beta component becomes significant in space or time and cannot be neglected.

One can also obtain an estimation of the value of L/D over which the beta component becomes significant. Suppose that mesoscale precipitation areas have a characteristic linear size of about 100 Km and lifetime of about 10 hours. In this case, the singularity of the rainfall field will start to significantly affect the observed ARFs for L/D ratios smaller than 10 Km/h. This result is in correspondence with what one observes in Figure 5.3.

Although the increased spacing of the iso-lines in Figure 5.3 extends to durations smaller than several hours, one should be cautioned that in this region only a few empirical ARF values are available (see Figure 5.1), and thus the accuracy of the interpolation is limited. Furthermore, the ARF values in that region are close to 1 , and thus even small distortions of the estimated ARFs caused by inaccuracies and statistical fluctuations highly affect the shape, slope and curvature of the empirical iso-ARF curves.

5.3 Numerical reproduction of the N.E.R.C. ARF results

Here we show how the N.E.R.C. ARF results in Figure 5.3 can be reproduced. For efficiency of the calculations¹, we focus on the sub-region with A in the range 30-1000 Km², and D in the range 15 min-6 hours. A magnification of this region is presented in Figure 5.4.

The region was selected because it includes all different observed ARF behaviors, except for Region 1. However, in Region 1 the ARF behaves in a way similar to exact multifractal cascades. Hence, one can obtain the ARF values for this region by extrapolating the iso-ARF curves of Region 2 using $D \propto A^{0.5}$.

Next we describe the models used to reproduce the empirical ARFs in Regions 2, 3 and 4.

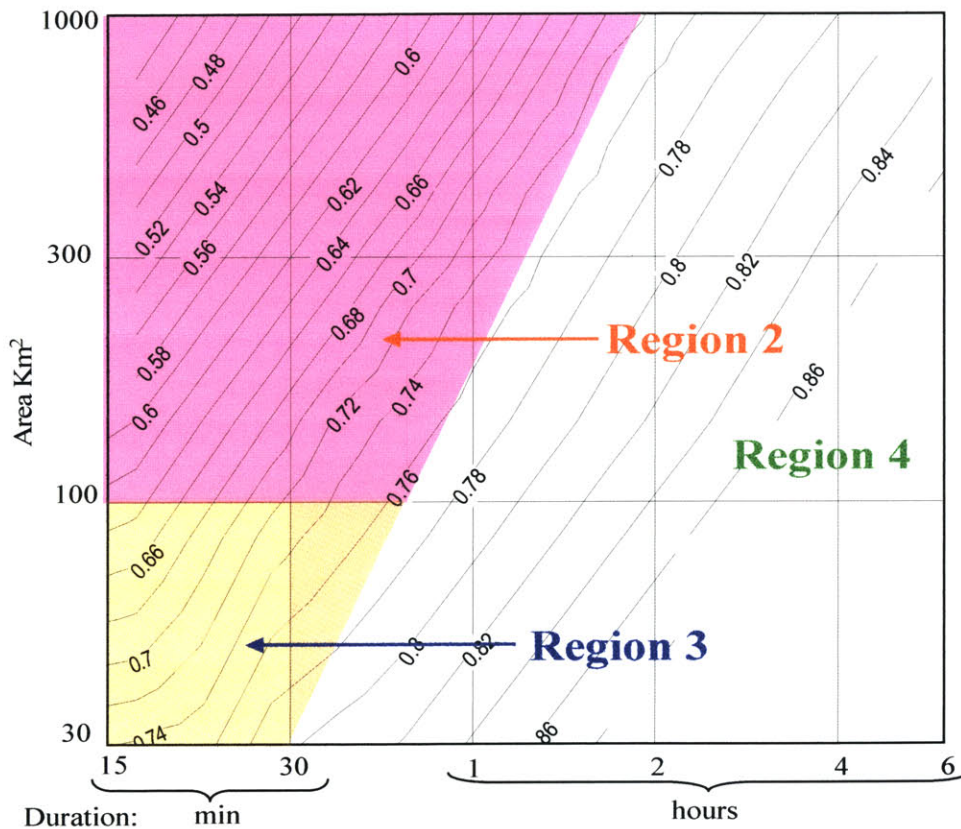


Figure 5.4: Magnification of the numerically reproduced region. Reproduced from Figure 5.3.

5.3.1 Numerical reproduction of Regions 2 and 3

The model used is a bounded Log-Normal (LN) cascade in two spatial dimensions plus time. The cascade has multiplicity 2 in all dimensions. The generator of the cascade, B_n , has a LN

¹ In general 3D cascade simulations require large computational times. Therefore, a 3D cascade that covers the whole range of areas and durations shown in Figure 5.3 cannot be generated and manipulated.

distribution with mean value 1 and variance that varies with the level n . Hence $\ln(B_n)$ has normal distribution,

$$\ln(B_n) \sim N\left(-\frac{\sigma(n)^2}{2}, \sigma(n)^2\right) \quad (5.1)$$

where $\sigma(n)^2$ is a function described below.

The space-time region simulated is a parallelepiped with spatial dimensions $2^6 \times 2^6$ tiles and temporal dimension 2^9 tiles, which is embedded in the 3D cascade; see Figure 3.26. This parallelepiped is considered to represent a rainy season of the year and includes 8 independent “storm” events in the form of isotropic multifractal cascades of size $2^6 \times 2^6 \times 2^6$; see Figure 5.5.

Each cubic tile at the highest resolution of the cascade is assumed to represent a space region with area 1Km^2 and a time interval of $\frac{1}{4}$ hours.

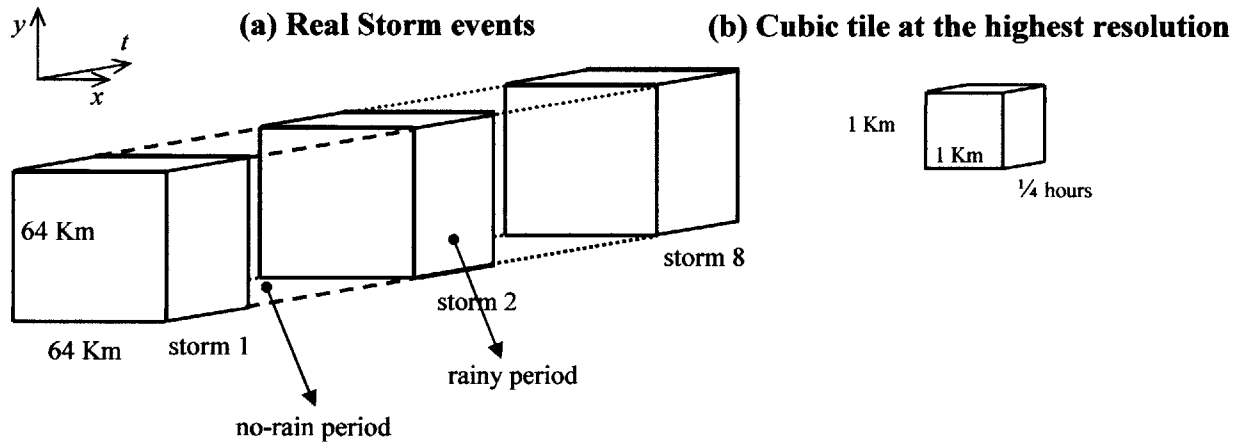


Figure 5.5: Simulation region

To simplify matters, the no-rain periods between storms are omitted. This assumption does not affect much the results for aggregation periods smaller than 2^6 cascade tiles (i.e. 16 hours). This is so because the estimation of the ARF is done by using maximum values observed in a given time period not average values.

The standard deviation $\sigma(n)$ of the generator is assumed to vary with the cascade level n according to Figure 5.6.

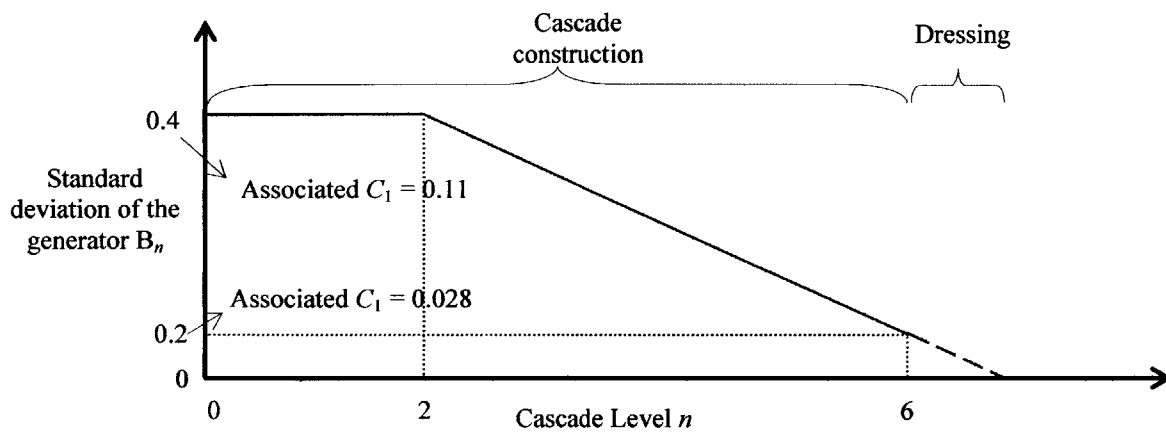


Figure 5.6: Standard deviation of the generator B_n of the bounded cascade with the scale n .

This behaviour is an approximation of the empirical findings of Menabde and Sivapalan (2000) for rainfall scaling in time; see Figure 5.7 and Section 4.1.1. For durations longer than those studied by Menabde and Sivapalan (2000), we assumed that the standard deviation of the generator remains constant and equal to that of the highest scale available. We follow those empirical findings because they are based on continuous rainfall records and not on storm data (e.g. Perica and Foufoula-Georgiou, 1996b; Section 4.1.2). Notice that the N.E.R.C. (1975) ARF results have also been obtained from continuous rainfall records. The present approximation assumes isotropy in all space and time directions.

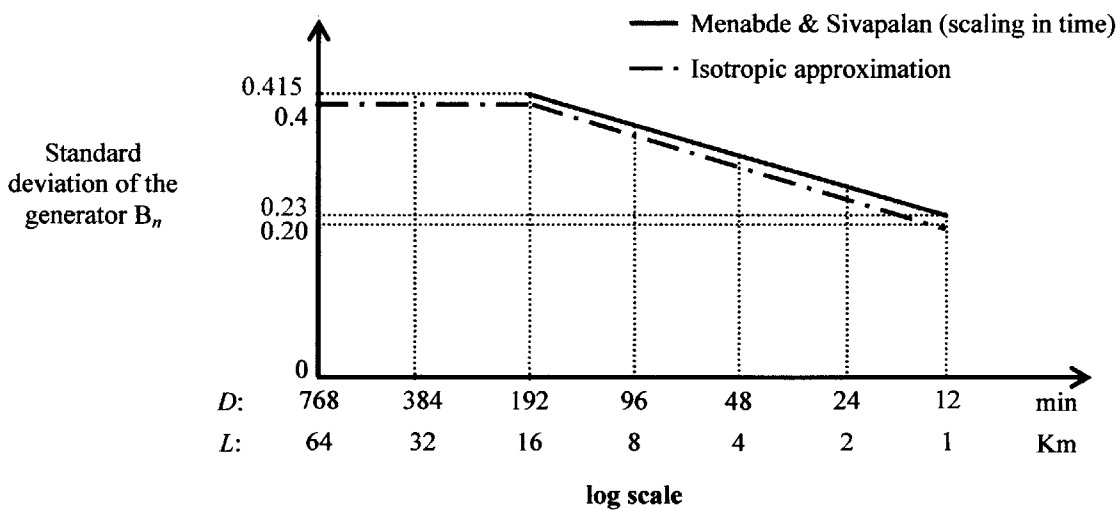


Figure 5.7: Comparison between the isotropic approximation used in the model, and empirical findings for rainfall.

Finally we considered the effect of sparse spatial sampling as described in Section 4.3.2. Specifically we assumed that area averaged rainfalls are obtained as averages over point measurements. The measurement locations were assumed to be regularly spaced with a density of 1 raingauge per 4 Km². This density seems comparable to the average raingauge density in the more densely sampled regions in Figure 4.5.

To reduce variability, the empirical ARF values were averaged over 10 independently simulated seasons.

Figure 5.8 shows the simulations results. The iso-lines in Regions 2 and 3 are in good agreement with those of Figure 5.3. Notice in particular the curved shape of the iso-lines in Region 3 caused by sparse sampling.

In Region 4 the agreement is less good. Next we will show that inclusion of a beta component can make the results in this region closer to those in Figure 5.3.

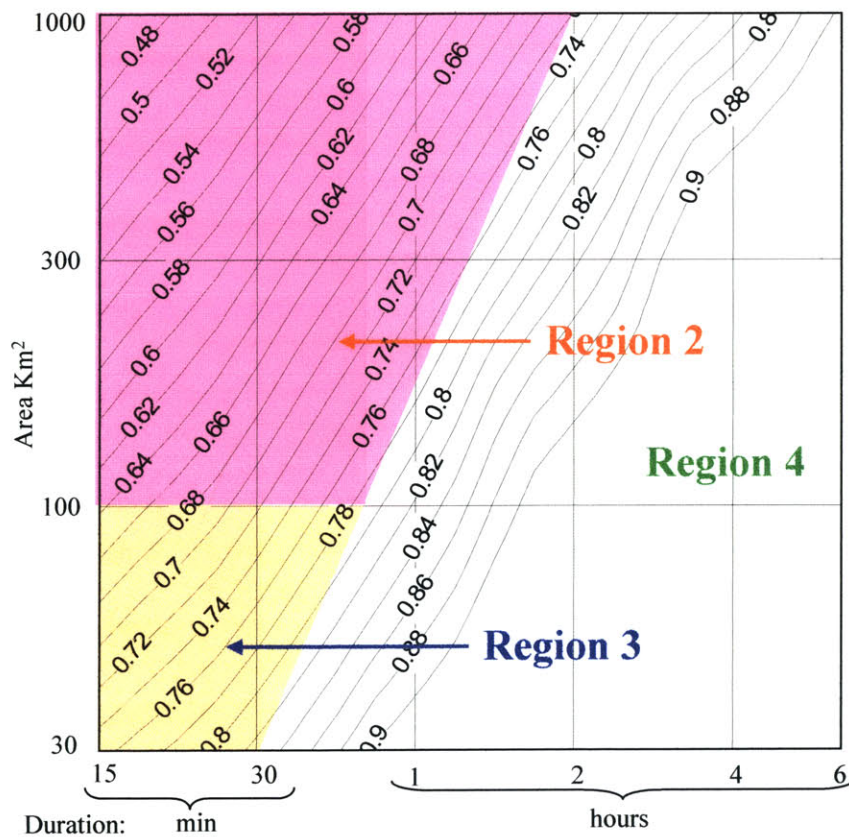


Figure 5.8: Numerically generated ARFs using a bounded 3D log-normal cascade. The sampling is discrete with density 1 raingauge per 4 Km².

5.3.2 Numerical reproduction of Region 4

For the purpose of reproducing the ARF values in Region 4, we use a 3D beta-LN cascade. The generator B has a non zero probability mass at $B = 0$ and $[B|B > 0]$ has log-normal distribution,

$$\ln(B) \sim N(-C_1 \ln(2), 2C_1 \ln(2)) \quad (5.2)$$

Notice that in this case the cascade is multifractal and not bounded. Also, in the simulations we have set $P_0 = P[B = 0] = 0.25$ and $C_1 = 0.1$. These values have been set to fit the empirical ARF curves in Region 4 and do not correspond to empirical observations.

The model is similar to that in Figure 5.5, but now a cubic tile at the highest resolution represents a space region with area 30 Km^2 and duration 6 minutes.

Finally, observations are assumed to be continuous in space (no sparse sampling). We do so because if one hypothesizes a density of 1 raingauge every 4 Km^2 (i.e same as the one hypothesized for Regions 2 and 3) then one has 7.5 raingauges in an area of 30 Km^2 , and therefore the effect of sparse sampling is small; see also Figure 5.8.

Figure 5.9 shows numerically generated ARFs (averages over 10 simulations). One observes that in Region 4 results are in good agreement with the N.E.R.C. values in Figure 5.3.

Since a beta-lognormal cascade fits well the empirical ARFs in Region 4, one could try to formulate a single model for all regions. However, the beta component seems to have pronounced effects on the ARF only for low values of the ratio L/D ; see Section 5.2. Hence, the beta component of the unified model should be effectively active only for Region 4 and not for Regions 2 and 3.

This may be possible by including a bounded beta component in the bounded cascade model of Section 5.3.1. In this case, the non zero probability mass P_0 should be almost constant for temporal scales larger than several hours, and decrease fast with scale to become negligible for temporal scales less than almost an hour.

Generating and analyzing such a 3D field is computationally not trivial, because the 3D field would have large dimensions (e.g $2^6 \times 2^6 \times 2^{12}$).

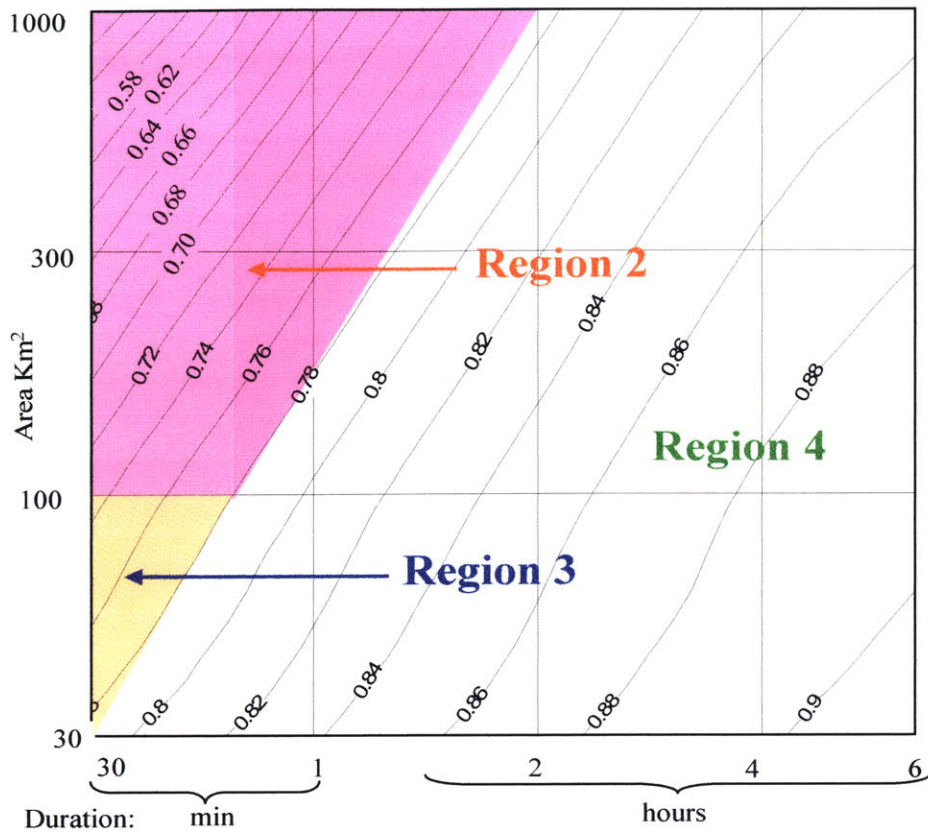


Figure 5.9: Numerically generated ARFs using a 3D beta log-normal cascade and continuous sampling.

5.4 Conclusions and comments

In the previous sections we used various rainfall and sampling models to interpret the ARFs of N.E.R.C. (1975).

For large areas and short durations, where the ARF attains the smallest values, the log-log slope of the empirical iso-lines is 2. This is consistent with multifractal rainfall.

Slopes smaller than 2 are observed for smaller areas. Such smaller slopes are produced by bounded cascades and by sparse spatial sampling. Sparseness of the raingauge network becomes most important at the smallest spatial scales.

The increased spacing of the iso-ARF curves for large D (Region 4 in Figure 5.3) may be related to a beta component associated with the characteristic linear sizes and lifetimes of mesoscale precipitation areas. However, one cannot neglect empirical biases and statistical errors in Region 4, for two reasons. First, only a few empirical ARF values are available in Region 4 (see Figure 5.1), and thus the accuracy of the interpolation is limited. Second, the ARF

values in that region are close to 1, and thus even small distortions of the estimated ARFs caused by inaccuracies and statistical fluctuations highly affect the shape, slope and curvature of the empirical iso-ARF curves.

A unified model for all regions may be possible. However, one should be aware that the beta component seems to have pronounced effects on the ARF only for low values of the ratio L/D . Such a model would then have to include a beta bounded cascade component in two spatial dimensions plus time, in which the non zero probability mass P_0 is almost constant for temporal scales larger than several hours, and decreases fast to become negligible for temporal scales less than almost an hour. However, this would require large cascade dimensions, which would increase the computational effort.

For this reason the numerical analysis performed for Regions 2, 3 and 4 was limited to two separate models; a bounded cascade model with sparse spatial sampling for Regions 2 and 3, and a beta multifractal model with continuous sampling for Region 4.

6. Conclusions

In this thesis we studied properties of the Areal Reduction Factor (ARF) for rainfall, with special attention for scaling (or non-scaling) behavior. We also linked such behavior to the scaling properties of rainfall itself. First, we reviewed existing theoretical results (i.e. Bendjoudi *et al.* (1999) and Veneziano and Furcolo (2002a)) on the extremes of point rainfall, obtained under the assumption that rainfall is multifractal in time. Then we extended the analysis to the average rainfall intensity inside regions of various shapes, again under the condition of multifractal rainfall in space and time. We considered regular (square or circular) regions and highly elongated regions and allowed the rainfall field to advect with constant velocity $\mathbf{v}_{ad} = [v_{ad,x}, v_{ad,y}]$. We found that the ARF scales with $A^{0.5} \propto D$, where A and D are the averaging area and duration respectively.

Case without advection

For the case when $\mathbf{v}_{ad} = \mathbf{0}$, a key parameter in scaling analysis is the ratio $u_{res} = v_{res}/v_e$ between the “response velocity” $v_{res} = L/D$ and the “evolution velocity” $v_e = L_e/D_e$, where L is the maximum linear dimension of the basin, and L_e and D_e are characteristic linear dimensions and durations of organized rainfall features. While ARF depends on L , D and the return period T in a complicated way, some simple asymptotic results hold:

For u_{res} small (say $u_{res} < 0.2$), ARF is close to 1. For example, raingauge records have minimal area coverage (i.e. $L \rightarrow 0$), and hence $u_{res} \ll 1$ and $ARF \rightarrow 1$. This is in agreement with the fact that when the averaging area is zero (i.e. $L = 0$) the Intensity Duration Area Frequency (IDAF) curves reduce to the familiar Intensity Duration Frequency (IDF) curves, and thus

$$ARF = \frac{IDAF}{IDF} = 1.$$

For u_{res} large (say $u_{res} > 5$) ARF becomes a power function of L/D and T with exponents that depend on L , D and T ; see Table 3.1 and Figure 3.4. For moderate T and small L , $ARF \propto (L/D)^{\gamma_1}$, and thus the return period as well as the shape of the rainfall collecting region are not influential. The constant γ_1 is the value of γ for which the co-dimension function $c(\gamma)$ of the multifractal rainfall process equals 1; hence $\gamma_1 < 1$. For moderate L and large T , $ARF \propto (L/D)^{-1} T^{-b}$. These theoretical findings are similar to those of Veneziano and Furcolo (2002a) for the IDF

scaling. Specifically, Veneziano and Furcolo (2002a) found that for moderate T and small D , the IDF value scales like $D^{-\gamma_1}$, whereas for moderate D and very large T , $IDF \propto D^{-1}$.

For $T \rightarrow \infty$, b is a positive constant that depends on the Euclidean dimension of the observation space d ($d = 2$ for rainfall observed along a line segment, $d = 3$ for rainfall observed over a square or disc); see Section 3.1.1. For $T \rightarrow \infty$ and rectangular regions, $d = 3$ and the elongation of the region does not affect the properties of the IDAF curves and the ARFs. By contrast, for intermediate T , b depends significantly on T and on the shape and size of the observation region; see Section 3.1.2. Specifically, b is larger for regularly shaped basins and for larger T . The increase further depends on the shape and size of the region, with faster increase for smaller and regularly shaped basins. This seems to be the first time that the effect of the shape of the rainfall collecting region on the ARF has been studied.

One concludes that, under the assumption of isotropic multifractality of the rainfall field in space and time, the ARF values are influenced significantly by T and by the shape of the rainfall collecting region. Specifically, the ARF scales as $ARF \propto (L/D)^c$, where c increases with T and takes values in the range $[\gamma_1, 1]$; see Table 3.1. This means that the ARF changes faster with L or D for larger values of T . For T either very small or very large, the shape of the region is not influential. For T very small the ARF does not depend on T , whereas for T very large, the ARF decreases as a power function of T with exponent in the range $(-1, 0)$; see Table 3.1. For intermediate values of T the shape of the rainfall collecting region becomes influential. Specifically the ARF decreases faster for regularly shaped basins relative to elongated ones; see Figure 3.14.

These findings may appear contradictory to the ones of N.E.R.C. (1975) that the ARF has a weak dependence on T , but they are in good agreement with what other researchers have found using semi-theoretical rainfall models (Bell, 1976; Asquith *et al.*, 2000; De Michele *et al.*, 2001). However, one should be cautioned that the N.E.R.C.'s empirical findings apply for small return periods (say 1-10 years) where, according to our analysis, the effect of T is negligible.

The effect of advection

For the case when $\mathbf{v}_{ad} \neq \mathbf{0}$, we studied the effects of advection on the IDF and IDAF curves and the ARFs. For highly elongated basins, both the direction and magnitude of advection are influential, whereas for rainfall over a regularly shaped region only the magnitude of advection, v_{ad} , matters. An important parameter for advection is the ratio $u_{ad} = v_{ad}/v_e$ between the

magnitudes of the advection velocity and the evolution velocity. We find that for $u_{res} \ll 1$ and T small the ARF is not affected by the magnitude of the advection velocity and it remains constant with L/D and close to 1, whereas for T large the ARF is a power function of T but the prefactor is a decreasing function of u_{ad} . For $u_{res} \gg 1$ the ARF scales as $ARF \propto (L/D)^c T^{-b}$, as happens for the case when $u_{ad} = 0$, but the prefactor depends on the magnitude of u_{ad} and increases as the magnitude of u_{ad} increases; see Figure 3.25 and Tables 3.2 and 3.3.

The theoretical results of both cases (i.e. $\mathbf{v}_{ad} = \mathbf{0}$ and $\mathbf{v}_{ad} \neq \mathbf{0}$) were validated numerically using simple multifractal models; see Figures 3.29 and 3.32. This seems to be the first time that dependence of the ARF on rainfall advection has been studied.

Response velocity and evolution velocity

We also examined the range of velocities v_{res} , v_e and v_{ad} that are encountered in typical hydrologic applications. In problems of flood estimation, v_{res} may be obtained by setting D equal to the concentration time of the basin, t_c . In this case, v_{res} ranges from about 3 to 7.5 Km/h, and depends mostly on the average slope of the basin and much less on its size. High values of v_{res} correspond to developed basins and high slopes. The rainfall evolution velocity, v_e , ranges from about 5 to 20 Km/h and depends on the type of the precipitation area (e.g. mesoscale vs synoptic scale areas); see Table 3.6.

ARF behavior in typical hydrologic applications

Thus, in typical hydrologic applications, values of u_{res} are in the range from 0.15 to 1.5. Therefore, the dependence of the ARF on T is moderate especially for small values of T (say 1-20 years). We conclude that in most cases the ARF is larger than 0.4 and scales as $ARF \propto (L/D)^c$, where the exponent c is smaller than γ_1 ; see Figure 3.4. The former is in agreement with the empirical findings of Koutsoyiannis (1997), and it is valid even for rainfall fields that vary much in both space and time. For example, Figure 3.30 shows the ARFs obtained using a beta-lognormal cascade in two spatial dimensions plus time with high overall co-dimension coefficient $C_t = 0.52$. For $u_{res} = 1.5$ the ARF is near 0.5.

Advection velocity and readjustment of empirical ARFs

The advection velocity v_{ad} usually takes values between 30 and 50 Km/h at small scales (a few kilometers) and from 20 to 40 Km/h at large scales (say 100 or more kilometers). Thus commonly met values of u_{ad} vary in the range from 1 to almost 10, depending on the type of the organized rainfall structures (e.g. convective cells, cloud clusters, stratiform patterns etc.), and

on local conditions (e.g. pressure oscillations caused by cold and warm fronts). Therefore, in flood estimation and design one should readjust the ARFs obtained from empirical diagrams according to local conditions and the type of the precipitation pattern which is assumed to cause the design flood. This can be done for both elongated and regular shaped basins using the expressions in Tables 3.2 and 3.3 respectively.

Storm direction and pattern and their effects on runoff

When overland flow is studied, also the storm direction and pattern are important factors determining the shape of the runoff hydrograph (Lima and Singh, 2002). Specifically, the peak discharges and hydrograph shapes depend strongly on the storm pattern, the characteristics of the catchment area and the direction and speed of storms. Storms moving upstream are normally characterized by hydrographs with early rise, low peak discharge, not steep rising limb and long base time. Also, the sensitivity of the hydrographs to rainfall patterns decreases as the advection velocity of the storm increases. In particular, rainfall intensity patterns become an important parameter when advection velocity is low and less than about 10 Km/hour.

Advection and observed scaling of rainfall

Advection affects the observed spatial and temporal correlation structure of rainfall (Deidda, 2000). This might explain significant differences between the scaling behaviors observed in storm data and continuous rainfall records: storm data are obtained under almost constant advective conditions, whereas continuous rainfall records include the combined effect of different storms. For example, the inconsistency of scaling found between the empirical observations of Menabde and Sivapalan (2000) for scaling of temporal rainfall, and Perica and Fofoula-Georgiou (1996b) for scaling of spatial rainfall (see Section 4.1.2) is due at least in part to the fact that Menabde and Sivapalan (2000) use continuous rainfall records, whereas Perica and Fofoula-Georgiou (1996b) use data from storms.

Deviations from multifractality- bounded cascades

We discussed observed deviations of rainfall from multifractality in the form of dependence of the multiplicative fluctuations on scale. We also reviewed proposed models that capture such deviations, and investigated numerically how the ARF behaves for a bounded cascade representation of rainfall in space and time. We found that when deviations from multifractality exist the ARF scaling is significantly altered. Specifically, for a bounded cascade model in two spatial dimensions plus time, when D is small and L large, the slope of the iso-ARF lines is less

than 1 and increases as L decreases or D increases. For a given L , the slope of the iso-ARF lines increases as D increases approaching 1 for large values of D ; see Figure 4.7. We also found that the ARF values for a bounded cascade are larger than in the multifractal case; see Figure 3.28 and 4.7. The reason is that in a bounded cascade representation of rainfall the amplitude of the multiplicative fluctuations decreases as the observation scale in space or time decreases, and hence the bounded process is smoother than the multifractal process.

Biases from sparse spatial sampling

Since areal averaged rainfall is usually estimated from raingauge records, the density of the observation network has an important effect on the estimated ARFs. Specifically, the average rain-rate in a basin of area A is estimated as the average rain-rate measured by the raingauges inside A . If the raingauge network is fixed, the average number of raingauges in A , $\tilde{N}(A)$, is proportional to A . However, not to disturb rainfall scaling relations including the ARF, \tilde{N} should not depend on A . Evidently, the bias is larger as A decreases and is maximum when A includes just one raingauge. We investigated numerically the effect of the observation network density on the ARFs. We found that for the limit case of areas that include only one raingauge the estimated ARF is approximately 1. For intermediate areas, the iso-ARF lines are curved indicating no scaling of the ARF; see Figures 4.8, 4.9 and 4.10. The curvature increases as the observation network density decreases. Also, the effect of sparse sampling becomes less significant as L increases; see Figures 4.8, 4.9 and 4.10.

We conclude that empirical ARFs based on raingauge measurements, such as those of N.E.R.C. (1975), include biases from the finite raingauge density. These biases become more pronounced as the network density or the observation area decreases. The bias is in the conservative direction of increasing the ARF values; see Figures 4.8, 4.9 and 4.10.

Reproduction of empirical ARF results

Finally we related various features of empirical Areal Reduction Factors (ARFs) to the multifractal character of rainfall, deviations from multifractality in the form of bounded cascades, and sparse spatial sampling. For this purpose we used the original ARF data of N.E.R.C. (1975) re-fitted with minimum smoothing; see Figure 5.3. Finally, we reproduced the N.E.R.C. (1975) iso-ARF curves using multifractal and bounded cascade models, as well as sparse sampling; see Figures 5.8 and 5.9. We found that for large areas and short durations, where the ARF attains the smallest values (Region 1 in Figure 5.3), the log-log slope of the

empirical iso-lines is 2. This is consistent with multifractal rainfall. Slopes smaller than 2 are observed for smaller areas (Regions 2 and 3 in Figure 5.3). Such smaller slopes are produced by bounded cascades and by sparse spatial sampling. Sparseness of the raingauge network becomes most important at the smallest spatial scales. The increased spacing of the iso-ARF curves for large D (Region 4 in Figure 5.3) may be related to a beta component associated with the characteristic linear sizes and lifetimes of mesoscale precipitation areas. However, limitations of the data in this particular region (see above) do not allow confident interpretations.

Research directions

Although this thesis covered a wide range of queries on rainfall scaling (or non-scaling) in space and time several issues still remain open.

One is the existence and effect of anisotropic scaling of rainfall in space and time. Qualitatively, anisotropic scaling would change the slope of the iso-ARF lines for large L and D . Such a scaling behavior was not observed in N.E.R.C.'s (1975) ARF results. However this absence of anisotropy should be confirmed using ARFs from other areas and rainfall data sets.

Finally, the limited accuracy of the N.E.R.C.'s (1975) ARF results in Region 4, where the ARF attains the largest values, did not allow extensive investigation of rainfall scaling in space and time for large values of D (say D larger than several hours). Such an investigation requires accurate empirical ARF results in this region. Although this might be possible, the fact that the ARF in this region is close to 1 makes its accurate determination less critical for practical applications.

References

- Aron, G. and Egborge, C.E. (1973) *A Practical Feasibility Study of Flood Peak Abatement in Urban Areas*, U.S. Army Corps of Engineers, Sacramento, California.
- Asquith, W.H. & Famiglietti, J.S. (2000) Precipitation areal-reduction factor estimation using an annual-maxima centered approach, , *Journal of Hydrology*, **230**, 55-69.
- Austin, P.M. and House, R.A. (1972) Analysis of the structure of precipitation patterns in New Englandn *J. Appl. Meteor.*, **11**, 926-935.
- Bacchi B. & Ranzi R. (1996) On the derivation of the areal reduction factor of storms, *Atmospheric Research*, **42**, 123-135.
- Bahadur, R.R. and Ranga Rao, R (1960), *Ann. Math. Stat.*, **31**, 1015.
- Bell, F.C. (1976) The areal reduction factors in rainfall frequency estimation, Rep. No. 35, Institute of Hydrology, Wallingford.
- Bendjoudi, H., Hubert, P., Schertzer, D., and Lovejoy, S. (1999) Multifractal explanation of rainfall intensity-duration-frequency curves, paper presented at EGS 24th General Assembly, *Eur. Geophys. Soc.*, The Hague, Netherlands.
- Carsteanu, A. and Foufoula-Georgiou, E. (1996) Assessing Dependence Among Weights in a Multiplicative Cascade Model of Temporal Rainfall, *J. of Geophys. Res.*, **101**(D21), 26 363-26 370.
- Castro, J., Cârsteanu, A., and Flores, C. (2004) Intensity – duration – area – frequency functions for precipitation in a multifractal framework, *Physica A*, (in press).
- Chaudhry, F.H., Filho A.G.A., Calheiros, R.V. (1996) Statistics on tropical convective storms observed by radar. *Atm. Res.*, **42**, 217-227.
- Chow, V. (1959) *Open-Channel Hydraulics*, McGraw-Hill, Inc.
- Coles, S.G., Tawn, J.A. (1996) Modelling Extremes of the Areal Rainfall Process, *J. R. Statist. Soc.*, **B 58**, No. 2, 329-347.
- Cramer, H. (1938) in: *Actualites Scientifiques et Industrielles*, No. 736, Colloque consacre a la theorie des propabilites, Herman.
- Deidda, R. (2000) Rainfall down scaling in a space-time multifractal framework, *Wat. Res. Res.*, **36**(7), 1779-1794.
- Dembo, A. and Zeitouni, O (1993) *Large Deviation Techniques and Applications*, Jones and Barlett.
- Den Hollander, F. (2000) *Large deviations*, American Mathematical Society.
- Farthouat, B. (1962) Analyse des précipitations à l'observatoire de Bordeaux Floirac. Relations entre quantité, durée, intensité, période. *La Météorologie*, Quatrième Série **67**, p. 291-295.

- Federal Aviation Administration (1970) *Circular on airport drainage*, Report A/C 050-5320-5B, Washington, D.C.
- Ferraris, L., Gabellani, S., Parodi, U., Rebori, N., Von Hardenberg, J. and Provenzale, A. (2003) Revisiting Multifractality in Rainfall Fields, *J. of Hydrometeorology*, **4**, 544-551.
- Fraedrich, K. and Larnder, C. (1993) Scaling Regimes of Composite Rainfall Time Series, *Tellus*, **45A**, 289-298.
- Frish, U. (1985) Fully Developed Turbulence and Intermittency, in *Turbulence and Predictability in Geophysical Fluid Dynamics*, edited by M. Ghil, R. Benzi and G. Parisi, p.71-84, Elsevier, New York.
- Frish, U. and Parisi, G. (1985) On the Singularity Structure of Fully Developed Turbulence, in *Turbulence and Predictability in Geophysical Fluid Dynamics*, edited by M. Ghil, R. Benzi and G. Parisi, p.71-84, Elsevier, New York.
- Gupta, V.K. and Waymire, E. (1993) A statistical analysis of mesoscale rainfall as a random cascade, *J. Appl. Meteorol.*, **32**(2), 251-267.
- Harris, D., Menabde, M., Seed, A. and Austin, G. (1998) Breakdown coefficients and scaling properties of rain fields. *Nonlinear Processes Geophys.*, **5**, 93-104.
- Hershfield, D.M. (1962) Extreme rainfall relationships. Proc. Am. Soc. Civ. Eng. , *J. Hydraul. Div.*, **HY6**(11): 73-79.
- Hubert, P., Tessier, Y., Ladoy, P. Lovejoy, S., Schertzer, D., Carbonnel, J.P., Violette, S., Desurogne, I., and Schmitt, F. (1993) Multifractals and extreme rainfall events, *Geoph. Res. Lett.*, **20**, 931-934.
- Izzard, C.F. (1946) *Hydraulics of Runoff from Developed Surfaces*. Proceedings, 26th Annual Meeting of the Highway Research Board, **26**, pp. 129-146.
- Kahane, J.-P., and Peyriere, J. (1976) Sur Certaines Martingales de Benoit Mandelbrot, *Adv. Math.*, **22**, 131-145.
- Kawamura, A., Jinno, K., Berndtsson, R., Furukawa, T. (1996) Parameterization of rain cell properties using an advection-diffusion model and rain gage data. *Atm. Res.*, **42**, 67-73.
- Kirpich, T.P. (1940) Time of concentration of small agricultural watersheds. *Civil Eng.* **10**(6), 362.
- Koutsoyiannis, D. (1997) *Statistical Hydrology* (in Greek), 4th Edition, Department of Water Resources, Hydraulic and Maritime Engineering - National Technical University of Athens, Greece.
- Ladoy, P., Schmitt, F., Schertzer D. and Lovejoy, S. (1993), Variabilité temporelle des observations pluviométriques à Nîmes, *C. R. Acad. des Sci.*, **317**, **II**, 775-782.
- Leclerc, G. & Schaake, J.C. (1972) *Derivation of hydrologic frequency curves*. Report 142, Massachusetts Institute of Technology, Cambridge, MA, 151 pp.

- Lima, J.L.M.P. and Singh, V.P. (2002) The influence of the pattern of moving rainstorms on overland flow. *Adv. in Wat. Res.*, **25**, 817-828.
- Lovejoy, S. and Schertzer D. (1995) Multifractals and rain, *New uncertainty Concepts in Hydrology and Hydrological Modeling*, Ed. A. W. Kundzewicz, 62-103, Cambridge press.
- Martin, D.W. and Schreiner, A.J. (1981) Characteristics of West African and East Atlantic Cloud Clusters: A Survey from GATE. *Monthly Weather Review*, **109**, 1671-1688.
- Mecklenburg, S., Joss, J., Schmid, W. (2000) Improving the nowcasting of precipitation in an Alpine region with an enhanced radar echo tracking algorithm. *J. of Hydrol.*, **239**, 46-68.
- Menabde, M (1998) Bounded lognormal cascades and quasi-multiaffine random fields, *Nonlinear Processes Geophys.*, **5**, 63-68.
- Menabde, M, Harris, D., Seed, A., Austin, G and Stow, D. (1997a) Multiscaling properties of rainfall and bounded random cascades, *Wat. Res. Res.*, **33**(12), 2823-2830.
- Menabde, M, Seed, A. and Pegram, G (1999) A simple scaling model for extreme rainfall, *Wat. Res. Res.*, **35**(1), 335-340.
- Menabde, M, Seed, A., Harris, D. and Austin, G (1997b) Self-similar random fields and rainfall simulation, *J. Geophys. Res.*, **102**(D12), 13, 509-13, 515.
- Menabde, M. and Sivapalan, M. (2000) Modelling of rainfall time series and extremes using bounded random cascades and Levy-stable distributions, *Wat. Res. Res.*, **36**(11), 3293-3300.
- Meneveau, C. and Sreenevasan, K. R. (1987) The Multifractal Spectrum of the Dissipation Field in Turbulent Flow, *Nucl. Phys. B., Proc. Suppl.*, **2**, 49-76.
- Merzin, M.Yu., Srarokoltsev, E.V., Fujiyoshi, Y., Yoshizaki, M. (2003) Contribution of different scales to integral moisture transport based on aircraft observations over the Sea of Japan. *Atm. Res.*, **69**, 109-124.
- Mood, A. M., Graybill, F. A. and Boes, D. C. (1974) *Introduction to Statistical Theory*. 3rd ed., McGraw-Hill, New York.
- Morgali, J.R. and Linsley, R.K. (1965) *Computer Analysis of Overland Flow*. *J. of Hyd. Div., Am. Soc. of Civ. Eng.*, **91**, no. HY3.
- Morin, E., Enzel, Y., Shamir, U., Garti, R. (2001) The characteristic time scale for basin hydrological response using radar data. *J. of Hyd.*, **252**, 85-99.
- Natural Environmental Research Council (N.E.R.C.) (1975), *Flood Studies report*, Vol. 2, Institute of Hydrology, Wallingford, U.K.
- Olsson, J. (1995) Limits and Characteristics of the Multifractal Behavior of a High-Resolution Rainfall Time Series, *Nonlinear processes in Geophysics*, **2**, 23-29.
- Olsson, J., Niemczynowicz, J. and Berndtsson, R. (1993) Fractal Analysis of High-Resolution Rainfall Time Series, *J. of Geophysical Research*, **98**(D12), 23 265-23 274.

- Omolayo, A.S. (1993) On the transposition of areal reduction factors for rainfall frequency estimation, *Journal of Hydrology*, **145**, 191-205.
- Orlanski, I. (1975) A Rational Subdivision of Scales for Atmospheric Processes. American Meteorological Society, **56**(5), 527-530.
- Over, T.M. and Gupta, V.K. (1994) Statistical Analysis of Mesoscale Rainfall: Dependence of a Random Cascade Generator on Large-Scale Forcing, *J. Applied Meteorology*, **33**, 1526-1542.
- Over, T.M. and Gupta, V.K. (1996) A Space-Time Theory of Mesoscale Rainfall Using Random Cascades, *J. of Geophys. Res.*, **101**(D21): 26 319- 26 331.
- Papoulis, A. (1990) *Probability and Statistics*, Prentice Hall.
- Perica, S. and Foufoula-Georgiou, E. (1996a) Linkage of scaling and thermodynamic parameters of rainfall: Results from mid-latitude mesoscale convective systems. *J. of Geoph. Res.*, **101**, 7431-7448.
- Perica, S. and Foufoula-Georgiou, E. (1996b) Model for multiscale disaggregation of spatial rainfall based on coupling meteorological and scaling descriptions. *J. of Geoph. Res.*, **101**(D21), 26 347-26 361.
- Roche, M. (1966) *Hydrologie de Surface*, Gauthier-Villars, Paris, France.
- Rodriguez-Iturbe, I. & Mejia, J.M. (1974) On the transformation of point rainfall to areal rainfall, *Water Resour. Res.*, **10**(4), 729-735.
- Samorodnitsky, G. and Taqqu, M.S. (1994) *Stable Non-Gaussian Random Processes*, Chapman & Hall, New York.
- Schertzer, D. and Lovejoy, S. (1987) Physical modeling and analysis of rain and clouds by anisotropic scaling of multiplicative processes, *J. Geophys. Res.*, **92**, 9693-9714.
- Schmitt, F., Vannitsem, S. and Barbosa A. (1998) Modeling of Rainfall Time Series Using Two-State Renewal Processes and Multifractals, *J. Geophys. Res.*, **103**(D18), 23 181-23 193.
- Seed, A. (1989) *Statistical problems in measuring convective rainfall*. Ph.D. Thesis, Mc Gill University, p. 143.
- Singh, V.P. (1992). *Elementary Hydrology*. Prentice Hall, Engelwood Cliffs, p. 973.
- Sivapalan M., Blöschl G. (1998) Transformation of point rainfall: Intensity-duration-frequency curves, *Journal of Hydrology*, **204**, 150-167.
- Smith, J.A. (1993) "Precipitation", in *Handbook of Hydrology*, edited by Maidment, D.R., 3.1-3.47, McGraw-Hill, New York, U.S.A.
- Soil Conservation Service (1972) *National Engineering Handbook*, Sec. 4, Hydrology. U.S. Dept. of Agriculture, U.S., GPO, Washington, D.C..

- Stedinger, J.R., Vogel, R.M., Foufoula-Georgiou, E. (1993) “ Frequency analysis of extreme events”, in *Handbook of Hydrology*, edited by Maidment, D.R., 18.1-18.66, McGraw-Hill, New York,U.S.A.
- Stroock, D. W. (1994) *Probability Theory: An Analytic view*, Cambridge University Press, U.S.A.
- Takeuchi, K. (1985) An automatic storm tracking method used to analyze traveling characteristics of heavy rain areas. *Natural Disaster Sci.* **7**(1), 13-24
- Takeuchi, K. and Guardado, A. (1990) Automatic Tracking of Radar Observed Rain Areas, IAHS Publ., no. 197, 261-270.
- Taylor, G. I. (1938) The spectrum of turbulence, *Proc. R. Soc. London A*, **164**(919), 476-490.
- Tessier, Y., Lovejoy, S. and Schertzer, D. (1993) Universal multifractals in rain and clouds: theory and observations. *J. Appl. Meteor.*, **32**, 223-250.
- Tessier, Y., Lovejoy, S., Hubert, P., Schertzer, D., Pecknold, S. (1996). Multifractal analysis and modeling of rainfall and river flows and scaling, causal transfer functions. *J. Geophys. Res.* **101**(D21), 26 427-26 440.
- Thiessen, A.H. (1911) Precipitation for large areas. *Mon. Weather Rev.*, **39**: 1082-1084.
- U.S. Bureau of Reclamation (1973), *Design of Small Dams*, 2nd ed., Washington, D.C.
- United States Weather Bureau (1957) Rainfall intensity-frequency regime. Part 1 – The Ohio Valley. U.S. Department of Commerce, U.S. Weather Bureau Tech. Pap. No. 29, Engineering Division, Soil Conservation Service, U.S. Department of Agriculture, Washington, D.C.
- United States Weather Bureau (1958) Rainfall intensity-frequency regime. Part 2 – The Southeastern United States. U.S. Department of Commerce, U.S. Weather Bureau Tech. Pap. No. 29, Engineering Division, Soil Conservation Service, U.S. Department of Agriculture, Washington, D.C.
- Upton, G.J.J. (2002) A correlation-regression method for tracking rainstorms using rain-gauge data. *J. of Hydr.*, **261**, 60-73.
- Veneziano, D. (2002) Large Deviations of Multifractal Measures, *Fractals*, **10**(1), 117-129.
- Veneziano, D. and Furcolo, P. (2002a) Multifractality of rainfall and intensity-duration-frequency curves, *Wat. Res. Res.*, **38**(12), 1306-1317.
- Veneziano, D. and Furcolo, P. (2002b) Scaling of multifractal measures under affine transformations, *Fractals*, **10**(2), 147-156.
- Veneziano, D. and Niemann, J. D. (2000) Self-similarity and multifractality of fluvial erosion topography 2. Scaling properties, *Wat. Res. Res.*, **36**(7), 1937-1951.
- Veneziano, D., Bras, R.L. and Niemann, J.D. (1996) Nonlinearity and Self-similarity of Rainfall in Time and a Stochastic Model, *J. of Geoph. Res.*, **101**(D21), 26 371-26 392.

Veneziano, D., Furcolo, P. and Iacobellis, V. (2003) Imperfect Scaling of Time and Space-Time Rainfall, *Hydrofractals '03, An international conference on fractals in hydrosciences*, Monte Verita, Ascona, Switzerland, August 2003, ETH Zurich, MIT, Université Pierre et Marie.

Zawadzki, I.I. (1973) Statistical properties of precipitation patterns. *J. Appl. Met.*, **12**, 459-472.

Appendix A

Linkage between Haar wavelets and micro-canonical cascades

Here we show how the standardized fluctuations of Haar wavelets are related to the generator of a 1D micro-canonical cascade for rainfall intensities; see also Section 4.1.2.

Specifically, we obtain the standard deviation $\sigma_q(m)$, with the scale m , of the generator q_m of a 1D micro-canonical cascade, as a function of the standard deviation σ_m of the standardized fluctuations ξ_m of Haar wavelets; for more details see Section 4.1.2.

For the rest of the analysis we focus on direction $i = 1$; see Figure A.1. However, when directional differences are insignificant, as in our case (see Section 4.1.2), the analysis is valid for any direction i .

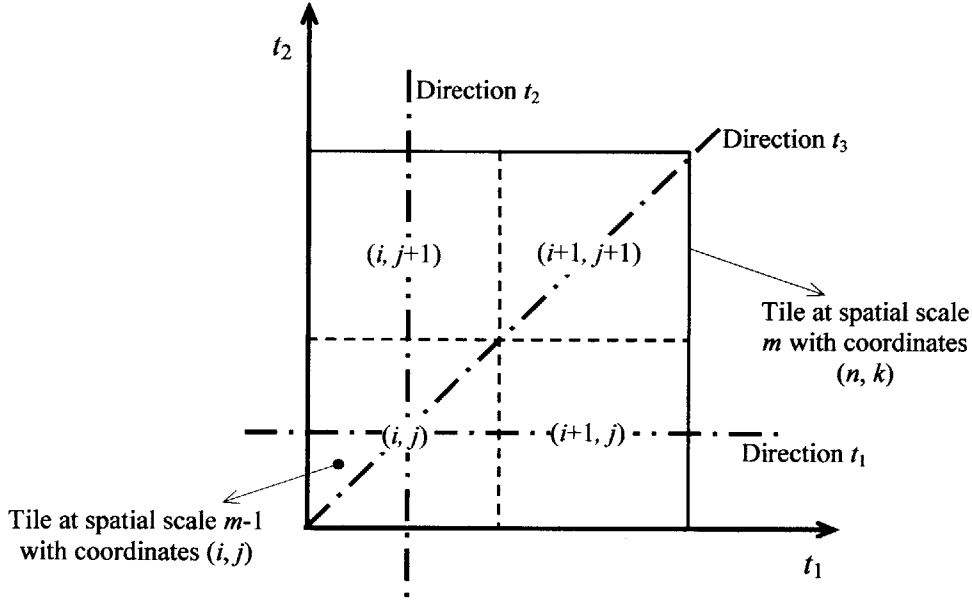


Figure A.1: Cascade tiles at relative spatial scales $m-1$ and m . The coordinates (i, j) , (n, k) and the spatial scales $m-1$ and m are the same as in Section 4.1.2.

Denote by $I_{m-1}(i, j)$ the rainfall intensity inside a cascade tile at scale $m-1$ centered at point (i, j) ; see Figure A.1. q_m is the partition coefficient at scale m in direction $i = 1$ given by,

$$q_m =_d \frac{I_{m-1}(i, j)}{I_{m-1}(i, j) + I_{m-1}(i+1, j)} \quad (\text{A.1})$$

Using equations (4.9)-(4.13) equation (A.1) becomes,

$$q_m =_d 1 + \frac{\zeta_{m,2} + \zeta_{m,3}}{1 + \zeta_{m,2}} \quad (\text{A.2})$$

One can use Taylor series expansion around zero and write:

$$q_m =_d 1 + \zeta_{m,2} + \zeta_{m,3} + O(2) \quad (\text{A.3})$$

where $O(2)$ denotes terms with order larger than 1.

Neglecting non linear terms and assuming that directional differences in the distribution of ζ are insignificant, one has:

$$\sigma_q(m) = \sqrt{2} \sigma_m, \quad m \geq 1 \quad (\text{A.4})$$

If σ_m is given by equation (4.14), then the standard deviation of the generator q_m is

$$\sigma_q(m) = 2^{(m-1)H+0.5} \sigma_1, \quad m \geq 1 \quad (\text{A.5})$$